Investigation of Impingement Jet Array Heat Transfer With High Temperature Ratio and High Crossflow

Wesley Ramm

St Edmund Hall

University of Oxford

A thesis submitted for the degree of

Master of Science (Research)

Hilary Term 2025

Acknowledgements

The opportunity to undertake research at the University of Oxford, and to be affiliated with St Edmund Hall, has been both intellectually and personally rewarding. The College provided a consistent source of community and support throughout this period, and I am grateful for that connection.

I would like to thank Dr Budimir Rosic and Dr David Gillespie, who served as my formal supervisors during this degree. I am also grateful to Mitsubishi Heavy Industries for their financial support and for the opportunity to engage with their research programme.

This project would not have been possible without the support of many others. A few individuals deserve particular recognition:

- **Dr Mark Baker**, whose postdoctoral guidance, critical insight, and intellectual energy were central to the development and completion of this work.
- **Mr Greg King**, for his technical expertise and precision in the construction of the experimental rig and instrumentation.
- **Hal Surtel, William Godfrey, Craig Parsons, and Roger Robinson**, for their dependable and responsive support throughout the project. Their commitment to student work is deeply appreciated.

I would also like to acknowledge Oguzhan, Jamie, Simla, Faisal, Mohammed, and Nikolas. The experience of working alongside you, particularly through the disruptions of COVID, was a privilege. I look forward to what you each go on to do next.

Finally, to my family and friends, especially Rob Anderson, whose encouragement over 35 years has never faltered: thank you for your unwavering support.

Lucinda also deserves special mention: her patience and encouragement have been indispensable throughout this journey.

Abstract

This thesis reports the development and commissioning of an experimental facility for investigating impingement cooling strategies relevant to gas turbine applications. The rig was modular, with precise thermal boundary control and a tailored instrumentation system for empirical determination of local and overall heat transfer coefficients. It extended the capability of published facilities by achieving higher temperature ratios than are commonly reported in canonical studies.

The facility was first validated by reproducing benchmark correlations from canonical impingement literature. Comparisons with established data confirmed stable, representative behaviour across a range of Reynolds numbers and thermal conditions.

Following validation, a corrugated jet plate configuration was assessed as a means of mitigating the adverse crossflow that typically degrades impingement performance. Experiments showed that this geometry exhibited less downstream degradation of Nusselt number compared to flat plate designs.

In parallel, a numerical study explored a novel supplementary approach based on in-plane thermal conduction. A simplified two-dimensional model of embedded high-conductivity inserts indicated potential for lowering peak surface temperatures and redistributing heat laterally where direct impingement is impractical.

These findings suggest that targeted geometric modifications and hybrid conduction–convection strategies can enhance internal blade cooling performance and reduce reliance on film cooling in future gas turbine designs.

Contents

Appendices

List of Figures

List of Tables

Abbreviations

	1D, 2D, 3D: One-, two-, or three-dimensional (spatial)
AM	Additive Manufacturing
CAGR	Combined Annual Growth Rate
CCGT	Combined Cycle Gas Turbine
CAD	Computer-Aided Design
CFD	Computational Fluid Dynamics
GUI	Graphical User Interface
h	Heat Transfer Coefficient
HTC	Heat Transfer Coefficient
IEA	International Energy Agency
IR	Infrared
MHI	Mitsubishi Heavy Industries
NI	National Instruments
NGV	Nozzle Guide Vane(s)
PIV	Particle Image Velocimetry
PID	Proportional–Integral–Derivative
RANS	Reynolds-Averaged Navier–Stokes
SCADA	Supervisory Control and Data Acquisition
SSR	Solid-State Relay
TBC	Thermal Barrier Coating
TET	Turbine Entry Temperature
TR	Temperature Ratio (T_w/T_j)
YSZ	Yttria-Stabilised Zirconia

Nomenclature

A_j	Single Jet Hole Cross Sectional Area [m^2]
c_d	Jet Plate Discharge Coefficient
c_p	Specific heat capacity [J/kg·K]
d	Jet Diameter [m]
$\dot{Q}$	Heat transfer rate [W]
γ	Ratio of Specific Heats [−]
h	Convective heat transfer coefficient or spacing from jet to surface [W/m^2·K] or [m]
k	Thermal Conductivity [W/m·K]
Nu	Nusselt Number [−]
P_0	Jet Plenum Pressure [Pa]
P	Ambient (Reference) Pressure [Pa]
Pr	Prandtl Number [−]
R	Ideal Gas Constant [J/kg·K]
Re	Reynolds Number [−]
T	Temperature [K]
T_∞	Freestream or mainstream hot gas temperature [K]
T_j	Jet Temperature [K]
T_w	Wall Temperature [K]
T_{ref}	Convective Heat Transfer Reference Temperature [K]
T_{surf}	Convective Heat Transfer Surface Temperature [K]
$\dot{m}_c$	Cross Flow Mass Flow Rate [kg/s]
$\dot{m}_j$	Total Jet Flow Mass Flow Rate [kg/s]
$\dot{m}_j{}^*$	Individual Jet Mass Flow Rate [kg/s]
ρ	Fluid Density [kg/m^3]
x/d	Geometric parameter for streamwise-pitch [−]

y/d	Geometric parameter for spanwise-pitch [−]
z/d	Geometric parameter for channel height [−]
H	Non-dimensional height parameter [$= h/d$]
N_x	Number of jets in streamwise direction [−]
N_y	Number of jets in spanwise direction [−]
η	Film Cooling Effectiveness [−]
$\overline{T}$	Mean Surface Temperature [K]
σ_T	Standard Deviation of Surface Temperature [K]
$\phi_{T>\overline{T}}$	Fraction of surface area above mean temperature [−]
TR	Temperature Ratio, T_w/T_j [−]

1

Introduction

1.1 Background and Industrial Relevance

The continuing push for higher thermal efficiencies and power outputs in modern gas turbine engines has driven turbine inlet temperatures to extreme levels. These operating temperatures regularly exceed the melting point of standard blade materials, mandating sophisticated cooling strategies to ensure component durability and reliable performance. Among these strategies, impingement jet cooling has seen widespread adoption due to its ability to deliver high local heat transfer rates. In many gas turbine designs, air bled from the high-pressure stages of the compressor is directed through internal cooling passages, where it impinges on critical surfaces prior to exiting as film cooling flow on the external blade surface.

Despite its efficacy, extracting compressor bleed air entails a significant performance penalty. Reducing this penalty by minimizing the required cooling airflow can enhance the overall performance and efficiency of the turbine. Furthermore, while film cooling helps maintain blade temperatures within safe operating limits, it also imposes aerodynamic and thermodynamic penalties on the main turbine flow. It is not explicitly known whether gas turbine manufacturers are currently exploring the removal of film cooling altogether, but the potential for significant performance gains makes this a compelling area of research.

1.2 Impingement Cooling and Crossflow Challenges

When multiple impingement jets are installed in series within a confined blade passage, the spent coolant from upstream jets flows downstream as crossflow, interfering with subsequent jets. This interference can reduce local heat transfer

coefficients for downstream impingement zones, thereby compromising the blade's overall cooling effectiveness. High-pressure turbine blades, which must withstand both extremely high gas temperatures and large pressure gradients, are particularly susceptible to high heat loading. Even partial losses in cooling effectiveness can lead to significant reductions in blade life.

1.3 Additive Manufacturing and its Role in Cooling Design

Additive Manufacturing (AM) has emerged as a transformative technology in the gas turbine industry, and as of the time of the publication of this thesis, production AM components for industrial gas turbines are in the market. Additive manufacturing techniques enable the fabrication of complex internal geometries that are otherwise infeasible or prohibitively expensive using conventional manufacturing methods. Two key aspects of AM are particularly relevant to this research:

1.3.1 Alternative Passage Channel Geometries

Advanced layer-by-layer fabrication allows the creation of interior surfaces like corrugations or "castellations". These features can expand the cross-sectional area available for spent coolant flow, potentially mitigating the build up of cross-flow. By providing additional flow volume, a castellated design may improve downstream cooling effectiveness while maintaining high local heat transfer near the impingement sites.

1.3.2 Anisotropic Material Properties

In addition to allowing new freedom in component geometries, AM offers the potential to tailor material properties within a single component. This capability opens the door to a more holistic approach to blade cooling, which is being proposed in this thesis: specifically, the selective placement of high-thermal-conductivity regions in the blade wall. By transporting heat from hotter regions of the blade to

areas with more effective or less obstructed coolant access, this approach could reduce the need for multiple impingement jets in series. In such a scenario, downstream jets may become less critical or even unnecessary, since heat would be conducted to the region of most efficient impingement.

Though realization of fully anisotropic spatially graded thermal properties in production components may lie in the future, current research indicates that such material property tailoring is indeed feasible at the laboratory scale. Furthermore, by the time of the publication of this thesis, 3D printing with multiple metallic materials has already been demonstrated. [1]

In this project, a combination of numerical modelling and fundamental analysis will be used to demonstrate the potential benefits of localized high-conductivity regions. This strategy could eventually allow the avoidance of classical crossflow challenges by consolidating impingement cooling in a single, optimal region and leveraging thermal conduction to distribute heat away from localized hotspots.

1.4 Research Objectives

This research is conducted with industrial sponsorship from Mitsubishi Heavy Industries (MHI), which aims to investigate how a castellated or corrugated jet plate can mitigate channel crossflow and enhance overall cooling effectiveness. To support this objective, an experimental facility has been constructed to quantify impingement jet Nusselt numbers for a range of jet Reynolds numbers on a fixed array of jets impinging on a flat target plate. The test rig has been designed within severe budget constraints to provide well-characterized local heat transfer measurements, with a particular focus on modularity, to allow study of alternative geometry jet and target plate configurations.

Independent of the goals of our research sponsor, this Master's thesis explores a novel approach to blade cooling: leveraging in-plane conduction to redistribute heat within the blade wall, transferring thermal energy from hotspots to more effectively cooled regions. While this concept is beyond the scope of the current experimental setup, it will be evaluated through numerical modelling and theoretical analysis. If

[1] See: "Multi material Metal Printing: The Future of Additive Manufacturing," Fraunhofer IGCV. [1]

proven viable, this approach could reduce reliance on multiple impingement jets, lowering bleed air requirements and simplifying cooling system design.

1.5 Chapter Overview and Thesis Structure

This introductory chapter outlines the motivation for investigating impingement jet cooling under crossflow conditions, alongside a parallel effort to develop a new conductive thermal management paradigm enabled by recent advances in additive manufacturing. Subsequent chapters are as follows:

- **Chapter 2**: Reviews the fundamental physics and thermodynamics of jet impingement relevant to this study.
- **Chapter 3**: Surveys the literature on impingement jet behaviour, crossflow development, mitigation strategies, and AM-enabled cooling technologies, including functionally graded materials.
- **Chapter 4**: Describes the experimental facility, instrumentation, and methods used to evaluate flat-plate heat transfer under impingement cooling, including tests with corrugated jet geometries.
- **Chapter 5**: Presents experimental results, highlighting flow field characteristics, local Nusselt number distributions, and the influence of temperature ratio and jet Reynolds number.
- **Chapter 6**: Examines numerical and theoretical modelling of enhanced in-plane conduction using high-conductivity inserts, assessing their role in mitigating crossflow limitations.
- **Chapter 7**: Concludes with the key findings and identifies future research directions, including the use of optimisation techniques to refine geometry concepts for the conduction cooling approach.

By focusing on near-term, geometry-based solutions and longer-term material innovations, this work aims to provide an integrated perspective on impingement jet cooling for advanced turbine blade applications. The ultimate goal is to support

strategies that reduce bleed air extraction, simplify blade manufacturing, and maintain robust cooling performance under the demanding conditions of modern gas turbine operation.

2

Fundamentals of Impingement Jet Cooling in Gas Turbines

In addition to examining the physics underpinning impingement jets and their analysis, this section develops a more rigorous theoretical foundation by revisiting key principles such as power-law correlations and fundamental heat transfer theory. Inclusion of this analysis supports clearer interpretation of results, provides context for modelling choices, and enables comparison across a broader range of cooling configurations.

2.1 Introduction: Advanced Cooling in Gas Turbines

Modern gas turbines operate at increasingly high pressures and temperatures to improve thermal efficiency and power density. These conditions often exceed the material limits of turbine blades and vanes, requiring advanced cooling strategies to prevent degradation from thermal stress, oxidation, and creep.

Impingement jet cooling is one of the most effective methods for localized heat removal, particularly in high-flux regions such as blade leading edges. To design and optimize such systems, it is critical to quantify the convective heat transfer they produce. Even a single jet creates highly non-uniform heat transfer due to distinct regions of stagnation, wall jet development, and boundary layer growth. In jet arrays, these effects are compounded by crossflow and jet-to-jet interference, which alter both flow structure and surface heat transfer. Accurately characterizing these interactions is essential for predicting temperature distributions and ensuring reliable thermal performance under extreme operating conditions.

2.2 The Problem of Convection

The primary concern in the study of convective heat transfer is to find some way to develop a value for the average or local heat transfer coefficient h for a particular configuration of fluid flow and geometry. This is not trivial and involves either the solution to the relevant boundary layer equations directly, or determination of HTC through experimental methods. Of course, solving the boundary layer equations without massive simplification is very difficult. Experiments can be used to carefully measure the the amount of heat transfer in a particular case. This is the basis of the experimental work described by this thesis.

The experimental rig that has been developed allows the direct measurement of heat transfer coefficient for a heated target surface, onto which an array of impingement jets is directed. This correlates to classical experiments in fluid mechanics for simplified geometries like external flow over a flat plate. Indeed, one of the fundamental concepts in every undergraduate text in fluid mechanics is illustrated in Figure 2.1 below.

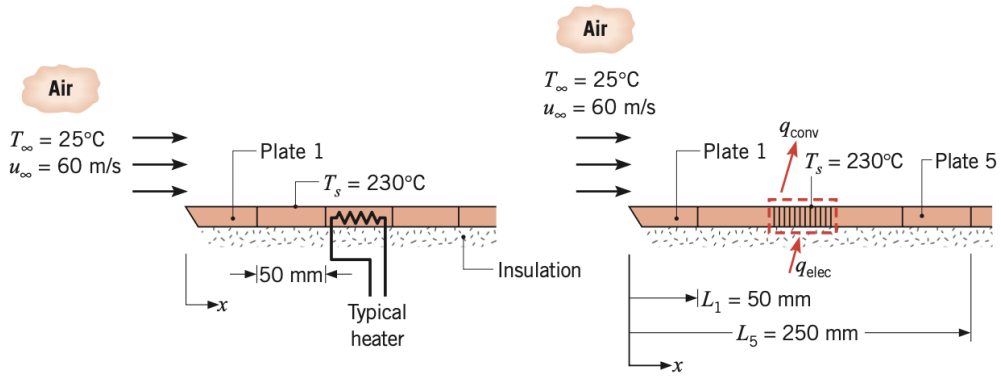

Figure 2.1: Experiment measuring heat transfer coefficient in forced convection.

2.2.1 The Empirical Method

In this experiment, a flat plate is heated electrically, and mounted in an insulative substrate so that heat can only travel in the 'up' direction, or into the moving fluid. If the plate is maintained at a temperature greater than the free stream fluid temperature, then there must be heat transfer from the plate to the fluid. It is a

relatively simple matter to measure the temperature of the plate and the electrical power, which correlates directly to the test section heat transfer coefficient (HTC).

A series of experiments could be conducted across a wide range of fluid velocities, plate lengths, and working fluids with differing Prandtl numbers. This would yield a corresponding set of Nusselt numbers associated with various Reynolds and Prandtl number combinations, which could then be plotted to identify trends.

This empirical methodology provides a practical means of determining the heat transfer coefficient for a given flow geometry. If the experiment is carefully designed, Newton's law of cooling can be applied to extract the heat transfer coefficient, since the rate of heat transfer from the heated plate to the fluid is given by:

$$I \cdot E = q = \overline{h_l} A_s (T_s - T_\infty) \tag{2.1}$$

Where I, E are known because heater power can be measured directly. In this well insulated experimental facility, it is appropriate to assume that all of the heater power q flows to the working section. This assumption makes it possible to solve directly for heat transfer coefficient.

A_s is known because the experiment is designed, and T_s and T_∞ can be measured at the mainstream fluid inlet and at the plate surface.

This trivial experimental setup forms the basis of the theory of the experimental facility developed for this project.

If a number of such experiments are carried out for for varying fluid velocity, Pr, plate length, electrical power etc., and plotted on a log–log scale, a distinct family of curves is obtained, as shown in Figure 2.2(a). By non-dimensionalising the data, as illustrated in Figure 2.2(b), these results can be collapsed onto a single curve, enabling direct comparison across a range of operating conditions. This approach, grounded in the Buckingham Pi theorem, forms the foundation of dimensional analysis in fluid mechanics and heat transfer. It provides a powerful means of generalising experimental results and facilitates direct comparison with other studies, making it an indispensable tool for engineers.

Examination of the resultant non-dimensionalised curve suggests that the local Nusselt Number has a functional relationship with Re of the following form:

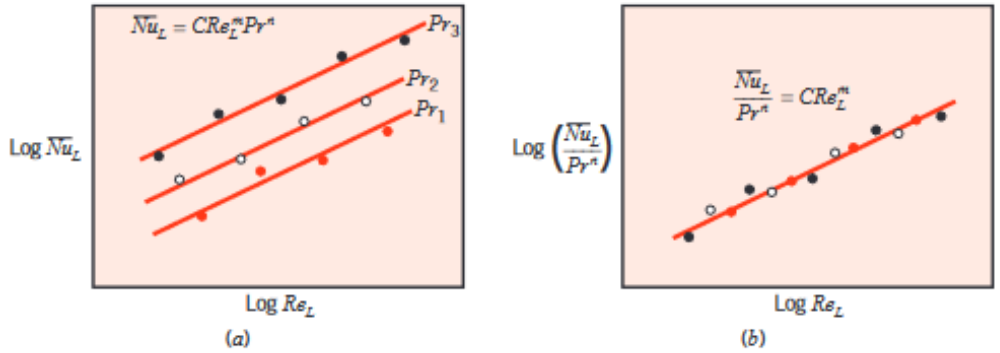

Figure 2.2: Nusselt number correlation for empirical experiment.

$$\overline{Nu_L} = C\, Re_L^m\, Pr^n \tag{2.2}$$

2.2.2 Analytical Methods

This section presents an analytical derivation of the heat transfer correlation using boundary layer theory and the Blasius similarity solution, providing theoretical grounding for the empirical relationship previously introduced.

Under the assumption of laminar flow over a flat plate, the velocity boundary layer thickness scales as:

$$\delta(x) \propto \left(\frac{\nu x}{U_\infty}\right)^{1/2} \tag{2.3}$$

leading to a velocity gradient at the wall:

$$\left.\frac{\partial u}{\partial y}\right|_{y=0} \propto \frac{U_\infty}{\delta(x)} \tag{2.4}$$

2.2.3 Thermal Boundary Layer and Wall Heat Flux

The similarity solution for velocity, expressed in Equation 2.4, reflects the simplified boundary layer equations for laminar flow over a flat plate. A parallel form can

be applied to the thermal boundary layer, which admits a similar treatment under the assumption of constant property laminar flow.

For $\mathrm{Pr} > 1$, thermal diffusion is less effective than momentum diffusion, resulting in a thinner thermal boundary layer. This leads to the classical scaling:

$$\delta_T \propto \delta \cdot \mathrm{Pr}^{-1/3} \tag{2.5}$$

Hence, the temperature gradient at the wall becomes:

$$\left.\frac{\partial T}{\partial y}\right|_{y=0} \propto \frac{\Delta T}{\delta_T} \propto \frac{\Delta T \cdot \mathrm{Pr}^{1/3}}{\delta} \tag{2.6}$$

Substituting into Fourier's law:

$$q'' = -k \left.\frac{\partial T}{\partial y}\right|_{y=0} \propto \frac{k \cdot \Delta T \cdot \mathrm{Pr}^{1/3}}{\delta} \tag{2.7}$$

From this, the heat transfer coefficient becomes:

$$h \propto \frac{q''}{\Delta T} = \frac{k \cdot \mathrm{Pr}^{1/3}}{\delta} \tag{2.8}$$

Finally, the local Nusselt number is expressed as:

$$\mathrm{Nu}_x = \frac{hx}{k} \propto \frac{x}{\delta} \cdot \mathrm{Pr}^{1/3} \propto \mathrm{Re}_x^{1/2} \cdot \mathrm{Pr}^{1/3} \tag{2.9}$$

This is the classical result derived from the Blasius similarity solution, providing a theoretical foundation for the empirically observed power-law relationship between Nusselt number, Reynolds number, and Prandtl number in laminar boundary layers. This result is valid for steady, two-dimensional, incompressible laminar flow over an isothermal flat plate, and assumes constant fluid properties.

2.2.4 Justification for Use of the Classical Correlation Form in Empirical Studies

In general, the empirical form $\mathrm{Nu} = C \cdot \mathrm{Re}^m \cdot \mathrm{Pr}^n$ is valid across a wide range of external flow situations, with constants C, m, n determined by geometry and flow regime. Despite the complexity of real systems such as impingement jets, experimental studies often adopt the same functional form for convective heat transfer correlations as those derived from idealised external flow:

$$\mathrm{Nu} = C \cdot \mathrm{Re}^m \cdot \mathrm{Pr}^n \tag{2.10}$$

This consistent presentation is justified for the following reasons:

Dimensional Consistency and Generality The form emerges naturally from dimensional analysis (e.g. via the Buckingham Pi theorem), where Nu, Re, and Pr are the dominant dimensionless groups in forced convection problems. Using this structure ensures dimensional consistency and generality across fluid types, flow conditions, and geometries.

Consistency with Classical Boundary Layer Theory Even though systems like impingement jets involve additional phenomena (e.g., stagnation flow, jet interference), the fundamental mechanisms—momentum diffusion and thermal diffusion—are still governed by the same transport equations. The classical Blasius solution, for example, provides a theoretical benchmark where:

$$\mathrm{Nu}_x \propto \mathrm{Re}_x^{1/2} \cdot \mathrm{Pr}^{1/3} \tag{2.11}$$

Later experiments extend this scaling to more complex geometries while preserving the same general form.

Empirical Utility and Curve Fitting Experimental data often show approximately linear trends on log-log plots of Nu vs. Re, validating the use of power-law relationships. Presenting correlations in this format simplifies regression analysis, supports straightforward comparison with previous studies, and enhances clarity.

Relevance to Engineering Practice The standard form aligns with the conventions used in engineering design, heat exchanger sizing, and CFD boundary condition modelling. Maintaining consistency facilitates implementation in design tools, empirical databases, and semi-analytical cooling models.

In summary, while the flow field and heat transfer in impingement cooling are more complex than canonical flat plate flows, the continued use of the classical power-law correlation remains valid, useful, and theoretically grounded.

2.3 Physics of Impingement Jet Cooling

2.3.1 Jet Structure and Heat Transfer Mechanisms

Impingement cooling involves directing high-velocity jets of air (or another coolant) onto a target surface. When the jet exits a nozzle and travels toward the surface, it forms a complex flow field with distinct regions that strongly influence the resulting heat transfer. The structure of a typical impinging jet can be divided into three primary zones:

- **Free Jet Region:** This region begins at the nozzle exit and extends to the vicinity of the target surface. Initially, the jet maintains a nearly uniform core velocity while entraining surrounding fluid. As it travels downstream, the jet begins to spread due to viscous diffusion and turbulent mixing.
- **Impingement Region:** As the jet approaches and strikes the surface, the flow decelerates rapidly, forming a stagnation zone. This region is characterized by high normal momentum and steep velocity and temperature gradients, resulting in a peak in local convective heat transfer. The stagnation point represents the location of maximum heat transfer under most conditions.
- **Wall Jet Region:** After impinging, the flow turns radially outward along the surface, forming a wall jet. In this region, the flow gradually develops a boundary layer, and both velocity and heat transfer coefficients decay with increasing distance from the stagnation point. The thickness and strength of the wall jet are influenced by jet Reynolds number, spacing, and surface conditions.

These regions are illustrated in Figure 2.3.

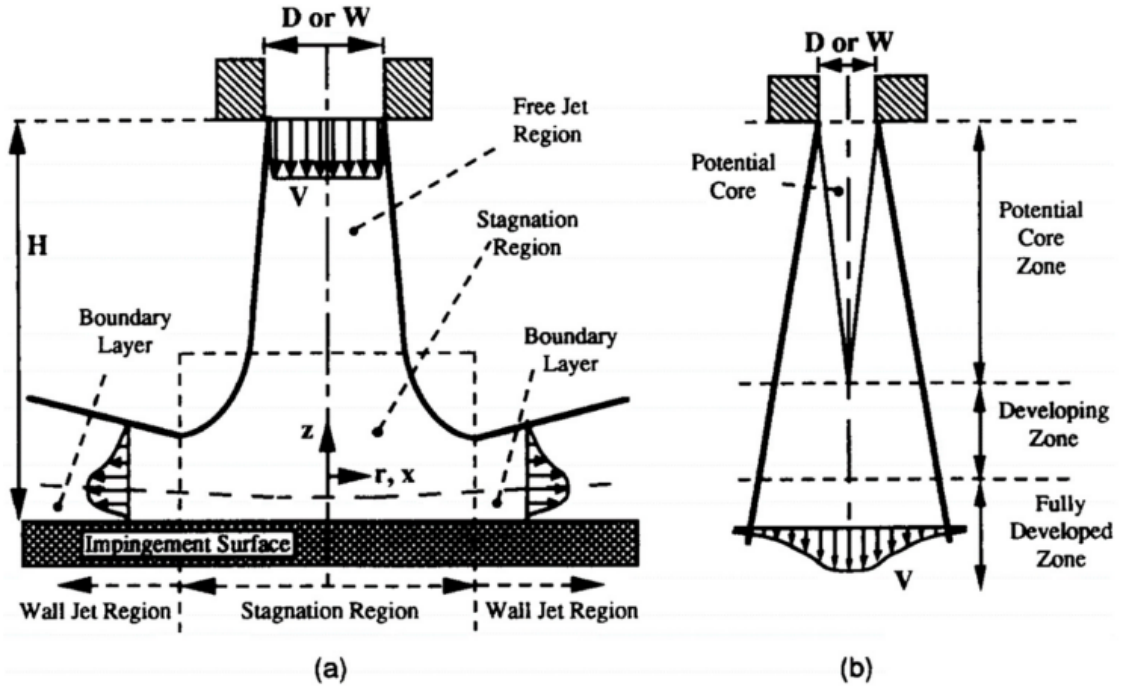

Figure 2.3: Structure of an impinging jet.

Understanding this flow structure is critical because each region contributes differently to surface heat transfer. The stagnation region delivers high local cooling effectiveness, but it is spatially limited. The wall jet region covers a larger area but at lower local heat transfer rates. When jets are arranged in arrays, interactions between adjacent jets, such as crossflow buildup and flow confinement, can disrupt this structure and reduce cooling uniformity. Therefore, the performance of an impingement cooling system depends not only on the characteristics of individual jets but also on how the jets interact with each other and with the surrounding geometry.

2.4 Quantifying Cooling Effectiveness

To characterize heat transfer in impingement systems, the local heat transfer coefficient h is often expressed in terms of the Nusselt number, Nu, which provides a dimensionless measure of convective performance. Distinguishing between local and area-averaged Nusselt numbers is important, particularly in jet arrays where cooling is spatially non-uniform.

$$h = \frac{q''}{T_s - T_\infty}, \quad \mathrm{Nu} = \frac{hD}{k} \tag{2.12}$$

An additional dimensionless parameter, the Stanton number St, relates heat transfer to flow momentum and is defined as:

$$St = \frac{h}{\rho c_p U} = \frac{\mathrm{Nu}}{\mathrm{Re} \cdot \mathrm{Pr}} \tag{2.13}$$

In configurations where the coolant forms a protective film along the surface, such as in combined impingement and film cooling strategies. the local cooling performance is often quantified using the film cooling effectiveness:

$$\eta = \frac{T_\infty - T_w}{T_\infty - T_c} \tag{2.14}$$

where T_∞ is the mainstream freestream gas temperature, T_c is the coolant supply temperature, and T_w is the measured wall (metal) temperature. This formulation corresponds to the overall or metal effectiveness, which accounts for both external convective shielding by the coolant and internal conduction within the wall. In some studies, the adiabatic effectiveness is used instead, where T_w is replaced by the adiabatic wall temperature T_{ad}, representing a surface with no internal cooling or conduction.

While T_∞ is often used as the reference temperature in effectiveness definitions, it represents the local static temperature of the hot gas stream, not the thermal state experienced by a wall exposed to high-speed flow. In reality, viscous dissipation within the boundary layer converts a portion of the kinetic energy in the flow into internal energy, causing the near-wall gas temperature to rise above T_∞. This dissipation arises due to velocity gradients established by the no-slip condition at the wall, which set up shear stress and energy conversion within the fluid.

The stagnation temperature T_0 represents the theoretical maximum temperature obtained through isentropic deceleration of the flow to zero velocity, with no heat loss and no entropy generation. However, this is an idealisation that does not occur in real flows. This motivates the use of the recovery temperature, T_{rec}, which accounts for losses and more accurately reflects the actual temperature a surface would attain under adiabatic conditions. It is defined as:

$$T_{\text{rec}} = T_\infty + r \cdot \frac{u_\infty^2}{2c_p}$$

where u_∞ is the freestream velocity, c_p is the specific heat at constant pressure, and r is the recovery factor, which varies for different flow regimes but can never be greater than 1.0. As such, T_{rec} always lies between T_∞ and T_0, and provides a more physically meaningful reference than T_∞ for evaluating thermal protection in compressible or high-speed flows.

It is important to recognise that the use of adiabatic wall temperature as a reference carries implicit physical assumptions. Specifically, the term "adiabatic" denotes a surface with no heat transfer into the wall, which clearly is not the case in actual engine components where internal cooling and conduction are present. Therefore, the choice of reference temperature, whether static freestream temperature, recovery temperature, or adiabatic wall temperature, must be made judiciously, depending on the physical quantity of interest and the region of the system under investigation, or to align a study with canonical reference work.

2.5 Efficiency Implications of Film Cooling

While film cooling is widely used to protect turbine hot section components from extreme gas temperatures, it introduces secondary effects that can impact overall thermodynamic efficiency. By injecting low-enthalpy coolant into the high-temperature mainstream, film cooling alters the flow's energy content and composition. This mixing is inherently irreversible and results in an increase in entropy, which reduces the potential for useful work in downstream turbine stages.

Although a detailed exergy analysis is beyond the scope of this work, the principle is straightforward: mixing two streams with different temperatures and pressures increases total system entropy, and this entropy generation corresponds to a loss in recoverable energy. This trade-off is particularly important in high-efficiency engine cycles, where even small degradations in thermal efficiency can have meaningful performance impacts.

These considerations help motivate the exploration improving the effectiveness of impingement jet cooling such that film cooling would no longer be necessary. This is explored in later sections and chapters of this thesis.

2.6 Thermodynamic Effects of Wall Heating and the Role of Temperature Ratio

The most intuitive source of crossflow development in impingement-cooled channels is the cumulative mass addition from the jet array. In configurations with a single downstream exit, which is common in gas turbine internal cooling configurations, each successive jet contributes to the streamwise flow, gradually building up channel crossflow. However, an additional and often overlooked mechanism also contributes to this lateral flow: the volumetric expansion of the coolant as it absorbs thermal energy from the hot wall. This thermally driven expansion increases the local velocity even in the absence of added mass, and, as will be shown, plays a critical role in the evolution of the crossflow. Together with temperature-dependent variations in material properties such as viscosity and thermal conductivity, this mechanism underlies the observed influence of temperature ratio on impingement cooling performance.

Under ideal gas assumptions and constant pressure, the density of the fluid varies inversely with temperature:

$$\rho = \frac{p}{RT} \tag{2.15}$$

When a jet at initial temperature T_0 impinges upon a wall at elevated temperature T_1, it absorbs thermal energy and its temperature rises accordingly. This heating process reduces the density from

$$\rho_0 = \frac{p}{RT_0} \tag{2.16}$$

to

$$\rho_1 = \frac{p}{RT_1} \tag{2.17}$$

The fractional change in density, corresponding to the relative volumetric expansion of the fluid, is given by:

$$\frac{\Delta\rho}{\rho_0} = \frac{\rho_0 - \rho_1}{\rho_0} = 1 - \frac{T_0}{T_1} \tag{2.18}$$

This expansion drives an increase in velocity in accordance with the continuity equation for steady flow:

$$\dot{m} = \rho A V = \text{constant} \tag{2.19}$$

For a fixed cross-sectional area A, a reduction in density necessitates an increase in velocity V. As a result, the jet's interaction with the wall induces local acceleration of the coolant, contributing to the growth of crossflow. This crossflow is therefore governed both by jet momentum addition and by thermally induced expansion resulting from wall heating.

To illustrate the sensitivity of volumetric expansion to the initial jet temperature, consider two scenarios in which the jet is heated by the same temperature increment of $\Delta T = 300$ K:

- Heating air from $T_0 = 300$ K to $T_1 = 600$ K:

$$\frac{\Delta\rho}{\rho_0} = 1 - \frac{300}{600} = 0.50 \tag{2.20}$$

- Heating air from $T_0 = 500$ K to $T_1 = 800$ K:

$$\frac{\Delta\rho}{\rho_0} = 1 - \frac{500}{800} = 0.375 \tag{2.21}$$

Although the temperature rise is identical in both cases, the volumetric expansion is greater in the first scenario due to the lower starting temperature. This behaviour is rooted in the inverse-square sensitivity of density to temperature at constant pressure:

$$\frac{d\rho}{dT} = -\frac{p}{RT^2} \tag{2.22}$$

The implications of these findings are significant. The volumetric expansion of the coolant is more pronounced at lower temperatures, as indicated by the larger fractional change in density. This means that for a given temperature increase, the coolant at lower initial temperatures will experience a greater reduction in density, leading to a more substantial increase in velocity and crossflow development.

This effect is compounded by the fact that the momentum ratio increases with the temperature ratio. The momentum ratio is defined as:

$$\mathrm{MR} = \frac{\rho_c V_c^2}{\rho_j V_j^2} \tag{2.23}$$

These findings align qualitatively with the numerical results of Hatta et al. [2, 3], who observed greater jet deflection and crossflow dominance at higher surface temperatures. The present analysis provides a thermodynamic foundation for these observations, revealing that the decline in heat transfer effectiveness is driven not solely by changes in jet momentum but by the temperature-sensitive expansion of the coolant as it interacts with the wall.

In summary, the initial jet temperature T_0 and the final wall-induced temperature T_1 jointly govern the thermofluid behaviour of impingement cooling systems. The magnitude of volumetric expansion, and hence the development of crossflow and jet distortion, is strongly influenced by the temperature ratio and the absolute thermal state of the fluid. These mechanisms provide a physical rationale for the commonly observed deterioration in impingement heat transfer performance at elevated surface temperatures.

2.6.1 Justification for In-Plane Conductive Cooling Channels

The preceding analysis highlights an inherent characteristic of convective impingement cooling systems operating under high thermal loading. High Turbine Entry Temperatures (TET) demand substantial internal and film cooling to keep component temperatures within acceptable limits. However, higher TET inevitably increases the required cooling mass flow rate. Elevated temperature ratios further compound the issue through increased volumetric expansion. As a result, baseline

crossflow in modern gas turbine blades is inherently significant, and effective mitigation remains challenging.

Crossflow momentum disrupts the downstream jets, deflecting them away from their intended impingement zones and degrading heat transfer effectiveness. Despite numerous geometric countermeasures such as corrugations or crossflow diverters, these strategies only partially restore performance and often require complex internal geometries that increase manufacturing burden. Rather than attempting to further optimize convection under increasingly hostile flow conditions, this thesis proposes a shift in paradigm: use conduction to redistribute heat internally, avoiding reliance on disrupted flow altogether.

Instead of transporting thermal energy through the fluid, heat can be redirected within the solid via enhanced in-plane conduction. In this paradigm, heat is conducted laterally from localized hot spots, such as those in downstream regions affected by weak or deflected jets,toward regions with better or optimised impingement cooling.

By deliberately designing high-conductivity pathways within the solid substrate it becomes possible to actively redistribute thermal energy away from regions suffering convective degradation. This strategy harnesses conduction not just as a supplemental effect, but as a primary transport mechanism, which may be particularly effective in scenarios where high crossflow causes severe jet breakdown, such as might be seen in scenarios where cooling air cannot be spent to the blade surface as film cooling. As previously discussed, there are good justifications for seeking to eliminate the use of film cooling altogether, and this approach may be one way to do so.

Moreover, conductive heat transfer scales linearly with temperature gradient and conductivity,

$$\mathbf{q}_{\text{cond}} = -k\nabla T \tag{2.24}$$

and is unaffected by by the channel flow, making it inherently robust under adverse flow conditions. By contrast, convective performance under impingement cooling degrades non-linearly as TR increases and downstream momentum ratios rise.

Thus, the use of in-plane conduction channels offers a physically motivated and structurally simple method for augmenting or replacing traditional convective cooling where it becomes ineffective,particularly in high TR, high crossflow environments typical of advanced gas turbine applications.

2.6.2 Concept Overview and Implementation Approaches

The proposed concept introduces the exploitation of in-plane thermal transport in conjunction with impingement jet cooling to create a more effective 'holistic' blade cooling methodology.

This approach is based on the hypothesis that controlled lateral conduction, supported by appropriately placed jets and thermally conductive pathways, can smooth surface temperature gradients and reduce peak temperatures. Several implementation strategies may be considered:

- Incorporation of high-conductivity inserts or regions within the target material to channel heat laterally.
- Optimization of jet placement to align high-flux regions with areas that can absorb and redistribute heat effectively.
- Hybrid approaches that combine fewer highly optimised jets in conjunction with engineered conduction paths.

The detailed development and evaluation of this concept, including numerical modelling and performance metrics, are presented below.

2.7 Figures of Merit for Holistic Cooling

The following figures of merit are introduced to quantitatively evaluate the performance of the proposed in-plane heat redistribution concept. Unlike traditional spatially-confined metrics such as peak heat flux or local Nusselt number, these indicators provide a more comprehensive assessment of cooling effectiveness across the entire target surface. They capture not only the average thermal load but also spatial variability.

2.7.1 Mean Surface Temperature

The first and most fundamental metric is the *mean surface temperature*, which represents the area-averaged temperature of the cooled surface. It provides a single scalar quantity that reflects the net effectiveness of the cooling system across the entire target area. Lower mean surface temperatures generally correspond to reduced material temperatures, improved component longevity, and greater thermal margin.

$$\bar{T}_s = \frac{1}{A} \int_A T_s(x, y)\, dA \tag{2.25}$$

Here, $\bar{T}_s$ is the mean surface temperature, A is the total surface area under consideration, and $T_s(x, y)$ is the local surface temperature distribution over the two-dimensional plane. This metric is particularly useful when evaluating hybrid cooling strategies, such as those incorporating inserts, which may reduce local hotspots through enhanced heat spreading but result in a higher overall surface temperature. In such cases, the area-averaged temperature becomes a critical measure of performance, offering a more representative basis for comparison across different cooling approaches.

2.7.2 Standard Deviation of Surface Temperature

The second metric is the *standard deviation of surface temperature*, which quantifies the degree of spatial non-uniformity in the surface temperature distribution. While mean temperature gives an average performance measure, standard deviation captures the magnitude of local deviations from that mean which is particularly important in assessing the likelihood and severity of large thermal gradients that can contribute to mechanical stress, fatigue, and material degradation.

$$\sigma_T = \sqrt{\frac{1}{A} \int_A \left(T_s(x, y) - \bar{T}_s \right)^2 \, dA} \tag{2.26}$$

This metric helps identify whether a cooling configuration produces localized hot spots or maintains a uniform surface temperature profile. A lower σ_T implies smoother thermal gradients, which are highly desirable for reducing thermomechanical stress and extending component service life.

Together, these figures of merit allow for a holistic evaluation of surface cooling performance, particularly in cases where the objective is not simply to minimize temperature at one point, but to manage the distribution of thermal energy across the component. They are used throughout this thesis to assess and compare different cooling strategies, including those involving in-plane conduction.

2.8 Summary

This chapter has examined the physics of impingement jet behaviour and channel flow under high thermal loading, with particular emphasis on the influence of temperature ratio and temperature-dependent property variation on crossflow development and cooling performance. The theoretical foundations of classical convective heat transfer correlations have also been revisited, demonstrating how the widely used power-law form for Nusselt number scaling emerges from boundary layer theory and dimensional analysis. This clarification strengthens the basis for interpreting legacy data and contextualising new experimental results. In addition, the chapter introduced a novel concept for in-plane heat redistribution as an alternative to conventional convection-dominated strategies. By reducing thermal non-uniformity through lateral conduction within the target surface, this approach presents a physically motivated pathway for enhancing component protection while reducing dependence on film cooling. Together, these concepts and metrics provide the analytical and conceptual basis for the comparative evaluation presented in the chapters that follow.

3

Literature Review

Increasing gas turbine power output and efficiency will inevitably mean driving the turbine entry temperature higher. Current state of the art for commercially available gas turbines is about $1600°C$. This temperature is already far above acceptable material limits for even high-temperature nickel-based superalloys; the theoretical highest temperature of hydrocarbon combustion at the stoichiometric limit is over $2000°C$. The adiabatic flame temperature of hydrogen, a potential alternative fuel, is higher still. In order to survive such high temperatures, gas turbine blades must be protected from the high temperature combustion products.

This literature review covers, briefly, the history of the evolution of gas turbine blade cooling technology, and more extensively, the history of research into impingement jet cooling, both in general and applied to gas turbine engines. Some gaps in the research are identified as potential for future work. Furthermore, a quick look at the recent advances from additive manufacturing has been done in support of demonstrating a path to realisation for the 2D conduction concept presented in this thesis.

3.1 Efficiency Limits in the Brayton Cycle: Role of Turbine Entry Temperature

The ideal Brayton cycle is governed by the first law of thermodynamics for a steady-flow system:

$$(q_{\text{in}} - q_{\text{out}}) + (w_{\text{in}} - w_{\text{out}}) = h_{\text{exit}} - h_{\text{inlet}} \tag{3.1}$$

For a complete cycle, the fluid returns to its initial thermodynamic state, such that $h_{\text{exit}} = h_{\text{inlet}}$, and the net work output equals the net heat input. Assuming

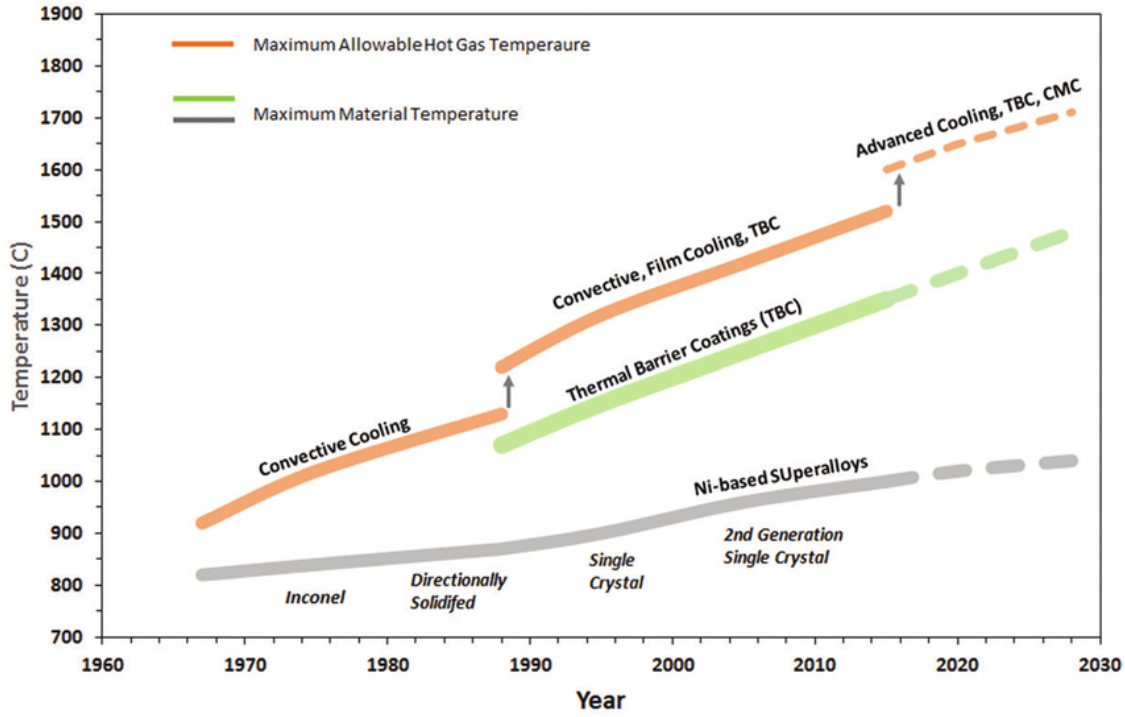

Figure 3.1: Evolution of Technology Developments Allowing Higher Turbine Entry Temperatures. From[4].

ideal gas behaviour and constant specific heat at constant pressure (C_p), the specific enthalpy change is directly related to temperature:

$$C_p = \frac{\delta h}{\delta T}\bigg|_p \tag{3.2}$$

Thus, the thermal efficiency of an ideal Brayton cycle is:

$$\eta_{\text{th,Brayton}} = 1 - \frac{T_4 - T_1}{T_3 - T_2} \tag{3.3}$$

Here, T_1 and T_2 denote compressor inlet and outlet temperatures, and T_3 and T_4 represent turbine inlet and outlet temperatures. The temperature differences across the compressor and turbine stages are connected to the pressure ratio $r_p = P_2/P_1$ via isentropic relations:

$$\frac{T_2}{T_1} = r_p^{(\gamma-1)/\gamma}, \quad \frac{T_4}{T_3} = r_p^{-(\gamma-1)/\gamma} \tag{3.4}$$

From these, it is evident that pressure ratio controls the compression and expansion temperature changes. However, the maximum cycle temperature T_3 is

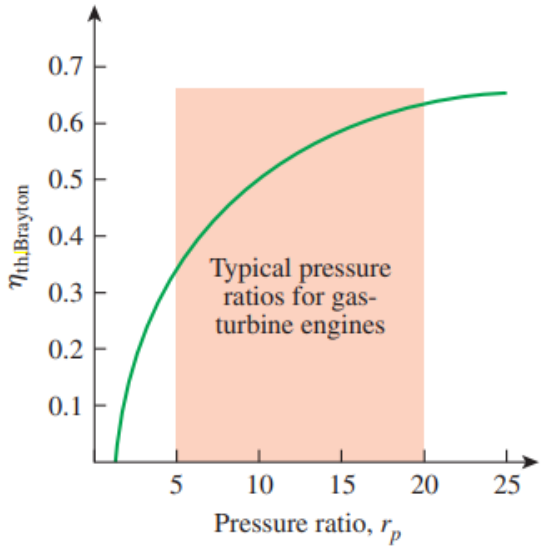

Figure 3.2: Brayton cycle overall thermal efficiency as a function of pressure ratio. Adapted from [5].

not determined by pressure ratio, but by the combustion process, which provides heat input at essentially constant pressure:

$$q_{\text{in}} = C_p(T_3 - T_2) \tag{3.5}$$

The turbine work output is:

$$\dot{W}_{\text{turbine}} = \dot{m}(h_3 - h_4) = \dot{m}C_p(T_3 - T_4) \tag{3.6}$$

where $\dot{m}$ is the mass flow rate, expressible in terms of flow density ρ, velocity V, and area A:

$$\dot{m} = \rho V A, \quad \rho = \frac{P}{RT} \tag{3.7}$$

In the ideal Brayton cycle, increasing the pressure ratio raises T_2 and lowers T_4 (for fixed T_1 and T_3), increasing the enthalpy drop across the turbine and enhancing thermal efficiency. It also reduces the temperature rise across the combustor, $T_3 - T_2$, for a fixed T_3. However, in the ideal cycle, T_3 is not constrained by material or operational limits, and can be increased to maintain or enhance heat input as needed.

3.1.1 Design Limits: Coupling of Pressure Ratio and Turbine Inlet Temperature

In a real engine, however, further increases in pressure ratio result in higher compressor work and reduced margin between T_3 and material limits. As a result, the net work output may begin to decline, and thermal efficiency can degrade beyond an optimal pressure ratio due to practical limitations not captured in the idealised model.

While it may appear that increasing the pressure ratio r_p indefinitely will improve Brayton cycle performance by increasing the enthalpy drop across the turbine and enhancing thermal efficiency, this gain is fundamentally constrained by the turbine inlet temperature T_3. In the ideal cycle, combustion occurs at constant pressure and raises the gas temperature from the compressor exit (T_2) to the turbine inlet (T_3). For a given T_3, increasing r_p raises T_2, which reduces the temperature rise available during combustion ($T_3 - T_2$) and thus the heat input $q_{\text{in}} = C_p(T_3 - T_2)$. As T_2 approaches T_3, both the heat addition and net work output tend toward zero, even as thermal efficiency approaches a theoretical maximum. If T_2 were to exceed T_3, the cycle becomes unphysical, and the efficiency expression itself begins to decline, highlighting a mathematical peak that marks the boundary of viability.

In a real engine, however, both T_3 and T_2 are constrained by distinct physical limitations. The maximum turbine inlet temperature T_3 is limited by combustion conditions, material capability, and available cooling technology. Meanwhile, T_2 is constrained by the achievable pressure ratio, which is in turn limited by compressor efficiency, mechanical tolerances, and system mass flow considerations.

The designer must therefore balance these two independent limits while selecting a pressure ratio r_p that optimises both thermal efficiency and specific work output. The ideal Brayton cycle provides a framework for understanding these relationships, but real-world performance depends critically on how these competing constraints are managed through materials, geometry, and system integration.

In summary, while classical Brayton cycle analysis emphasizes pressure ratio as a lever for improving efficiency, real gas turbine performance is fundamentally limited by the maximum allowable turbine entry temperature. This parameter governs not only the energy addition in combustion but also the extent to which

enthalpy can be extracted during expansion. Therefore, meaningful improvements in thermal efficiency and specific work output require technologies that raise T_3 safely. Advanced cooling strategies and high-temperature materials, rather than indefinite increases in pressure ratio, are the key to these improvements.

3.2 A Brief History of Gas Turbine Blade Cooling

Early gas turbine engines operated at turbine entry temperatures on the order of $600°C$ to $800°C$ and thermal efficiencies of approximately 15%-20% [6]. At these temperatures, turbine blades did not have to be cooled, but engine longevity was an issue because the engines operated near the creep temperature of common engineering alloys, and rotating turbine blades experience a great deal of mechanical stress.

As technology advanced and manufacturers pushed to higher turbine inlet temperatures, other strategies were needed to extend engine life and prevent catastrophic failures. In a very general sense, operation of gas turbine engines at very high turbine entry temperatures has been made possible with three enabling technologies: high temperature materials, thermal barrier coatings and internal convective cooling.

3.2.1 High Temperature Materials

Early efforts to improve engine reliability on gas turbine engines focused on development of alloys that could withstand high temperatures. However, as is evident from Figure 3.1, a large capability gap has existed between allowable metal temperature and turbine entry temperature (TET). Even the most advanced modern super alloys with single-crystal manufacturing have allowable metal temperatures well below current commercial turbine inlet temperatures. There is clearly a 'capability' gap for turbine materials despite massive advances over the past several decades. Thus, material development plays only a secondary role in allowing increasing turbine entry temperatures.

3.2.2 Thermal Barrier Coatings.

Ceramics are a well known class of electrically and thermally insulative materials. Thin layers of ceramics are used on turbine blade surfaces as thermal barrier coatings (TBC) to insulate the blade metal from the high temperature combustion products. Temperature drops of approximately $100°C$ between the hot gas and blade surface can be obtained with only $500\mu m$ of TBC coating[7]. Using even thin layers of materials like yttria-stabilised zirconia (YSZ) reduces metal temperatures significantly.

TBCs are a key enabling technology for allowing increasing TETs, but are very brittle and highly subject to damage. Additionally, there are problems with material adhesion which can result in local loss of barrier material on blade surfaces.

3.2.3 Convection Cooling of Blades

The key enabling technology that has allowed higher temperature operation of gas turbines is forced convection cooling of turbine blades. It is relevant to this research project to understand the trajectory of development of convection cooling over the past 90 years or so to understand why impingement jet cooling is important.

Turbine blade cooling is achieved by bleeding air off of the compressor prior to the combustor and flowing that air through the turbine blades and to the blade surface where it cools the blade. However, using compressor air to cool the turbine blades naturally results in losses to the engine, because 20%-30% of the compressor discharge is used for aggressive cooling of turbine blades[8]. This is air that could otherwise be used to burn fuel. Furthermore, the cool air is injected into the turbine combustion, reducing the engine output and thermal efficiency. So, there is a trade-off between cooling the turbine blades and extracting the maximum energy from the engine. Future work in this area will focus on increasing cooling effectiveness to reduce the amount of cooling air needed.

Blade convective cooling consists, in general, of 2 key technologies: Internal convective cooling and external surface film cooling, and there are many configurations and combinations in commercial use.

Film cooling is achieved when cooling air is ejected to the surface of a turbine blade to form a 'film' of cooler air, which shields the blade from the higher temperature combustion products. Film cooling can be well understood by comparing

convective heat flux to a turbine blade surface with and without the presence of a cooling film. Convective heat transfer is driven by the temperature difference between the adiabatic wall temperature and some reference free stream temperature.

In the case without a film of cooling air, Newton's law of convective cooling defines the heat transfer between the free stream fluid and blade surface

$$q_0'' = h_0(T_{\text{inf}} - T_w) \tag{3.8}$$

Cooling air ejected from the blade mixes with the near wall main flow and cools it. It is therefore apparent from equation 3.8 that any reduction in the free stream fluid adjacent to the wall will reduce the heat flux to the wall.

However, injection of the cooling flow into the near wall flow can affect the heat transfer coefficient h. In fact, injection of cooling air into the near wall flow often increases local heat transfer effect[8] which is disadvantageous. Film cooling is therefore a very complex phenomenon, and careful analysis must be done for each gas turbine application.

A typical configuration for turbine blade cooling, including film, internal and impingement jet cooling is shown in Figure 3.3.Cooling air enters the root of the blade at two locations, marked as 1 and 4. At location 2, some of the cooling flow is forced through holes to create jets that impinge on the inner surface of the blade leading edge where the blade experiences the highest temperature. The remaining internal flow passes over extended surfaces inside the channel which enhance heat transfer. In this illustration, rib turbulators and pin-fin arrays are shown at locations 2, 5 and 6. For cooling flow paths 2 and 4, the cooling air then exits the blade at the blade trailing edge. At location 3 shown on Figure 3.3 the cooling air is ejected through holes at the leading edge to provide a film of cooling air for the blade, which insulates the blade from the hot gas flow. Impingement jet cooling is used in locations where very high heat transfer is needed, such as the inside of the leading edge of the blade.

Figure 3.3 is meant to illustrate the different components of convective blade cooling and is representative only. There are many possible configurations for internal cooling, and different manufacturers use different internal features or use impingement jets at other chord wise positions in addition to at the leading edge.

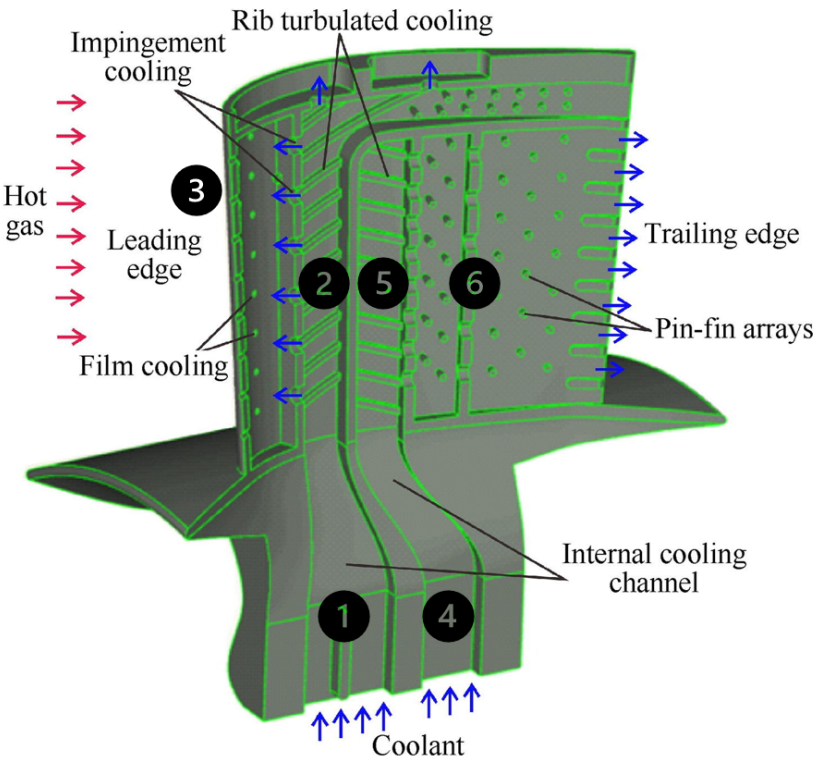

Figure 3.3: Illustration of typical modern internal turbine blade cooling configuration. From[9].

In fact, different internal configurations may be used in the same engine for blades at different axial stages. The stagnation surfaces for the internal impingement jets may also be treated with additional surface roughness or other surface modifications to enhance heat transfer in those locations.

3.3 Jet Impingement Cooling

The flow and heat transfer of impingement jets is very complicated, and heat transfer is a strong function of the geometry of the jet and jet/target spacing. The flow and heat transfer characteristics of a single jet impinging on a flat plate has been extensively studied and is well understood[10]. A representation of the flow field of a single jet is shown in Figure 3.4. Impingement jets flow is described by convention as having 3 distinct flow regions: free jet region, stagnation or impingement region, and wall jet region.

The free jet region is further broken down into 3 distinct regions: potential core, developing zone and fully developed zone. In general terms, the fluid flow of an

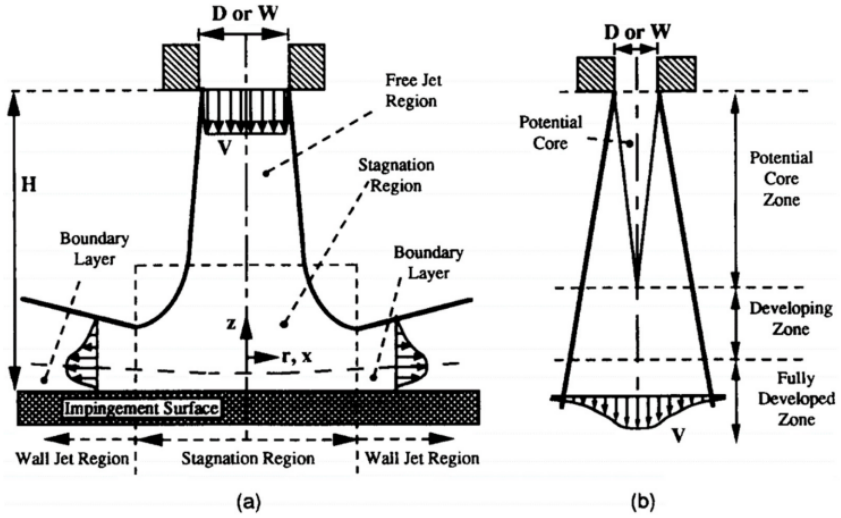

Figure 3.4: Illustration of Jet Flow Regions. (a)Full jet/wall interaction, (b)Free jet region detail. From[11].

impinging jet can be explained in the following fashion:

The well formed high-velocity potential core of the jet exits the nozzle and immediately begins to entrain air at the boundary between the jet and the surrounding fluid. The entrainment reduces the overall jet velocity and gives rise to vortices in the region between the core and surrounding fluid. If the distance between the jet nozzle and the target plate is kept below 6, i.e. $z/d \leq 6$, at least some of the high velocity high momentum jet potential core reaches the target plate and develops a flow stagnation region. The flow then accelerates radially from the stagnation region and a thin boundary layer begins to develop. The stagnating potential core starts a boundary layer of thickness of $\cong 0.02d$, which results in very good heat transfer in this region.

The jet fluid flow field and heat transfer coefficient are governed by a complex relationship between a number of parameters including nozzle geometry, jet exit Reynolds number and distance to the target plate. It is conventional to describe all geometrical parameters as non-dimensional ratios of the diameter, d. For example, the spacing from the bottom of the jet plate to the top of the target surface is most commonly given by the ratio h/d. There is no way to generalise the heat transfer of impingement jets in terms of length or growth of the different regions, as the jet flow field is highly dependent on geometry. However, a number of different empirical correlations have been established for describing the heat transfer for

a single jet in terms of jet and target plate geometry. These correlations are generally in the form of power-laws relating non-dimensional fluid parameters. Most commonly these correlations involve a relationship between the Nusselt Number and Prandtl number of the flow and fluid.

Martin[12] provides a basis for predicting the heat transfer of a single impinging jet using a normalised Nusselt number correlation. The following widely used formulation is based on his data:

$$\frac{\overline{Nu}}{Pr^{0.42}} = G\left(\frac{r}{d}, \frac{h}{d}\right) F_1(Re) \tag{3.9}$$

Where

$$F_1 = 2Re^{\frac{1}{2}}(1 + 0.005Re^{0.55})^{\frac{1}{2}} \tag{3.10}$$

and

$$G = \frac{d}{r}\frac{1 - 1.1d/r}{1 + 0.1(h/d - 6)d/r} \tag{3.11}$$

A vast body of work has been done with parametric studies of nozzle geometry, jet impingement angle, Jet Reynolds number and jet height to establish empirical relationships which correlate the flow Nusselt Number to fluid Prandtl Number. Terzis[13] has compiled relations from a number of sources and presented them in graphical format.

Figure 3.5 shows a typical plot of jet heat transfer power-law versus the non-dimensionalised radial distance from the stagnation region on the target plate. In general, cooling effectiveness is highest at the stagnation point with higher Reynolds number jet flow producing better cooling. This is intuitive. For most geometries, cooling effectiveness drops off rapidly with distance from the jet stagnation point as the flow transitions from jet to wall flow and a thermal boundary layer develops in the fluid.

Figures 3.5 and 3.6 present essentially the same dataset, with Figure 3.5 holding the channel height-to-diameter ratio (Z/D) constant, and Figure 3.6 allowing Z to vary. It is conventional to present power-law relationships for jet cooling effectiveness in multiple forms to highlight functional dependence on key parameters. Notably, Figure 3.6 shows a distinct peak in local jet Nusselt number at some radial offset from the jet centreline for the smallest Z/D. This suggests that, at very small

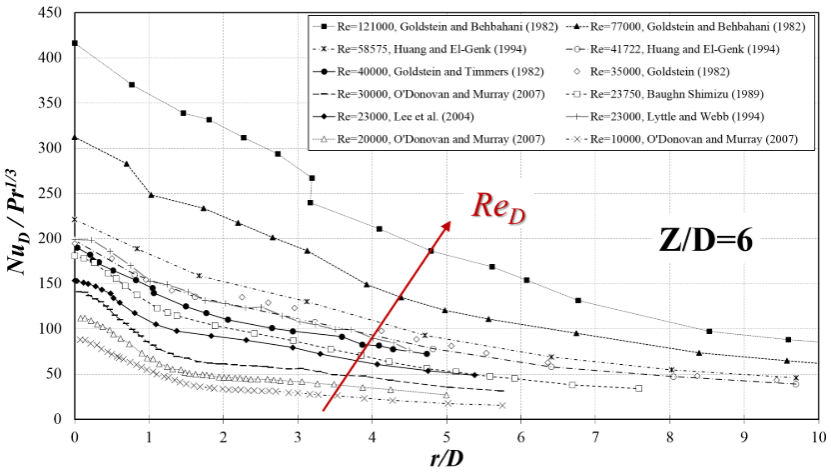

Figure 3.5: Array heat transfer with constant non-dimensional height. From[13].

channel heights and high Reynolds numbers, a jet is never developed. Instead, the observed peak indicates a transition to turbulent channel flow, which locally enhances heat transfer. These results highlight the critical role of channel geometry in governing flow development and cooling performance.

In addition to varying jet/plate height, many other parameters have been examined in dozens of studies. Examples include studies of heat transfer of single jets impinging on a single plate with different fluids[14], different nozzle geometries[15][16], varying jet impingement angle[17], target plate surface modifications[18][19] and jet/wall temperature ratio[20]. Xu [21]and Geng[22] study heat transfer of synthetic jets. Synthetic jets are created by moving air already available inside the cavity with some internal mechanism like a piezo-actuator or some other mechanical device. In essence, synthetic jets can redirect existing cooling flow into impingement jets without the introduction of additional coolant at high pressure. However, it has not yet been demonstrated that active synthetic jet mechanisms can be built for the harsh environment of gas turbine internal cooling. Furthermore, as the temperature of the ambient cooling fluid increases due to interaction with hot components, the temperature of synthetic jets increases correspondingly. This means that the driving temperature difference between the synthetic jet and hot target surface is reduced. This is not a problem for traditional impingement jets, which are continuously replenished with fresh fluid. The authors of these studies conclude that synthetic jets are not as effective as real jets for cooling applications[22].

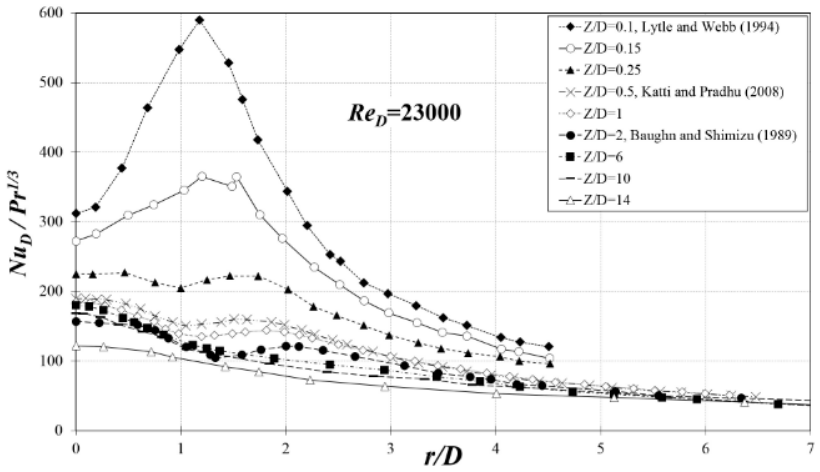

Figure 3.6: Effect of h/d on jet heat transfer. From[13].

3.4 Arrays of Impingement Jets

In applications where a large area or a number of discrete locations require enhanced cooling load, arrays of impingement jets are commonly employed. This is true for internal cooling of gas turbine blades. Fluid flow fields for impingement jet arrays are much more complicated than for single jets because the flow from individual jets can interact and interfere with each other.

Correlations for the flow field and heat transfer performance of impinging jet arrays are well covered in the literature. Many of the same enhancement strategies developed for single-jet systems, such as surface roughness, confinement, and target plate geometry, have been extended to jet arrays. Comprehensive reviews are available in the works of Jambunathan [10] and Plant [23], which summarise decades of experimental and analytical developments. For the present study, however, the early foundational work of Florschuetz et al. [24–26] and Kercher [27] provided the most directly applicable correlations and were used extensively during rig design and analysis.

3.4.1 Florschuetz Flow and Heat Transfer Correlations

Florschuetz et al. developed a widely adopted set of correlations describing flow field development and heat transfer performance in impinging jet arrays with crossflow. These correlations. along with subsequent refinements by Gillespie [28], were used during the rig sizing and planning stages of this project.

Florschuetz's flowfield model is based on a continuous-injection mass flux formulation and is supported by extensive experimental validation. The local crossflow-to-jet mass flux ratio, G_c/G_j, was shown to follow a hyperbolic function of streamwise position:

$$\frac{G_c}{G_j} = \frac{1}{\sqrt{2} \cdot C_D} \frac{\sinh\left[\beta(x/x_n - 1/2)\right]}{\cosh\left[\beta(x/x_n)\right]} \tag{3.12}$$

where β captures the geometrical parameters of the array.

$$\beta = C_D\sqrt{2}(\pi/4)/[(y_n/d)(z/d)] \tag{3.13}$$

Here, x/x_n is the non-dimensional streamwise location based on jet pitch, y_n/d and z/d are the spanwise jet pitch and non-dimensional channel height respectively, and C_D is the coefficient of discharge for each jet. Notably, Florschuetz makes no distinction between uniform and staggered jet arrays in this flowfield model; the mass flux is additive row-by-row in the streamwise direction, and the influence of array configuration enters indirectly through geometric parameters.

To link flow development with thermal performance, Florschuetz proposed a Nusselt number correlation of the form:

$$Nu = A \cdot Re_j^m \cdot \left\{1 - B\left[(z/d) \cdot \left(\frac{G_c}{G_j}\right)\right]^n\right\} \cdot Pr^{1/3} \tag{3.14}$$

where A, m, B, and n are empirically derived coefficients dependent on the jet array geometry (uniform or staggered), and are tabulated in Florschuetz et al. (1981) [25]. These correlations relate local convective performance directly to both the developing crossflow and the fundamental geometric parameters of the array: x/d, y/d, and z/d. Notably, examination of the exponent m across different geometries shows that the dependence of Nusselt number on jet Reynolds number and Prandtl number is consistent with canonical power-law behaviour, reinforcing that Florschuetz' formulation captures the underlying physics with a high degree of fidelity.

A full derivation of these expressions is beyond the scope of this thesis, but they were used extensively in the conceptual sizing and performance benchmarking of the present experimental rig.

3.5 Channel Effects in Turbine Blade Cooling

Manufacture of the internal cooling channels for turbine blades is accomplished either during casting or by use of an insert that fits inside of a partially hollow blade. Before exiting the blade through cooling holes if film cooling is used, the cooling flow is retained in internal channels where channel effects become significant.

3.5.1 Development of Channel Crossflow

A common internal cooling configuration is to have the 'first row' of cooling jets impinging on the inside of a blade just inside the stagnation line. This gives maximum ΔT for HTC at this location. Figure 3.7 shows leading edge and mid-chord impingement jet flow exiting the blade after traversing internal channels. The mid-chord impingement cooling shown in Figure 3.7 extends radially (into and out of the page on the diagram) and thus constitutes an array of impingement jets. Channel crossflow is additive, and each jet in turn will contribute to the total mass flow in the channel, creating a large mass flux crossflow. This crossflow can become so strong in the internal passages that the downstream jets can be deflected downstream as a vector addition of the jet flow and the crossflow. This can result in a reduction of the stagnation on the internal target surface. If this occurs, cooling effectiveness is drastically reduced[25] because the formation of the jet stagnation zone on the target plate is destroyed. An example of this can be seen in Figure 3.8 where the downstream jet local heat transfer at the surface becomes diminished and asymmetrical. The authors of this study concluded that the loss of jet heat transfer effectiveness was because the structure of the impinging jets is affected by the developing channel crossflow[29].

3.5.2 Jet Array Interaction Effects in Channels

Impingement jet arrays create additional flow complexity in channel flow because of interaction between adjacent jets[30], and the correlations for cooling effectiveness become much more complicated. Careful control of spacing is required to ensure that regions of reduced heat transfer are not created in regions where recirculation is present.

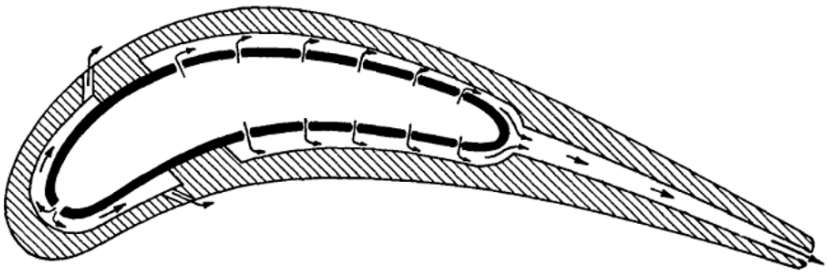

Figure 3.7: Development of channel flow from impingement jets in gas turbine blade. From[24].

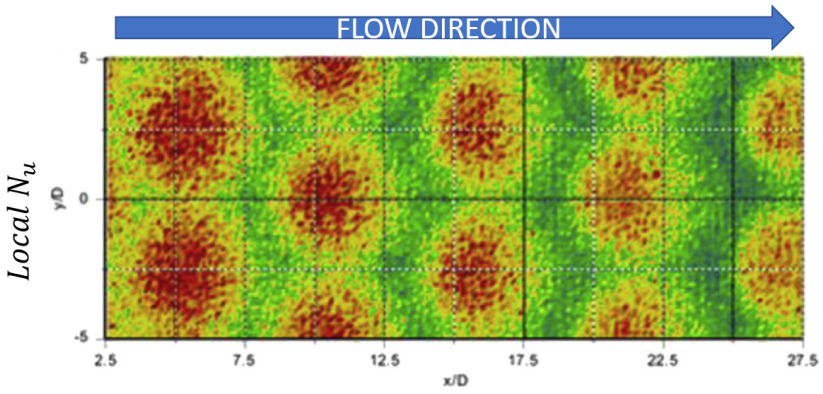

Figure 3.8: Reduced Cooling Effectiveness downstream caused by crossflow disruption of jets. Re=30,000. z/d=5.0 From[29].

3.5.3 Mitigation of Disruption of Jets by Channel Crossflow

The most common strategy for mitigating the disruption of impingement jets by channel crossflow is to transition from an impingement cooling regime to an optimised channel cooling regime once the crossflow velocity becomes large enough to deflect or destabilise the jets [31]. While originally proposed for combustor cooling, the principle also applies to blade internal cooling.

Ji and Singh [32] attempted to control crossflow development by varying the jet array hole diameters along the streamwise direction. However, they did not account for the mismatch in jet sizing relative to the constant channel height, which reduced cooling effectiveness downstream. In contrast, Wang and Sunden [33] used channel wall turbulators to pre-condition the flow upstream of the jets. They found that these structures reduced jet disruption by the developing crossflow. Their approach appears compatible with existing extended surface manufacturing methods.

More recently, Hatta [3] demonstrated that crossflow can be passively mitigated by replacing the flat jet plate with a corrugated or "castellated" configuration. This

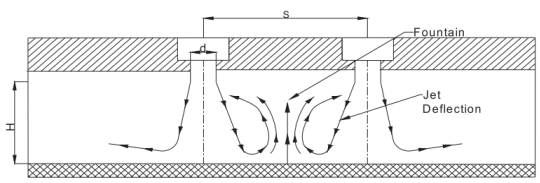

Figure 3.9: Impingement jet interaction in channel flow. From[30].

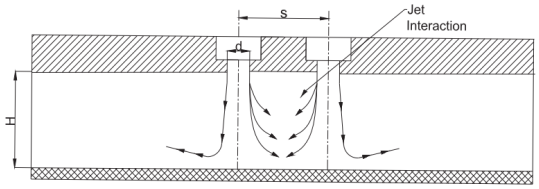

Figure 3.10: Impingement jet interference for reduced jet spacing. From[30].

increases the local channel cross-sectional area, thereby reducing the mean velocity of the crossflow and possible deleterious deflection of jets.

Figures 3.9 and 3.10 illustrate how spanwise-adjacent jets interact as a function of spacing. At larger spacings, wall jets from adjacent impingement zones form a central "fountain" region with upward-directed flow. Aligning the valleys of a castellated plate with these fountain regions could offer a synergistic crossflow mitigation strategy.

This hypothesis could be tested through targeted future study.

3.6 Target Surface Modifications

When the total channel flow becomes high enough that disruption of downstream jets occurs, manufacturers often change cooling strategies to enhance the convective cooling of the channel flow, rather than relying on impingement cooling. One of the most effective ways to enhance convective heat transfer coupling to a surface is to install an 'extended surface' like a pin or fin, or to modify the surface with some texturing or roughness. Extended surfaces and surface roughness application both increase the wetted surface area of the object, and can affect the fluid flow to promote turbulence which enhances heat transfer locally. They may also promote flow separation and reattachment, restarting the boundary layer. Both rib turbulators and pin fin arrays are seen in Figure 3.3. Due to the manufacturing constrains in the investment casting process, rib turbulators and pin fin arrays seem to be the current state of the art[8].

3.6.1 Dominance of Rib Turbulators and Pin Fin Arrays

Rib turbulators and pin fin arrays are the most common extended surfaces used in gas turbine blade cooling applications. They are used in the internal channels of turbine blades, and are also used in the combustor liner. The use of rib turbulators and pin fins is well established in the literature.

Structurally, rib turbulators and pin-fin arrays provide excellent mechanical integrity, ensuring durability under the extreme centrifugal and thermal stresses experienced by turbine blades. Additionally, decades of practical experience have resulted in well-developed empirical correlations and design guidelines, significantly simplifying analysis, performance prediction, and optimization. Standard undergraduate-level heat transfer and fluid mechanics methodologies are directly applicable, facilitating straightforward analytical modelling and rapid iterative design improvements.

However, these extended surfaces are limited to the manufacturing techniques available for gas turbine blades. The investment casting process is limited to a few geometries, and while rib turbulators and pin fins can be manufactured with this process, other surface modifications cannot be manufactured with current techniques.

While newer methods enabled by additive manufacturing offer potential improvements through more complex cooling geometries, their adoption remains constrained by cost, scalability, material qualification requirements, and the current complexity of predictive modelling. Consequently, the established effectiveness, analytical simplicity, reliability, and manufacturing convenience of rib turbulators and pin-fin arrays ensure their continued dominance in gas turbine cooling strategies.

3.6.2 Other Surface Modifications

Hanson and Webb[34] are among the earliest to do a systematic study of different types of extended surfaces for jet impingement cooling. They studied square pin arrays, concentric circles and pyramidal fins of varying geometries and found that overall heat transfer could be enhanced by 1.5-4.5 times by use of extended surfaces. Gabour and Leinhard[35] studied wall roughness at levels that corresponded to standard casting manufacturing processes and were able to increase local heat transfer by 50%. This points to a potentially easy enhancement of internal heat

transfer by control of the casting process. Taslim et al.[36] studied heat transfer enhancement with a novel geometry on a concave surface simulating a leading edge impingement zone. They found that it was possible to enhance heat transfer by 30% over a datum smooth wall. Jeffers et al.[37] manufactured large complex macroscopic elements at the jet impingement site and found that enhancements of up to 2.2x were possible.

There are many such studies in the literature, and while it is currently impossible to manufacture many of the studied impingement surface modifications in internal cooling passages, the literature does point to the kinds of features that can be used in the future as manufacturing processes improve.

3.7 Temperature Ratio Effects on Impingement Jet Heat Transfer

While most experimental and numerical studies of impingement jet cooling focus on geometric and flow field parameters, relatively few have addressed the influence of wall-to-jet temperature ratio (TR = T_w/T_j) on cooling performance.

Goodro et al.[38] conducted one of the few experimental investigations into this phenomenon, studying jet arrays at temperature ratios up to 1.73. They observed a consistent decrease in Nusselt number with increasing TR across all configurations tested. This trend was attributed to changes in fluid properties at elevated wall temperatures, but no specific mechanism was identified or confirmed. Their findings were among the first to show that temperature ratio has an impact on jet cooling effectiveness.

More recently, Hatta et al.[2, 3] used RANS-based numerical simulations to explore this effect in more detail. Their work showed that as temperature ratio increases, the heated fluid undergoes volumetric expansion, accelerating the crossflow and weakening subsequent impingement jets. Their simulations showed that at high TR, momentum ratio increases substantially, leading to greater jet deflection and lower local heat transfer coefficients.

While Goodro established the experimental trend and Hatta quantified its aerodynamic consequences, the underlying thermophysical mechanisms were not

fully explored. The present thesis builds on this body of work by developing a first-principles explanation of how temperature ratio and absolute jet temperature govern volumetric expansion, which leads to crossflow acceleration. This work also looks at sensitivity of material properties to temperature and offers a deeper explanation for the performance degradation observed in both prior studies.

3.8 Effects of Convective Cooling on Overall Engine Efficiency

As previously shown, the overall thermal efficiency of a gas turbine is limited, from a practical standpoint, by limits on turbine entry temperature (TET), engine compression ratio and the isentropic efficiencies of the engine components. However, ejecting cooling into the main flow does affect the main flow. There are thought to be three possible mechanisms that use of film and convective cooling can reduce engine efficiency:

1. Ejection of cooling air increases aerodynamic drag of blades.

2. Cooling flow ejected from the first stator row lowers the stagnation pressure of the main fluid entering the first rotor stage.

3. Cooling flow is a source of entropy generation in the main flow.

Pressure losses due to coolant injection into the main flow was shown by Hartsel[39] to relate to the temperature and velocity ratios between the main flow and the coolant.

$$\frac{\Delta P}{P} \approx -\frac{\gamma}{2}\frac{W_c}{W_g}Ma_g^2\left[1+\frac{T_{tc}}{T_{tg}}-2\frac{V_c}{V_g}cos\phi_c\right] \tag{3.15}$$

Horlock et al.[40] conclude that there will be a practical limit for driving engine overall efficiency by increasing TET. The thermodynamic losses which occur in the engine for cooling at higher TETs will eventually cost so much that the 'gains in thermal efficiency with increasing TET can become marginal.

The inlet enthalpy of the coolant and the mainstream gas must be accounted for in generating the stage efficiency, while the exit flow may be treated as mixed out flow. Thus methods to compute efficiency are complex.

3.9 Exploitation of In Wall Conduction

Because of channel crossflow, truly effective impingement cooling may be limited to a single row of jets, or a small number of rows. Once crossflow effects are large enough to render impingement ineffective, the cooling strategy must change to a channel flow cooling strategy. This is not ideal, as the impingement jets are very effective at removing heat from the target surface. The use of channel flow cooling is a compromise that reduces the overall cooling effectiveness of the blade.

In the standard approach to jet impingement cooling, researchers have focused on an approach that is a balance between impingement jet and channel cooling. This involves the modification of channel geometry, jet array layouts, surface enhancements and methods to mitigate jet crossflow interference for as long as possible. While these techniques (e.g., castellated plates, macro-structures, various jet orientations) can indeed preserve or improve local cooling effectiveness, a more holistic strategy, proposed here, is to embed high-conductivity 'heat channels' within the target wall.

Specifically, the concept envisions a composite or additively manufactured target wall embedded with regions of higher thermal conductivity material. These internal conduction paths would transfer heat from zones receiving less direct impingement cooling (e.g., downstream jets suffering crossflow) to upstream regions with stronger local impingement or higher convective cooling coefficients. Because conduction typically outperforms convection for short-range heat transfer within solids, an inlay of high-conductivity material could improve overall cooling, rendering crossflow effects less limiting. In practice, this could be achieved by focusing on a single (or fewer) zone(s) of highly effective impingement, relying on the conduction network to distribute and remove heat.

Such an approach reduces or eliminates the need for complex crossflow mitigation. Recent advances in additive manufacturing (AM), particularly multi-material AM, underpin the feasibility of implementing conduction-enhancing channels.

Studies of polymer-based AM by Elkholy et al. [41] show that even modest adjustments to layer orientation, raster geometry, and filler content can yield anisotropically high thermal conductivity. Jia et al.[42] demonstrated a 3D-printed heat sink in a thermally conductive graphite-polymer composite, achieving cooling efficacy comparable to an aluminum baseline, while Hymas et al. [43] introduced a hybrid technique embedding metallic strips into fused-deposition-modelled polymer heat exchangers.

Both highlight that careful choice of filler and raster pattern can form conduction sub-networks in low-conductivity matrices. Furthermore, Kalsoom et al. [44] showed how stereolithography-based composites with embedded diamond fillers can deliver superior heat dissipation. Although such polymer composites rarely match fully metallic conductivities, they still illustrate the growing capacity to engineer internal conduction pathways via AM.

Meanwhile, multi-material perspectives from Zhang et al. [19] emphasize merging dissimilar materials, such as metals and high-temperature alloys, within a single build, thereby enabling "veins" of inherently higher conductivity. Bandyopadhyay and Heer [45] likewise stress that multi-material AM can integrate multiple alloys, ceramics, or functional gradients in a single monolithic part. As processing equipment matures to accommodate dissimilar melt pools ([46]), these processes become increasingly relevant for deploying metallic conduction channels inside turbine-blade superalloys. Notably, functional grading and advanced design strategies (e.g., localized copper patches within an Inconel or steel matrix) support the idea that conduction optimization can be realized through topology-oriented manufacturing rather than purely fluid mechanic means.

Overall, demonstrations of polymer composites with improved conductivity, combined with multi-metal printing, bolster the premise that carefully engineered 'heat channels' could substantially enhance turbine-blade cooling. Due to time and budgetary constraints, this idea was not explored directly in this work. Nevertheless, the base concept has been demonstrated numerically and offers a clear justification for further development. While challenges such as large-scale build integration, void control, and high-temperature mechanical integrity remain, ongoing technological advances suggest that conduction-optimized, holistically cooled blades could become practical in the near future.

3.10 Gaps In the Literature and Future Work

While significant progress has been made in the understanding and modelling of jet impingement cooling, several important gaps remain. Much of the existing literature focuses on laboratory-scale experiments conducted at relatively moderate temperatures and with simplified geometries. There is a lack of comprehensive studies investigating impingement cooling performance under engine-realistic conditions, including elevated temperatures, high pressure ratios, and reactive flow. At these conditions, fluid properties such as viscosity and density deviate substantially from low-temperature air, which may lead to different flow regimes and heat transfer behaviour than those predicted by canonical data and research.

Additionally, most studies exploring the mitigation of crossflow effects in jet arrays were conducted before additive manufacturing (AM) became a viable production method for gas turbine blades. These earlier works often relied on conventional manufacturing constraints that limited geometric complexity. With the maturation of AM technologies, particularly in multi-material and topology-optimized builds, there is now a compelling opportunity to revisit internal cooling strategies. New configurations, such as castellated jet plates, integrated heat channels, or transitional flow passages, can be designed and manufactured in ways that were previously impossible.

A particularly important area for future research is the exploitation of additive manufacturing to engineer anisotropic thermal conductivity within the blade material. The in-plane conduction concept proposed in this work depends not only on increasing absolute thermal conductivity, but also on preferentially directing heat laterally within the wall, away from regions of poor convective coverage. Such directional heat transport could be achieved by embedding high-conductivity veins, layering composite materials, or aligning thermally conductive phases during fabrication. These strategies are currently impractical using traditional manufacturing methods but are becoming increasingly feasible through advanced AM techniques, including multi-material printing and controlled microstructure orientation. Realizing this vision will require interdisciplinary collaboration between materials science, heat transfer, and manufacturing research communities, but the potential performance gains could be substantial.

4

Experimental Facility

4.1 Overview of Experimental Objectives

Building on the theoretical framework and literature survey presented in the previous chapters, a bespoke experimental facility was developed to explore the geometric and flow parameters of interest. This chapter describes the development and commissioning of that facility, and discusses constraints in supply, materials, and capabilities discovered during the scoping exercise.

The primary objective of this study was to develop a well-conditioned controlled experimental facility capable of allowing careful investigations into the heat transfer characteristics of jet impingement cooling arrays under varying flow and geometry configurations. The rig was designed specifically to allow initial crossflow development upstream of the impingement array. Figure 4.1 shows a schematic block diagram of the experimental facility. The building main 10 bar air supply compressor is used to provide working fluid, and proved to be adequate for all experimental conditions, including the highest target jet Reynolds Number of Re = 20,000.

Figure 4.2 shows an annotated photograph of the rig, which was designed to allow for a wide range of flow conditions and temperature ratios. The rig was designed to be modular, allowing for easy replacement of the jet plate and other components to accommodate different geometries and flow conditions.

Figures 4.2 and 4.4 provide complementary views of the physical and functional layout of the rig, respectively. These are referred to throughout this chapter to contextualize the components discussed.

To ensure experimental validity, initial validation testing was conducted using a flat jet plate geometry consistent with canonical historical studies reported in the literature [24][25][26][27][38]. This allowed for direct comparison with historical data and provided a baseline for subsequent investigations. The rig was designed to be modular primarily to support testing of a corrugated (castellated) jet plate concept

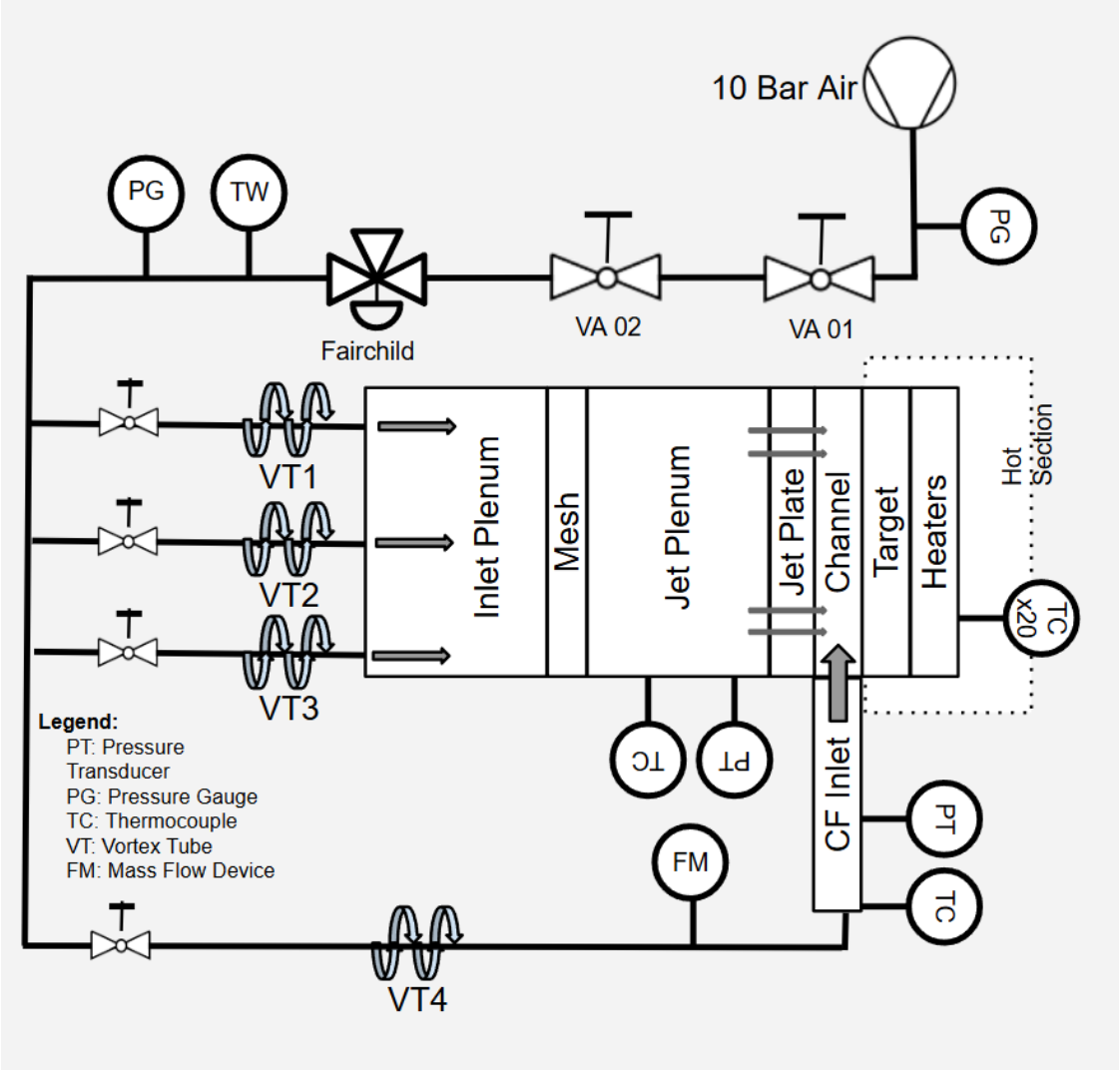

Figure 4.1: Schematic Block Diagram of the Experimental Facility.

proposed by Mitsubishi Heavy Industries (MHI), which was designed to mitigate crossflow-induced degradation of jet cooling effectiveness. The modularity will allow further studies focusing on varying geometry, flow conditions and temperature ratios. Figure 4.3 shows the canonical nomenclature and geometry conventions as described by Florschuetz. These conventions are followed in this work.

Figure 4.2: Annotated photograph of the assembled experimental apparatus. Key components are indicated with numbered callouts: (1) Crossflow inlet plenum, (2) Crossflow converging nozzle, (3) Crossflow channel, (4) Main jet plenum, (5) Jet inlet flow-straightener cassette, (6) As-built vortex tube inlet location (side-mounted), and (7) Heated working section.

4.2 Design Philosophy and Thermal Measurement Method

The overall approach adopted in this work follows an empirical steady-state methodology based on local application of Newton's Law of Cooling. The copper target plate is subdivided into ten individual segments, each independently heated by a 900 W mica heater. The target surface is maintained in a nearly isothermal condition during experiments via PID control, enabling local heat flux measurements

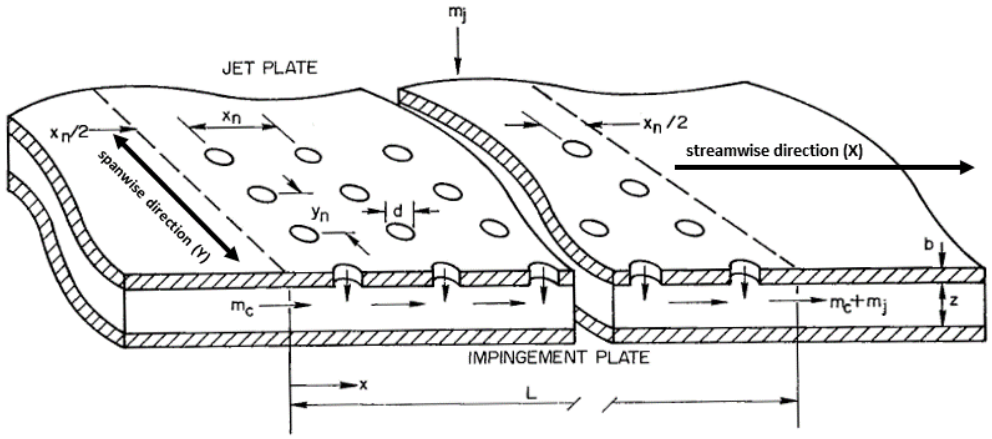

Figure 4.3: Canonical Jet Plate Geometry Nomenclature.

under controlled thermal boundary conditions.

To expand the achievable range of temperature ratios, which was one of the principal objectives of the rig design, a provision was made to cool the working fluid below ambient. This was accomplished by repurposing a set of legacy vortex tubes to pre-cool the supply air to the main jet and crossflow plenums.

Vortex tubes operate by separating a compressed air stream into distinct hot and cold fractions via a swirling flow field, governed by conservation of angular momentum and radial pressure gradients. While the underlying mechanisms are complex, their thermodynamic behaviour is well-documented. For the present work, the inherent characteristics of the vortex tubes imposed two key experimental limitations.

First, the jet Reynolds number was set by pressurizing the jet plenum to a prescribed value. However, this same pressure determined the pressure drop across the vortex tubes, and thus influenced the cold-side outlet temperature. As a result, the minimum attainable coolant temperature varied with Reynolds number selection.

Second, since a portion of the supply air is diverted to a separate hot exhaust stream, it was not possible to directly measure the mass flow rate of cooling air into the plenums without high-accuracy, high-flow mass flow sensors installed on the inlet and outlets of each vortex tube. This was beyond the available budget for this project.

In practice, the lowest air temperature achieved was approximately $-5°C$ (268K). With a conservative maximum surface temperature of 200°C (473K)

imposed for safety, the maximum temperature ratio realized during testing was approximately 1.76.

Heated segment high temperatures were measured using K-Type thermocouples embedded within each copper segment. The thermocouples were mounted at a depth determined via one-dimensional conduction analysis to ensure temperature uniformity. From the known electrical power input and the measured surface-to-air temperature difference, the local convective heat transfer coefficient h is computed from:

$$\dot{q} = hA(\Delta T),$$

where $\dot{q}$ is the electrical heat input, A is the surface area of the copper segment, and ΔT is the temperature difference between the copper surface and the jet air.

This empirical approach is consistent with the methodology employed in foundational works such as Florschuetz et al.[24],allowing for direct benchmarking and validation.

4.3 Rig Configuration and Flow Conditioning System

Shop air, supplied at 10 Bar_g is reduced to lower pressure through a precision Fairchild precision regulator. The air is then cooled using four Vortex Tubes. Working air temperatures as low as $-5°$C (268 K) were achieved during the experimental campaign.

A schematic showing the main and crossflow paths is presented in Figure 4.4. Cooled air from three of the vortex tubes was used to charge the main jet plenum, and the final vortex tube was used to provide initial crossflow.

4.4 Jet Plenum Geometry

The jet plenum was designed to provide uniform flow distribution to a regular array of impingement holes on the jet plate. To allow uniform jet flow, a number of

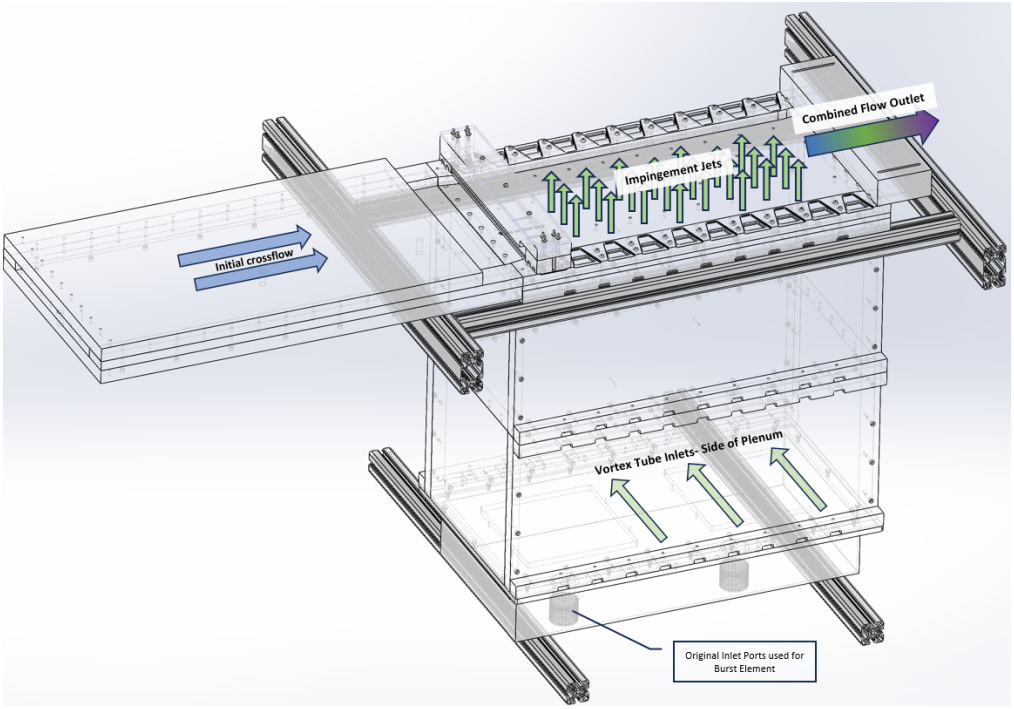

Figure 4.4: Schematic of the experimental rig showing the main working fluid cross and jet flows.

strategies were employed to minimise flow non-homogeneities in the plenum:

- the internal volume of the plenum was sized to maintain a flow area at least ten times greater than the total jet discharge area, consistent with best practices in jet impingement literature [24]
- the plenum walls were spaced at least one-half of the largest pitch dimension from the outermost jet holes, as recommended by Florschuetz et al. [24]
- Vortex tube outlet was directed into the jet plenum from the side walls, with inlet flow oriented orthogonally to the main jet flow direction
- a multi-layer stainless mesh was placed between two segments of the jet plenum construction to provide flow straightening and uniformity

No studies were conducted to establish the uniformity of the flow, or of the uniformity of jet discharge coefficient across the jet plate. However, the design of the plenum was based on best practices in the literature, and the flow straightening strategies employed were consistent with good engineering practice.

4.5 Jet Plate Geometry

The baseline experimental configuration featured a staggered jet array comprising ten streamwise and ten spanwise holes, arranged to provide uniform coverage of the heated copper plate. Jet diameter d was used as the reference dimension to non-dimensionalise the configuration for comparison with prior studies.

The primary geometric parameters defining the baseline configuration are shown in Table 4.1.

Table 4.1: Dimensionless geometric parameters of the jet plate

Parameter	Symbol	Value
Array Configuration	-	Staggered
Channel height	Z/d	3.5
Streamwise spacing	X/d	12.5
Spanwise spacing	Y/d	25
Jet plate thickness	T/d	2

This geometry, including pitch and layout, was defined in collaboration with MHI to ensure relevance to actual gas turbine internal cooling channel configurations. While the rig permits replacement of the jet plate to accommodate alternate geometries, the baseline configuration was retained for all tests reported in this thesis.

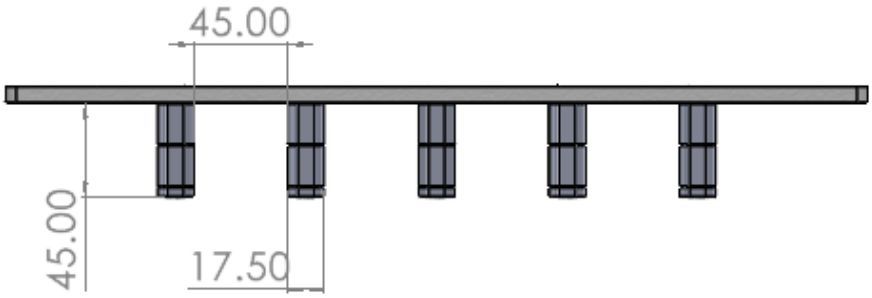

Figure 4.5: Illustration of castellated plate geometry. Row spacing and height of jet above the target plate was maintained for consistency.

4.5.1 Castellated Plate Design

The castellated plate that was tested maintained the datum staggered hole array: 5 spanwise rows of holes were used with 10 rows of streamwise holes. The jet hole

was maintained at 5mm diameter, and the height of the jet over the working section was maintained at 17.5mm. Figure 4.5 shows the size of the resultant corrugated flow channels. This geometry was driven by MHI internal research goals. In order to ensure manufacturability, the jet plate was built in smaller sections that could be assembled together in a variety of configurations, allowing a parametric study of corrugation geometries in later work. Only one geometry was studied for this project.

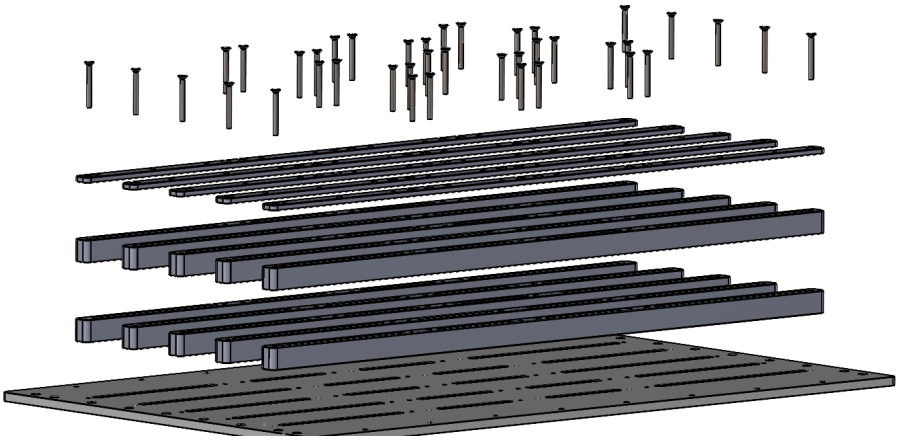

Figure 4.6: Illustration of modular design of castellated plate assembly.

Table 4.2 compares the present experimental rig with the maximum values or range of values for several canonical studies in terms of geometry, flow parameters, and temperature ratio. The rig developed for this project was deliberately scoped to provide a modular, flexible test platform that meets or exceeds the capabilities reported in prior work. It should be noted that the as-built X and Y spacing is well beyond the geometries studied previously. Suitability of the use of canonical results to qualify the current test stand is discussed later in this thesis.

Table 4.2: Comparison of Jet Array and Operating Parameters Across Studies

Parameter	**Present Work**	**Kerch. & Tab.[27]**	**Flors.[24][25][26]**	**Goodro**[38]
N_x (streamwise jets)	10	10	10	10
N_y (spanwise jets)	5	5	6	10
Z/d (channel height)	3.5	4.8	6.0	3
X/d (streamwise spacing)	12.5	12.5	15.0	8
Y/d (spanwise spacing)	25	12.5	8.0	8
$\mathrm{Re}_{\mathrm{jet}}$	3,000-20,000	300–30,000	5,000–50,000	17,000–18,000
$T_{\mathrm{wall}}/T_{\mathrm{jet}}$	1.06–1.76	1.05–1.28	1.10	1.06–1.73

4.6 Hot Section Design

The hot section of the rig was designed to produce well-characterized, steady-state heat flux conditions on the surface of the copper target plate. The target plate consists of ten equal-width copper segments, each approximately $6mm$ thick, aligned beneath the jet array and thermally isolated from one another.

Each copper segment is placed beneath a 900W mica patch heater (230 VAC). These heaters are individually controlled via solid-state relays (SSRs), allowing independent thermal regulation of each segment. Custom control boxes were designed and produced in the OTI for the purposes of this experiment. The boxes used Crydom solid state relays rated to 10 Amps per channel.

Segment temperatures are maintained at setpoints via PID control loops implemented in LabVIEW, which adjust heater power through analog output signals supplied by National Instruments (NI) C-Series hardware. This configuration ensures tight control of surface temperature, a prerequisite for accurate empirical determination of local heat transfer coefficients.

With the vortex tubes operating at the highest attainable pressure ratio, which theoretically provides the largest $DeltaT$, temperature ratios above 1.7 have been demonstrated. It should be noted that higher temperature ratios are possible, but the facility is limited by available electrical power. The custom heater control boxes components are rated to 10 Amps per segment, but the facility power supply is limited to 32 Amps per 10-channel box.

It should be noted, however, that the maximum commercially available heater power density will limit the practical power limit for the heaters to no more than approximately $10\frac{W}{cm^2}$, which is the state of the art capability for commercially available heating elements operating above 100°C. The internal resistance of polyimide and other film type heaters drops very quickly with temperature, creating a constraint on power dissipation at elevated temperatures.

Working air temperatures as low as -5°C (268 K) were achieved during the experimental campaign. The working surface could be actively heated to a maximum of 200 °C to ensure the rig remained within material limits. Direct measurement of the mass flow into the main plenum was not possible due to the operating characteristics of the vortex tubes, which exhaust a portion of the input

flow to atmosphere. Instead, mass flow rates were inferred from plenum pressure and temperature measurements using one-dimensional isentropic perfect gas flow relations. Although a Dwyer/Omega Series-300 differential pressure flow meter was installed in the crossflow channel, it was ultimately not used, as validation could not be completed within the project timeframe.

4.7 Instrumentation

A custom LabVIEW data acquisition and control software tool was written for this project. The system was designed to capture steady-state or near steady-state behaviour at stable thermal equilibrium. Thus, all data was captured at a rate of 1 Hz.

The data acquisition system consisted of the custom LabVIEW software, a National Instruments cDAQ-9188 Ethernet chassis, and a number of C-Series modules. The system was designed to be modular and expandable, allowing for future upgrades and additional sensors as needed. The system was also designed to be user-friendly, with a graphical interface that allowed for easy monitoring and control of the rig.

Thermocouples were used to measure the temperature of the copper segments and the working fluid temperatures. K-Type thermocouples were connected directly to a National Instrument C-Series module that had isothermal terminal block and on-board cold junction compensation. The thermocouple modules use a 24-bit ADC for highest possible temperature resolution.

A Scanivalve DSA-3217 system with 16-channel precision transducers was used to measure static pressure in the main plenum and crossflow duct. The Scanivalve system was connected to the LabVIEW software via an ethernet serial interface. A custom LabVIEW interface was written to allow capture of data from the Scanivalve.

Heater control was also implemented in the LabVIEW software, and details of this system are given in the sections below. A low-speed PID loop operating at 1Hz was implemented. Due to the large thermal mass of the system this control servo rate was found to be completely adequate for the experimental facility.

Segment heat flux required careful determination of the copper segment temperature for direct application of Newton's Law of Cooling. A 1-D thermal network

model analysis showed that even with non-uniformity of heater temperature and thermal contact with copper segments, that at 4 mm depth from the heater interface, the copper blocks temperature should be uniform. This is due to the high thermal conductivity of the copper, and is the reason that copper was selected for this application. Each copper segment was instrumented with 2 thermocouples, analogous to the setups by Kercher [27], Florschuetz [24] and others. Slots were cut into the bottom of the copper blocks to a depth of 4 mm and thermocouples were attached to the copper with thermal epoxy suited to the temperature. The temperature measurements from the thermocouples on each segment was used to calculate the segment heat transfer coefficient.

Additional thermocouples were placed to monitor:

- Main jet plenum air temperature
- Crossflow duct inlet air temperature
- Heater element surface temperature

All thermocouples were connected to an NI-9212 C-Series module, housed in an NI cDAQ-9188 Ethernet chassis.

4.7.1 Pressure Measurement

Static pressure measurements were acquired using a Scanivalve DSA-3217 system with 16-channel precision transducers. Measurements included:

- Main plenum pressure (averaged from four wall taps)
- Crossflow duct static pressure (two taps)
- Differential pressure across a Dwyer flow meter for estimating crossflow mass flow rate

4.7.2 Electrical Power Measurement

Voltage and current delivered to each heater were measured in real-time using Lovato D111 digital power meters with MODBUS RTU output. These were connected via a dedicated RS-485 bus and logged through the LabVIEW interface. These measurements were used to calculate the electrical power input to each heater segment, which was then used to determine the local heat transfer coefficient using the empirical methodology described in Chapter 2. It was assumed for the measurement that the total losses in the power conduction cables were low, and that all power was dissipated in the heaters rather than in the power lines.

4.7.3 SCADA and GUI

The LabVIEW interface provided a dedicated user interface which allowed for easy monitoring of the temperatures and adjustment of the low level operating parameters of the PID control system. Additional diagnostic information was given for all sensor interfaces, including the Scanivalve and power meters.

LabVIEW interface was developed for data acquisition, control, and logging. The software provided:

- Real-time display of temperature, pressure, and electrical signals
- PID control of each heater segment
- Automated logging of all sensor data for post-processing

4.7.4 Heater Control Interface

Custom control boxes were designed to interface with the mica heaters. Each box contained a solid-state relay (SSR) for each heater, allowing for independent control of power input. The SSRs were controlled via analog output signals from the National Instruments 9188 chassis, enabling precise regulation of heater power. The control boxes were designed to accommodate up to 10 segments, with a maximum current rating of 10A per segment. This configuration allowed for flexibility in heater selection and power distribution, ensuring that the rig could be operated safely and efficiently. All solid state relays were mounted to a large aluminium plate

to serve as a heat sink, and the boxes were built into Schroff 2-U vented transfer racks for ventilation and mounting into standard 19" racks.

Each copper segment was instrumented with 2 thermocouples. The temperature of the copper segments was calculated by averaging the two thermocouple readings. The calculated segment temperature was used as the input to the PID algorithm, and each segment/heater was controlled independently. Provision was made to allow a unique PID parameter set for each heater, but this was not needed in practice.

Due to the fragility of the thermocouples, 'broken thermocouple' detection was employed in the Labview software. If a segment experienced a thermocouple failure, the control parameter would be derived from the remaining functional thermocouple. In the event of a failure of both thermocouples, the heater would be disabled and an alarm would be raised. This was a useful feature, as it allowed for continued operation of the rig in the event of a single thermocouple failure.

4.8 Sources of Experimental Uncertainty

A detailed uncertainty analysis was conducted to quantify the uncertainties associated with the heat transfer coefficient calculations. This analysis is critical for ensuring the reliability and accuracy of the experimental results, particularly considering that the empirical method employed requires a full accounting for heat losses between the heaters and working section.

The uncertainty analysis presented here follows the framework of ANSI/ASME PTC 19.1-1985 and the methodological guidance described by Wells [47]. This approach enables the estimation of the interval within which the true value of a measured or derived quantity is expected to lie, typically with 95% confidence.

4.8.1 Recommended Procedure

The recommended procedure involves the following key steps:

1. **Definition of the True Value**: Clearly define the physical quantity of interest, including how it is measured or derived. This anchors the analysis to a specific intended result and prevents misinterpretation.

2. **Identification of Input Quantities**: List all measured or controlled variables used to compute the final result. These may include temperature, heat flux, thermal conductivity, or geometric dimensions.

3. **Error Classification**: Each uncertainty source is classified as either:

   - *Type A (Random)*: Evaluated statistically, typically via standard deviation of repeated measurements.
   - *Type B (Systematic)*: Estimated based on calibration reports, manufacturer specifications, or engineering judgment.

4. **Standard Uncertainty Estimation**: For each variable x_i, the standard uncertainty u_{x_i} is estimated. For Type A uncertainties, this is usually the sample standard deviation. For Type B, a uniform, triangular, or normal distribution assumption is applied to infer the standard uncertainty.

5. **Propagation of Uncertainty**: The uncertainty in a derived quantity $y = f(x_1, x_2, \ldots, x_n)$ is obtained via the general law of propagation of uncertainty:

$$u_y = \sqrt{\sum_{i=1}^{n} \left(\frac{\partial f}{\partial x_i} u_{x_i} \right)^2}$$

   This requires the functional relationship between y and each x_i, and reflects the sensitivity of y to each variable.

6. **Calculation of Relative Uncertainty**: To compare the magnitude of uncertainty across different quantities or methods, the *relative uncertainty* is computed:

$$\text{Relative Uncertainty} = \frac{u_x}{x}$$

   This dimensionless quantity is often expressed as a percentage and is particularly useful for assessing which input variables dominate the total uncertainty.

7. **Combination of Random and Systematic Components**: Final uncertainty in the result is calculated using the root-sum-square method:

$$U = \sqrt{U_{\text{rand}}^2 + U_{\text{sys}}^2}$$

where U is the expanded uncertainty associated with a 95% confidence level (typically using a coverage factor $k = 2$ for large samples).

8. **Result Reporting**: The result is reported in the form:

$$y = \bar{y} \pm U \quad [\text{units}]$$

along with a statement of confidence level and any relevant caveats regarding systematic errors or modelling assumptions.

The uncertainty analysis for this work took into the following factors:

- **Thermocouple Mounting Method**
- **Use of Thermocouple Connection Plugs**
- **Use of Thermocouple Extension-Grade Wire**
- **ADC Least Significant Bit Conversion Error**
- **IR Camera Measurement Error**
- **Heater Power Measurement Accuracy**
- **Insulation Material homogeneities**
- **Insulation Material Thickness**
- **Insulation Material Thermal Conductivity**

The summary shown in Figure 4.7 represents an initial, geometry-based uncertainty analysis performed early in the design process. This first-cut assessment revealed that geometrical tolerances and insulation uniformity would have a dominant influence on the reliability of calculated heat transfer coefficients, particularly in the absence of a calibrated thermal loss model. As a result, design attention was focused on controlling these factors during rig construction. While the configuration of the experimental rig evolved during the project, this preliminary analysis remains instructive in illustrating the relative magnitudes and sources of uncertainty inherent in the system. A more refined evaluation, based on a thermal network model and updated geometry, was used to quantify final uncertainty values, as presented in Chapter 5.

Propagation of uncertainties through HTC Calc

Convection (Surface Thermocouples)

	Uncertainty	Expected Value		Relative Unc.	
Temperature Uncertainty†	3.15E+00	473	**[K]**	6.67E-03	[-]
Flux Uncertainty	3.47E+00	3000	**[w/m2]**	1.16E-03	[-]
Total Uncertainty HTC:		~350	±	2.36914	**[W/m^2K]**

Convection (IR Camera)

	Uncertainty	Expected Value		Relative Unc.	
Temperature Uncertainty	1.87E+00	473	**[K]**	3.95E-03	[-]
Flux Uncertainty	3.47E+00	3000	**[w/m2]**	1.16E-03	[-]
Total Uncertainty HTC:		~350	±	1.44200	**[W/m^2K]**

Convection Photochromic Liquid Crystal

	Uncertainty	Expected Value		Relative Unc.	
Temperature Uncertainty	1.15E-01	473	**[K]**	2.44E-04	[-]
Flux Uncertainty	3.47E+00	3000	**[w/m2]**	1.16E-03	[-]
Total Uncertainty HTC:		~350	±	0.41319	**[W/m^2K]**

Conduction*

	Uncertainty	Expected Value		Relative Unc.	
Rohacell Material Uncertainty	5.20E-03	0.03	**[W/mK]**	1.73E-01	
Rohacell Measurement Uncertainty	1.15E-06	0.0005	**[m]**	2.31E-03	
Flux Uncertainty	3.47E+00	3000	**[w/m2]**	1.16E-03	
Total Uncertainty HTC:		~350	±	60.62851	**[W/m^2K]**

***Note: This calculation assumes flux measured across a single layer of the target plate assembly.**

Figure 4.7: Preliminary estimate of uncertainties in heat transfer coefficient calculations, used during early rig design to inform construction and instrumentation priorities.

4.9 Rig Performance Targets

The rig was originally designed to achieve the following design envelope:

- **Temperature Ratio:** 2.0
- **Jet Reynolds Number:** 0-20,000
- **Crossflow / Main Mass Flow Ratio:** 0.3

4.10 Rig Actual Performance

In practice, the performance of the rig deviated significantly from the idealised design targets.

- **Temperature Ratio:** ≈ 1.7 (Only at low Jet Reynolds numbers)
- **Jet Reynolds Number:** 0-20,000
- **Crossflow / Main Mass Flow Ratio:** Not directly measured

The maximum temperature ratio achievable was constrained by both the electrical power available at the facility and the performance limitations of the vortex tube cooling approach. Specifically, the use of 8 barg compressed air,combined with the inherent mass loss due to the hot-side exhaust of the vortex tubes, limited the net cooling capacity deliverable to the plenums. Although a 28 barg line was available, its use would have required significant modifications to the test stand infrastructure and formal recertification of the facility under the UK Pressure Systems Safety Regulations (PSSR), which was not feasible within the scope of this work.

Similarly, the availability of 32 A electrical outlets in proximity to the test area constrained the maximum heater power that could be delivered to the copper target plates. While additional power drops could theoretically have been installed, the cost and complexity of doing so were prohibitive in the context of this experimental campaign. The power distribution/control/monitoring boxes for the heater section were capable of up to 10 Amps per segment, which was 2x the rated power of the heaters.

4.11 Recommendations for Rig Improvements

The originally conceived rig represented a significant step forward in the design of experimental facilities for jet impingement cooling studies. However, due to budgetary restrictions, a number of compromises were made during the design and construction phases that limited the performance of the rig. The following recommended improvements or modifications to the rig are recommended if the work is to be continued. These recommendations are drawn from lessons learned in the design, procurement, manufacturing and operation of the experimental facility.

4.11.1 Heater Selection and Installation

Due to temperature and energy density requirements for temperature ratio targets, selection of commercially available heaters was restricted to using mica or cartridge heaters. Cartridge heaters were rejected due to high cost and exceptionally precise mounting requirements. The construction of the selected mica heaters was such that temperature uniformity could not be achieved across the heaters. This meant uneven heating of the copper segments, which was exacerbated by the fact that the mica heaters were not in direct contact with the copper segments. Goodro et al. [38] and others used extremely thin polyimide single zone heaters bonded to the aerodynamic working surface [24] to achieve good temperature uniformity, but our temperature ratio and energy density targets did not allow the use of polyimide or polyimide foil heaters in this experiment. Polyimide heater max allowable power density drops off dramatically at temperatures above $75°C$. In addition to difficulties with the heater uniformity, the copper blocks themselves were not uniform geometrically, and this gave further rise to uncertainty in the determination of Nusselt number and heat transfer coefficients. Finally, inclusion of interstitial insulators between the heaters proved to be difficult to achieve due to uniformity of the aerodynamic surface, and there was therefore no insulation between the heater and the copper segments. This meant that the heat transfer coefficient was not uniform across the copper segments. The mica heaters also demonstrated different electrical characteristics between the different segments. All of these factors would certainly have caused a source of uncertainty in the determination of Nusselt number and heat transfer coefficients.

It is recommended to use suitably sized cartridge heaters embedded into precision manufactured copper segments to allow high temperature operation.

4.11.2 Process Air Cooling

The use of the vortex tubes for process air cooling also required a number of compromises. The original design concept was to use a cascade refrigeration air handling unit to bring the main jet and crossflow working fluid to a target of $-40°C$. This would have allowed a wall/jet temperature ratio of 2.0 while keeping the rig temperature within safety and material limits. Use of the refrigerated air handling unit was not possible due to budgetary constraints. Surplus vortex tubes,

purchased for another experiment, were repurposed for this application and used to cool our working air. However, the use of vortex tubes limited the achievable temperature ratio to a maximum of 1.7, and mass flow limitations on building air supply limited us to a reduced range of jet Reynolds numbers at this highest temperature ratios. And, since the vortex tubes bleed a certain amount of air to atmosphere, it was not possible to do mass flow measurements in the main jet plenum due to budgetary constraints.

It is recommended to allow for use of cascade refrigeration air handling loop for working air cooling to allow driving the jet and crossflow to lower temperatures. Management of these flows through dedicated piping without losses would also allow determination of mass flow rates in the main jet plenum. This would allow for better control of the mass flow rates and determination jet Reynolds numbers.

4.11.3 High Temperature Structural Materials

During the experimental campaign, it was observed that the commercially available high-temperature structural materials selected for certain components of the apparatus degraded severely after thermal cycling. Although material ratings were not exceeded, these materials became exceptionally fragile and brittle following repeated thermal exposure. Commercially available insulation, designed for use in domestic fireplaces, was employed to insulate the hot section of the rig. While rated for the intended temperatures, this insulation was only available in block form and required manual cutting to fit the rig geometry. As a result, the insulation was non-uniform, and improved thermal performance could likely have been achieved using custom-manufactured, monolithic structural insulation elements.

It is recommended to create custom monolithic structural insulation elements to allow for better thermal insulation of the hot section of the rig.

4.11.4 Thermocouple Attachment

In practice, the most technically challenging aspect of the rig manufacture was the attachment of the thermocouples to the copper blocks. This problem led to the greatest number of failures and repairs needed in the hot section of the experimental facility. Materials used to embed the thermocouples in the copper

blocks were brittle and extremely fragile. This provided challenges for assembly and handling, and routing of leads through the heaters and copper segments was difficult. The thermocouples were also not able to be removed from the copper segments without damaging the copper segments once the attachment materials dried or cured. This meant that the thermocouples could not be replaced without significant rework, involving cleaning and reattachment of the thermocouples. Thermal expansion of elements in the working section created mechanical pinch points which damaged delicate fine-gauge thermocouple wires, and local temperature hot spots clearly exceeded the temperature ratings of thermocouple wire insulation in the finest gauge thermocouples.

It is recommended to use a more robust method of attaching the thermocouples to the copper segments. This could be achieved by using a more robust attachment method, such as soldering or welding, or by using a different type of thermocouple that is less sensitive to mechanical damage. It is also recommended to use a larger gauge thermocouple wire to reduce the risk of mechanical damage.

A great deal of work and iterative improvement was done on the experimental rig over the course of the commissioning exercise, and remedial improvements to the design, equipment and methodology were made when problems were discovered.Ultimately, the experimental rig proved well conditioned enough to give good data and agreement with the canonical literature. However, the highest design temperature ratios were ultimately unachievable.

4.12 Unrealized Design Features

The following activities were not completed during this project, but are recommended for future investigation:

Infrared Imaging for Surface Temperature Mapping

An alternative design concept was developed to enable infrared (IR) imaging of the target plate through optical windows integrated into the jet plate. This would have permitted two-dimensional surface temperature measurements under jet impingement. The approach relied on a lower-conductivity overlay material

bonded to the copper substrate, providing strong through-thickness conduction while suppressing lateral conduction; effectively creating a thermally anisotropic layer. Under constant power operation (as opposed to isothermal control), impinging jets would induce localised cooling and generate measurable surface temperature gradients. These gradients could then be captured via IR imaging to infer local heat transfer coefficients.

This methodology is consistent with the work of Goodro et al. [38], who employed a very thin (0.5 mm) polystyrene plate on the back of a polyimide film heater operating in constant power mode. Their system operated at sufficiently low power that temperature variations on the front surface were spatially resolvable through the back of the thin heater layer. However, in the present work, the higher jet Reynolds number and temperature ratio targets precluded the use of polyimide heaters, which suffer from strong power roll-off at elevated temperatures.

Although a new heater working section was proposed to support this configuration, the required IR windows were not procured due to budgetary constraints, and the design was not finalised within the project timeframe. It is recommended that future work incorporate IR imaging capability, as this would enable spatially resolved surface temperature measurements and support a more detailed characterisation of impingement cooling behaviour.

Flow Visualisation and Particle Image Velocimetry (PIV)

The rig was also designed to accommodate flow visualisation using a laser sheet and high-speed imaging. This configuration would have supported the use of particle image velocimetry (PIV) to capture time-resolved velocity fields within the jet impingement array. However, a suitable laser enclosure was not available, and there was insufficient time to conduct PIV measurements within the project timeframe. Future implementation of PIV is recommended, as it would provide valuable insights into the unsteady flow structures and jet - crossflow interactions that govern local heat transfer.

Measurement of Jet Discharge Coefficient Uniformity

A detailed study of jet discharge coefficient uniformity across the target plate is also recommended. No measurements were conducted during this project to assess whether discharge coefficients were spatially uniform across the array. This is a significant limitation of the present work. Due to flow acceleration in the channel, particularly in downstream locations, it is anticipated that local discharge coefficients may vary, resulting in elevated jet Reynolds numbers further downstream.

CFD simulations conducted for the flat plate geometry suggest that this effect becomes increasingly pronounced at higher total mass flow rates. While it is not yet clear whether the variation is large enough to exceed experimental uncertainty, the underlying trend could influence the interpretation of spatial heat transfer data. Future work should therefore include experimental or computational studies to assess plenum flow uniformity and jet discharge coefficient variation across the array.

5

Experimental Results and Analysis

With the facility and instrumentation platform now designed and manufactured, this chapter presents the experimental results obtained for both flat and corrugated jet plate configurations. These results provide direct insight into the influence of jet Reynolds number and temperature ratio on local heat transfer, and lay the groundwork for subsequent numerical evaluation of a conduction-enhanced cooling concept.

As previously stated, the primary objective of this work is to assess whether the use of a corrugated jet plate can reduce the deleterious effects of accumulating crossflow in an impingement cooling channel. Crossflow interference remains a serious challenge in gas turbine cooling applications, and effective mitigation strategies have the potential to significantly improve overall cycle efficiency. If internal cooling performance could be enhanced to the point where film cooling were no longer necessary, the implications for gas turbine blade design and manufacture would be substantial.

While it is not known whether Mitsubishi Heavy Industries (MHI), the industrial sponsor of this work, intends to eliminate film cooling entirely, they are actively investigating corrugated internal cooling geometries as a means to mitigate crossflow-induced degradation of impingement jets. The current state of the art of additive manufacturing suggests that it should be possible to manufacture blade inserts with corrugated walls for use inside gas turbine blades. Recent work by Hatta [2, 3] confirms that this concept is is under active investigation by MHI.

Experiments were conducted across a range of initial crossflow conditions; however, due to time constraints, it was not possible to perform a rigorous characterization of the Dwyer in-line differential mass flow device in-situ. As a result, no quantitative values are provided for the ratio of main flow to crossflow mass flow rates. Instead, the presence of crossflow is treated as a binary condition; either present or absent.

Following successful commissioning of the experimental rig, the limited time available for testing precluded a full parametric study. Notably, no experimental results for the flat plate with initial crossflow are presented in this thesis. Although these tests were performed, the inability to determine the corresponding main-to-crossflow mass flow ratios precluded any meaningful interpretation, and the data have therefore been omitted.

Nevertheless, at high jet Reynolds numbers, the flow was sufficient to generate substantial crossflow through entrainment alone, without the need for externally introduced secondary flow. The relationship between crossflow and Nusselt number reduction for both flat and corrugated jet plates is examined later in this chapter.

5.1 Rig Commissioning and Validation Against Canonical Literature

Comparison to canonical literature, particularly the work of Kercher et al. [27], was adopted as a reference point for evaluating the performance of the test facility. Although the specific jet array geometry used in this study—provided by Mitsubishi Heavy Industries (MHI)—featured significantly larger spanwise spacing (Y/d) than typically reported in the literature, initial validation against established power-law trends offered a practical means of assessing whether the rig was operating in a well-conditioned regime. While early commissioning efforts paid particular attention to matching the slope of the Kercher correlation, it must be acknowledged that the geometries studied by Kercher and Florschuetz were considerably more compact. In the present configuration, where the channel height is not aggressively constrained and the flow remains well within the jet-dominated regime, broadly similar power-law behaviour is expected. The wider spacing may reduce jet-to-jet interference and modify downstream flow development, but the comparison remains scientifically valid and useful for interpreting cooling trends.

Despite this, the experimental data produced in this work exhibit a slope of $m = 0.859$, which fall squarely between the canonical values reported by Kercher ($m = 0.957$) [27]and Florschuetz ($m = 0.812$) [25]. This result is interpreted as strong evidence that the essential heat transfer physics are preserved, and

that the experimental rig is capable of producing meaningful and trustworthy data in extended flow configurations. Values of the fitted slope, along with fits derived from the Florschuetz et al. and Kercher et al. correlations for equivalent geometries, are shown in Figure 5.1.

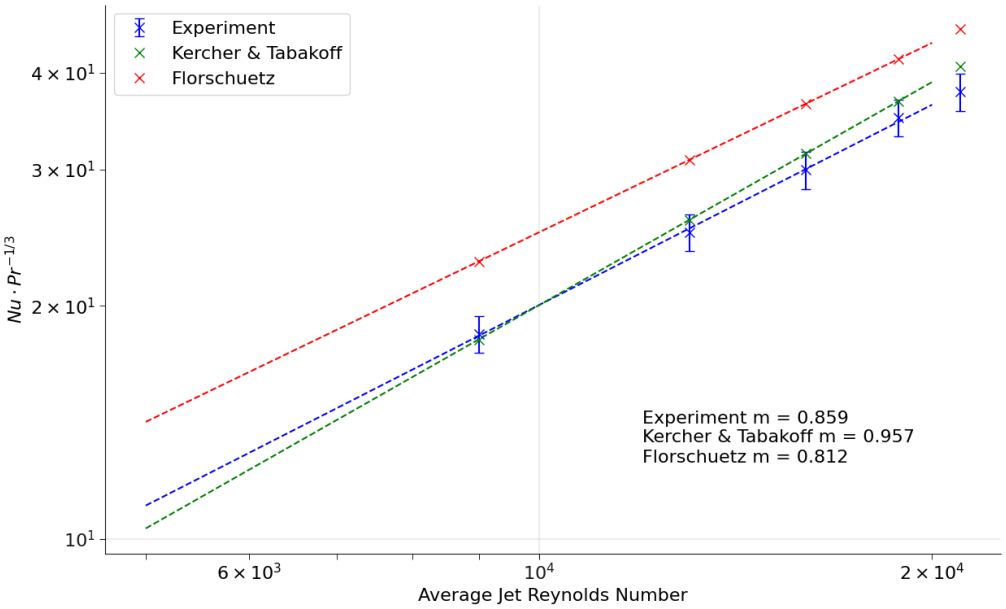

Figure 5.1: Comparison of experimental results with canonical correlations for $Nu \cdot Pr^{-1/3}$ as a function of jet Reynolds number. Data were obtained using a $d = 5\,\text{mm}$ jet and extended geometric ratios ($X/d = 12.5$, $Y/d = 25$). The observed slope of the experimental trend closely matches those of Florschuetz and Kercher & Tabakoff, supporting consistency with established literature. Error bars indicate systematic uncertainty only.

While it is reasonable to use classical correlations as a benchmark for general comparison, it is not necessarily wise to demand precise equivalence when the underlying data were developed for geometries and flow regimes substantially different from those under investigation. The Florschuetz and Kercher correlations were derived empirically for compact jet arrays with limited channel height and spacing ratios, whereas the present configuration was intentionally extended to study performance in tall, high-aspect-ratio channels with jet diameters and related geometries designed allow for high resolution 2D temperature imaging with thermography. The fact that the experimental slope falls between the canonical values is not a deviation, but rather a confirmation that the rig successfully captures the dominant physics across a broader range.

The error bars shown in Figures 5.1 represent only the propagated uncertainty due to systematic measurement errors, including power input, surface temperature, area, diameter, and air conductivity, as outlined in the analysis below. While a thermal resistance model was applied during post-processing to estimate the surface heat flux at each operating point, the fidelity of that model may not fully capture the poor thermal contact between the non-uniform heaters and non-uniform copper segments. Accordingly, the error bars presented here reflect only the known measurement uncertainty, which is justified for comparative and trend analysis, with a more detailed discussion of heat loss and magnitude discrepancies provided in the next section.

5.2 Uncertainty Analysis Methodology

A detailed analysis of systematic and random error sources was conducted based on the NREL / ANSI PTC 19.1 methodology [47]. This approach recommends quantifying sources of error such as thermocouple attachment, thermocouple electrical connection type, and analog-to-digital conversion accuracy.

The experimental Nusselt number Nu is computed as:

$$Nu = \frac{hD}{k} \tag{5.1}$$

where the convective heat transfer coefficient h is given by:

$$h = \frac{q''}{\Delta T} \tag{5.2}$$

5.2.1 Heat Flux Determination

The surface heat flux q'' is calculated from the measured electrical power input Q_{total}, corrected by a 'loss' factor η, which quantifies the fraction of total heater energy that is lost from the rig and cannot be included in flux calculations at the working surface. This factor is obtained from a thermal network model developed by the group's Post Doctoral Research Fellow.

$$q'' = \frac{\eta \cdot Q_{\text{total}}}{A} \tag{5.3}$$

where:

- $\eta = 1 - Q_{\text{loss}}/Q_{\text{total}}$ is the known fraction of power reaching the working section,
- A is the heated surface area (m^2),
- Q_{total} is the total electrical power input (W).

Since η is not uncertain, the relative uncertainty in q'' is:

$$\left(\frac{\Delta q''}{q''}\right)^2 = \left(\frac{\Delta Q_{\text{total}}}{Q_{\text{total}}}\right)^2 + \left(\frac{\Delta A}{A}\right)^2 \tag{5.4}$$

5.2.2 Uncertainty in Heat Transfer Coefficient h

Using Equation (5.2), the propagated uncertainty in h is:

$$\left(\frac{\Delta h}{h}\right)^2 = \left(\frac{\Delta q''}{q''}\right)^2 + \left(\frac{\Delta(\Delta T)}{\Delta T}\right)^2 \tag{5.5}$$

5.2.3 Uncertainty in Nusselt Number Nu

Finally, propagating h, D, and k into Nu:

$$\left(\frac{\Delta Nu}{Nu}\right)^2 = \left(\frac{\Delta h}{h}\right)^2 + \left(\frac{\Delta D}{D}\right)^2 + \left(\frac{\Delta k}{k}\right)^2 \tag{5.6}$$

5.2.4 Sources of Measurement Uncertainty

Assumptions:

- For temperature-based uncertainty calculations, the lowest expected operating temperature was used to give the largest (i.e., most conservative) error bounds.

Table 5.1: Summary of measurement uncertainties used in uncertainty propagation calculations.

Quantity	**Uncert. (Δ)**	**Nominal**	**Frac.** (Δ/Nominal)	(%)
Temperature	3.15	295	0.0107	1.07%
Power	3.46	100	0.0346	3.46%
Area	2.8E-4	0.00195	3.3E-3	0.33%
Jet Diameter	2.0E-4	5e-3	0.04	4.0%
Air Conductivity	-	$\kappa(370.5K)$	0.0095	0.95%

- Power measurement nominal was given to be on the low end of rig operating points to give the largest (i.e., most conservative) error bounds.
- All rig components were manufactured to a nominal precision of ±0.1 mm. However, for the purposes of worst-case analysis, a more conservative uncertainty of ±0.2 mm was applied to linear dimensions used in the area and diameter calculations.
- The thermal conductivity of air was evaluated at the film temperature, which was taken as the average of the surface and coolant temperatures. A temperature uncertainty of ±3 K was assumed, and its impact on air conductivity was estimated using tabulated property data as shown in standard property data [48]. The resulting uncertainty in k was approximately ±0.95%, and this was included in the propagation of uncertainty into the Nusselt number. The temperature dependence of air conductivity is approximately linear in the operating regime of this experiment.

5.2.5 Final Propagated Measurement Uncertainties

Based on the uncertainty propagation methodology described above, the relative uncertainties in the heat transfer coefficient and Nusselt number were calculated as:

$$\frac{\Delta h}{h} = 0.0364 \quad \Rightarrow \quad \Delta h = 3.64\% \cdot h$$

$$\frac{\Delta Nu}{Nu} = 0.0549 \quad \Rightarrow \quad \Delta Nu = 5.49\% \cdot Nu$$

These values account for measurement uncertainties in power input, surface temperature, heated area, jet diameter, and air thermal conductivity, as outlined in Table 5.1.

5.3 Experimental Campaign

After rig commissioning, approximately 80 experimental runs were conducted over a 3 month period. Tests were punctuated by rig repairs and reconfigurations. Runs spanned a range of Reynolds numbers from approximately 1,000 to 20,000, and temperature ratios T_s/T_∞ ranging from 1.0. to 1.7. Tests were performed on two geometrically distinct jet plates: a flat (smooth) datum geometry and a corrugated plate designed to give more channel cross sectional area for spent cooling air to exit without interfering with downstream impingement jets.

The goal of this experimental campaign was not to explore the full parameter space, but to generate a robust, physically plausible dataset that could prove whether the use of corrugated plates would be effective in reducing the effects of crossflow on impingement jets in gas turbine internal cooling channels.

5.4 Experimental Procedure

The experiment, and data post processing, was considered at steady-state thermal equilibrium only. No transient behaviour of the rig was logged or investigated. At the beginning of the test, the rig was set to desired flow conditions by adjusting the plenum pressure using the Fairchild pressure regulator, which fed the vortex tube distribution plenum. Flow was established first to reduce the possibility of operating the heaters without any cooling.

Once the target pressure in the plenum was reached, the data acquisition and control system was switched on, which gave initial low power to the heaters. The energy meters required some current to be flowing through the heaters in order to function. At power-on, each heater was operated at circa 15 Watts. This proved to provide only very minimal heating, and allowed for tracking of the heater power through the entire test.

In order to start a test run, the rig had to be set up to operate at the target temperature ratio, which was defined as T_s/T_∞. Jet Reynolds number was selected for each run by setting the Fairchild regulator to charge the main jet plenum with a target static pressure which corresponded to our target Jet Reynolds number for the run. This meant that the vortex tubes operated at a different ΔT for each run. And, because the vortex tube produced different output pressures for each target jet reynolds number, the target surface temperature setpoint had to be calculated for each run. Once the target temperature was input into the system, the PID control loop was activated in the LabVIEW software, and the rig was allowed to get to steady state equilibrium. The system proved to be exceptionally stable in active control. When all heaters were functioning correctly, segments could be controlled reliably to within one degree of each other during soak segments.

Once thermal equilibrium was achieved at each flow/temperature setpoint, the LabVIEW SCADA system was used to record heater voltage, heater current, plenum pressure, as well as segment, plenum and ambient temperatures. These values were logged at a rate of 1Hz to a TDMS file for later postprocessing. Those results are presented later in this Chapter.

5.5 Data Reduction Methodology

The data analytical method for the empirical determination of HTC in this experimental apparatus was detailed in Chapter 2. The first step of the process involved calculation of the segment HTC directly from Newton's Law of Cooling using the segment electrical power and temperature. From the HTC, the segment Nusselt number could be calculated. The jet diameter d was used for the calculation of Nusselt number, per historical convention, and the fluid properties were calculated at the average of the plenum and segment temperatures.

The post-processing routine used to extract heat transfer coefficients and Nusselt numbers in this study was originally developed by the group Post Doctoral Research Fellow. It was adapted for the present work with minor modifications. The routine includes a thermal network model to estimate the heat losses from the rig using a thermal resistance framework. In addition, radiative heat loss to the cold jet plate is estimated using a simplified parallel-plate formulation. The Nusselt number

values reported in this thesis include these heat loss corrections for Nusselt number calculation. It should be noted that the analysis is approximate, as the surface emissivities of the copper and acrylic jet plates were not measured directly. A detailed radiation analysis of the corrugated jet plate was not attempted due to geometric complexity. If this work is extended beyond the Master's level, a more rigorous treatment of radiative loss, including geometry-specific modelling and surface property characterization, will be required.

5.5.1 Calculation of Jet Reynolds Number

The rig, as built, did not have a mass flow measurement capability on the main jet plenum flow. As such, the jet Reynolds number had to be calculated using the plenum pressure, plenum temperature and the discharge coefficient of the jet orifice. Jet orifice discharge coefficient was calculated with the empirical relationships generated by McGreehan, et. al. [49] per Gillespie[28]. Jet Reynolds number was calculated using the jet velocity from the Florschuetz methodology as function of the $\frac{G_c}{G_j}$ parameter. This is based on their following expression, which assumes one-dimensional isentropic perfect gas flow through the jet orifice [26]

$$G_j = C_D P_0 \left(\frac{P}{P_0}\right)^{1/\gamma} \left[\frac{2\gamma}{\gamma - 1} \cdot \frac{1}{RT_0} \left(1 - \left(\frac{P}{P_0}\right)^{\frac{\gamma-1}{\gamma}}\right)\right]^{1/2} \tag{5.7}$$

where G_j is the jet mass flow rate, C_D is the jet orifice discharge coefficient, P_0 is the plenum (total) pressure, P is the ambient (or channel) pressure, and γ is the ratio of specific heats. It should be noted that variation of C_D in the channel is expected because of the accelerating flow as crossflow accumulates in the channel. This will affect the discharge coefficient and the jet velocity as a function of the axial position in the channel. And while this was not measured directly, it is expected that the effect of the channel crossflow on the jet velocity will be small, and that the average value of C_D will be a good approximation for the entire channel. This is supported by the work of Florshuetz, et. al. [24] who measured the uniformity of the jet velocity and found it to be largely unaffected except at small channel heights.

5.6 Selection of Reference Temperature

In gas turbine cooling applications, and in the present experimental configuration, spent jet cooling fluid (air) is typically confined within a narrow flow channel downstream of the impingement region. As a result, the local fluid temperature, and hence the convective driving temperature difference ΔT in Newton's Law of Cooling, is not constant but varies spatially along the channel. This spatial variation raises a fundamental concern regarding the commonly used assumption of a uniform reference temperature for convective heat transfer analysis.

Newton's Law of Cooling, stated in its classical form, relates the local surface heat flux q'' to the temperature difference between the wall and the fluid:

$$q'' = h\,(T_s - T_\infty) \tag{5.8}$$

where h is the local convective heat transfer coefficient, T_s is the local surface temperature, and T_∞ is the reference fluid temperature. The physical interpretation of T_∞ is straightforward in simple, spatially uniform flows, but becomes non-trivial in spatially developing or confined impingement flows, where the fluid temperature varies significantly along the wall.

The most rigorous reference temperature in such flows is arguably the adiabatic wall temperature, which accounts for the local stagnation of the flow and the associated conversion of kinetic energy into internal energy. This definition captures the thermal effects of both full and partial stagnation and is commonly used in high-speed convective heat transfer. However, even this approach is fundamentally limited in wall-bounded jet flows: it does not account for the downstream evolution of fluid temperature caused by accumulated heat transfer from upstream wall sections. As such, even the adiabatic wall temperature does not fully resolve the ambiguity in defining ΔT in Equation (5.8).

In the present study, adiabatic (unheated) test runs were conducted to evaluate whether flow stagnation affected the surface temperature on the instrumented surface. This was a time consuming validation step because the working fluid was cooled, the entire section had to be allowed to get to thermal equilibrium before a meaningful determination could be made. However, within the resolution limits of the thermocouple instrumentation, no measurable difference was observed

between the wall temperature at the stagnation region and the upstream plenum air temperature during these tests. This experimental observation supports the use of the plenum temperature as a practical and justifiable approximation for T_∞ in Equation (5.8). The approach taken here aligns with Florschuetz and other foundational studies, reinforcing the appropriateness of using plenum temperature as T_∞ in jet impingement heat transfer experiments.

Nevertheless, the analysis presented here underscores a deeper conceptual limitation in Newton's Law of Cooling when applied to confined or spatially evolving convective flows. Newton's original formulation describes the cooling of a body in terms of the excess heat relative to the ambient atmosphere, effectively treating the surrounding air as an infinite thermal reservoir at constant temperature. His experimentation on idealized forced convection scenarios used the same assumption, as the ambient environment served, for all practical purposes, as an infinite thermal sink [50].

However, in complex configurations such as impingement cooling, this simplification becomes problematic. The fluid temperature varies spatially due to the confinement of spent air in narrow channels and the cumulative effects of upstream heat transfer. As a result, the driving temperature difference ΔT is itself a function of position within the fluid domain, and the choice of reference temperature becomes non-trivial. In such cases, any quantification of heat transfer effectiveness must rely on a limiting assumption. To enable consistent comparison across studies, the community must adopt and adhere to clearly defined conventions.

In the present work, the plenum temperature was used as the reference temperature. This choice is consistent with established literature and reflects common practice in experimental jet impingement studies. Nevertheless, consideration of the selection of a reference temperature for Newton's Law of Cooling highlights an underlying conceptual limitation of Newton's Law when applied to non-ideal, thermally evolving convective environments. While a comprehensive treatment of this issue lies beyond the scope of the current study, and no claim is made here to amend Newton's foundational insight, it is noted as an intellectual point of interest and a potential subject for future theoretical and experimental refinement.

5.7 Presentation of Results

As the focus of this study was to establish whether the use of corrugated plates would be effective in reducing the effects of crossflow on impingement jets in gas turbine internal cooling channels, the results are presented in a manner that emphasizes the comparison between smooth and corrugated plates. The results are presented in two sections: first, the local Nusselt number distribution along the centreline of the channel is presented, followed by a discussion of the global Nusselt number as a function of Reynolds number. It was not possible within the scope of this apparatus to capture the full two-dimensional structure of the HTC distribution on the target surface, and therefore no direct qualification of jet deflection was attempted. This limitation was understood at the outset and is consistent with the intended scope of the study, which was not designed as a full parametric investigation of the effects of corrugated geometries on jet flow structure. However, this effect has been captured in high fidelity in a detailed CFD study performed by a PhD student in our group. Those results are not presented in this thesis.

Flat plate experiments did not include initial crossflow runs. However, since initial crossflow only translates to *additional* channel flow, we'd expect the results to broadly follow the trends demonstrated by Florshuetz et al. in the 1982 work [26]. However, the corrugated plate experiments were conducted with and without initial crossflow, as mitigation of 'high' levels of crossflow was the goal of the corrugated plate design. The results of the corrugated plate experiments are presented in Section 5.7.2.

Figure conventions. In all panels, line colour encodes jet Reynolds number (low→high: Blue, Orange, Green, Red, Purple). Not every Reynolds level was run in every case; when a level is absent, the remaining series retain the same low→high colour order.

5.7.1 Flat Plate Results

The results of the flat plate experiments are presented in Figure 5.2. The data show a consistent trend across all temperature ratios, with the Nusselt number increasing with Reynolds number. This is consistent with the expected behaviour of jet impingement cooling, where higher Reynolds numbers lead to increased convective

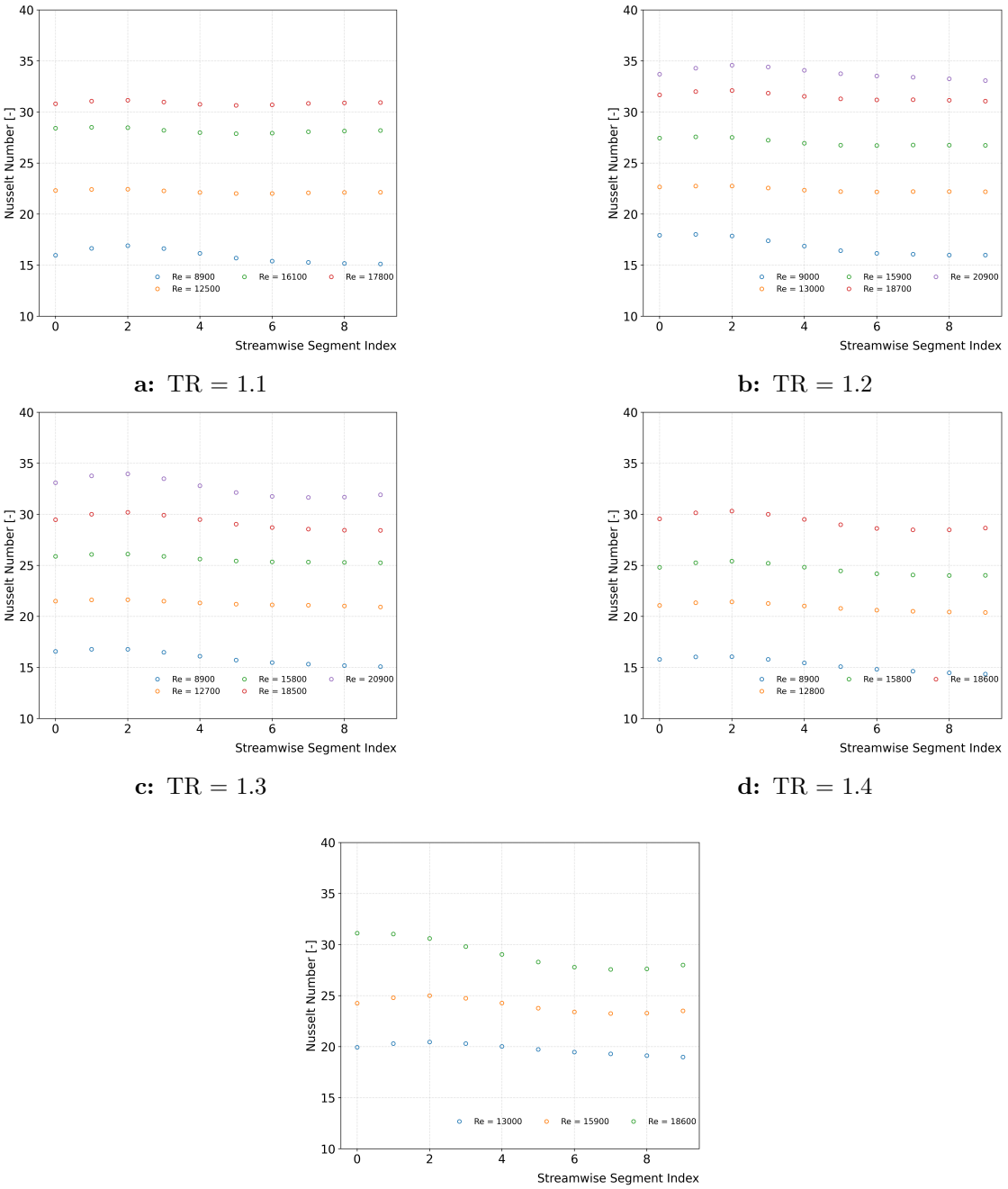

a: TR = 1.1

b: TR = 1.2

c: TR = 1.3

d: TR = 1.4

e: TR = 1.5

Figure 5.2: Experimental results for flat plate jet impingement across five temperature ratios, showing Nu as a function of jet Reynolds number. No Initial Crossflow.

heat transfer due to generally more impingement stagnation and increased coolant mass flow rates. The overall trend of declining Nusselt number with streamwise location (as crossflow is developed) can also be seen on the plots, and is broadly in line with the trends observed in the literature.

However, Figure 5.3 shows that the Nusselt number is consistently lower than the predictions of the Florschuetz correlation, which was developed for idealized conditions. This discrepancy is likely due to several factors, including uncertainty in the thermal boundary conditions: imperfect insulation and non-uniform thermal coupling between the electrical heaters and copper segments. Indeed, the earlier analysis looking at the functional relationship between $Nu \cdot Pr^{1/3}$ also shows that while the power law relationship is broadly in line with the canonical literature, the absolute values of Nusselt number are consistently lower than those predicted by the Florschuetz correlation, for instance.

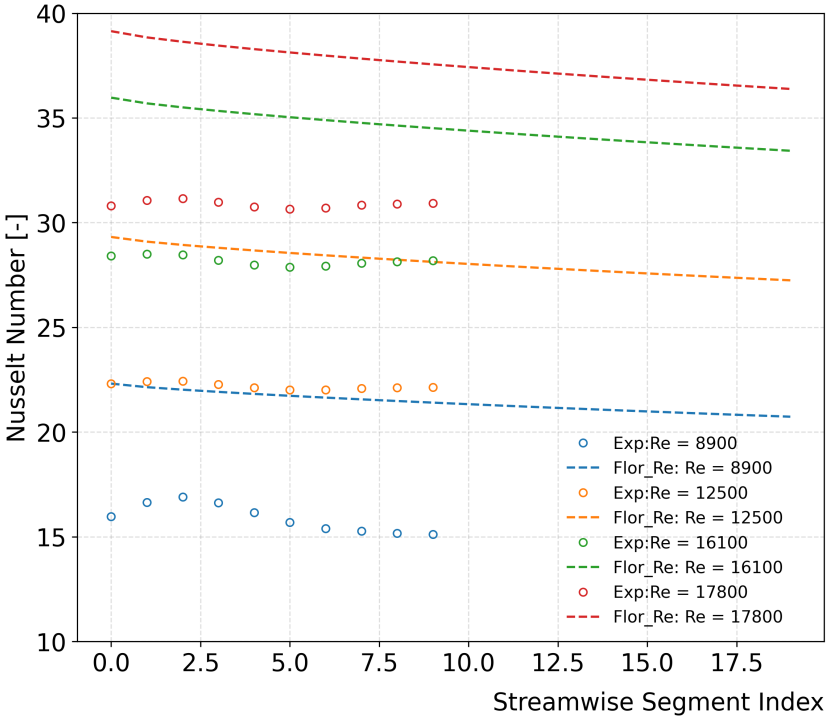

Figure 5.3: Segment-wise comparison of experimental Nusselt number with Florschuetz predictions at matching jet Reynolds number. Although the measured values are consistently lower in magnitude, the trend behaviour is well aligned, indicating that the essential heat transfer mechanisms have been captured.

5.7.2 Corrugated Plate Results

The results of the corrugated plate experiments are presented in Figure 5.4. The data show a consistent trend across all temperature ratios, with the Nusselt number increasing with Reynolds number. No literature exists to predict the Nusselt

number for the custom corrugated plate geometry used in this study, and therefore no comparison is made to canonical literature. The results are presented in a similar format to the flat plate results, with Nusselt number plotted against Reynolds number for each temperature ratio.

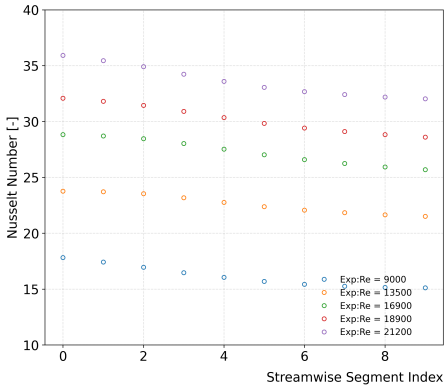

a: TR = 1.1

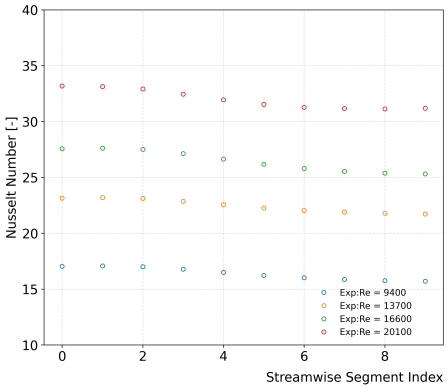

b: TR = 1.2

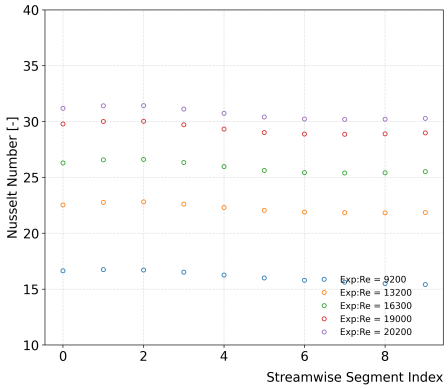

c: TR = 1.3

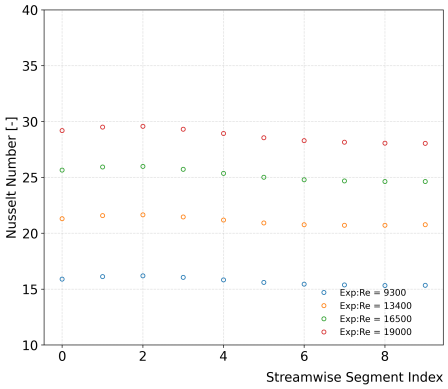

d: TR = 1.4

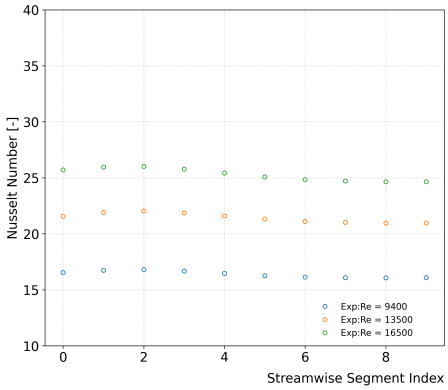

e: TR = 1.5

Figure 5.4: Experimental results for Corrugated plate jet impingement across five temperature ratios, showing Nu as a function of jet Reynolds number. No Initial Crossflow.

5.8 Effects of Temperature Ratio

An open question in this study is how the wall-to-jet temperature ratio, $T_r \equiv T_{\text{wall}}/T_{\text{jet}}$, contributes to degradation of impingement-jet cooling. Building on Hatta et al. [3] and Goodro [38], the present results indicate that the observed sensitivity to T_r is plausibly explained predominantly by volumetric expansion of the coolant, which strengthens the spent-flow crossflow downstream of impingement.

Two related effects act in the same direction: (i) for a hotter wall, greater heat input raises the post-impingement gas temperature and hence the volumetric expansion; and (ii) for a fixed wall temperature, a higher T_r implies a lower jet inlet temperature, so a given thermal increment produces a larger *fractional* density drop (ideal gas: $\rho \propto 1/T$), i.e. $\Delta\rho/\rho \approx -\Delta T/T_0$. By continuity ($\dot{m} = \rho U A$), this enhanced density reduction drives higher channel velocity for fixed mass flow. Since momentum flux scales as ρU^2, velocity has a disproportionately strong influence on crossflow development, meaning that even moderate increases in U amplify the crossflow and increase the likelihood of downstream jet deflection.

Although direct measurements of channel velocity and crossflow strength were not obtained, the available dataset can be post-processed to infer whether these temperature-ratio effects manifest in observable trends of average and streamwise Nusselt numbers, consistent with the momentum-flux argument presented in Chapter 2.

5.8.1 Temperature Ratio Effects: Flat Plate

Figure 5.5 presents the measured variation of hot-section average Nusselt number with wall-to-jet temperature ratio for the flat plate configuration.

The data establish a clear experimental link between temperature ratio and average Nusselt number. Despite the limited range of T_r achievable in this facility, the results extend the findings of Goodro et al. [38], confirming that increasing T_r leads to a monotonic decline in jet cooling effectiveness. The effect is strongest in the highest Reynolds number cases, where the large jet mass flow drives stronger channel mass flow and hence more severe crossflow interaction. These crossflow-dominated regimes appear especially vulnerable to the additional volumetric expansion associated with higher jet temperatures.

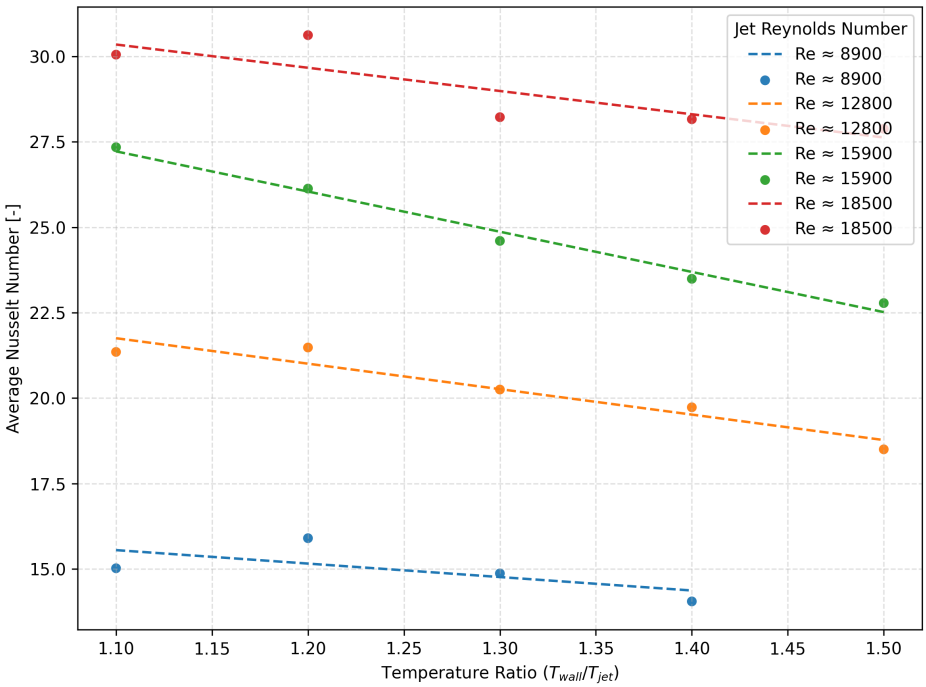

Figure 5.5: Raw data and linear trend lines of average Nusselt number versus jet-to-wall temperature ratio ($T_{\text{wall}}/T_{\text{jet}}$) for the flat plate. Higher Re_{jet} cases show a stronger decline, consistent with increased channel crossflow.

5.8.2 Temperature Ratio Effects: Corrugated Plate

Figure 5.6 presents the corresponding results for the corrugated plate configuration.

In contrast to the flat plate, the corrugated geometry exhibits a weaker sensitivity to T_r, with only modest reductions in Nusselt number observed across Reynolds numbers. This behaviour is evident in the shallower slopes of the Nusselt number trends shown in Figure 5.6, and suggests that the corrugations suppress, at least in part, the amplification of crossflow at elevated temperature ratios.

The most direct (primary) explanation is likely geometric: the corrugated plate increases the effective channel cross-sectional area, which by continuity ($\dot{m} = \rho U A$) reduces the mean channel velocity for a given mass flow and thereby weakens the crossflow. A secondary, more speculative mechanism is that the fountain structures formed by interacting jets are preferentially directed into the corrugation grooves, providing dedicated egress paths for spent flow and reducing interference with subsequent impingement zones. In a periodic jet array, such alignment would occur naturally, further enhancing the mitigating effect.

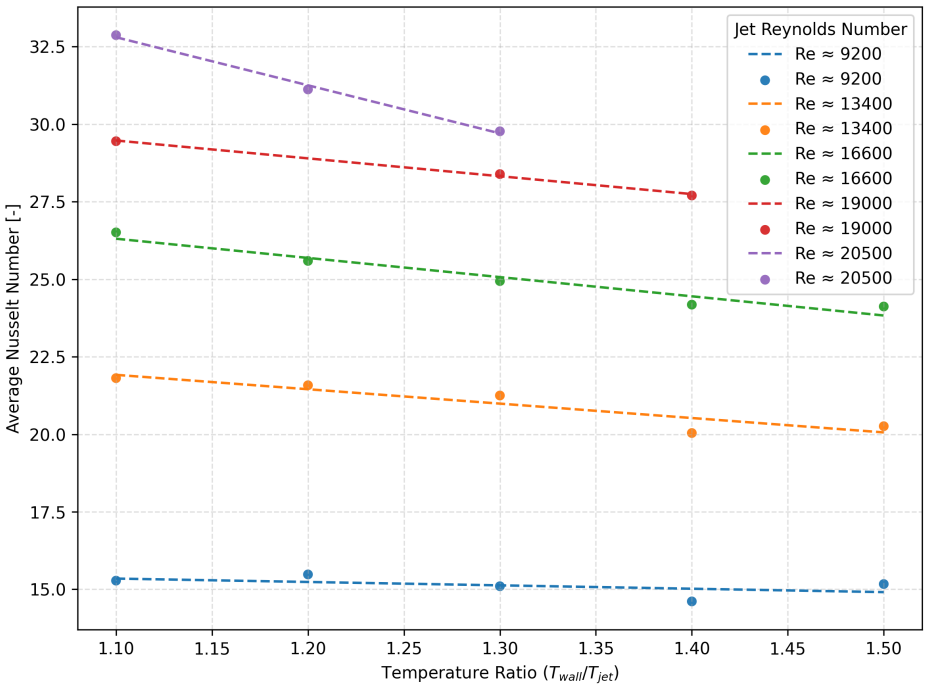

Figure 5.6: Raw data and linear trend lines of average Nusselt number versus jet-to-wall temperature ratio ($T_{\text{wall}}/T_{\text{jet}}$) for the corrugated plate. The decline with increasing T_r is weaker than for the flat plate, consistent with partial crossflow mitigation by the surface geometry.

Florschuetz [26] offered a similar interpretation when comparing staggered and inline jet arrays: uniform arrays allowed fountain interactions to form coherent, self-organising structures, whereas staggered layouts disrupted this mechanism. By analogy, a corrugated plate provides a natural and periodic egress path for fountain flow in a uniform array, reinforcing rather than disrupting its organisation.

5.9 Impingement Jet CFD

Although some early CFD work was undertaken during the initial stages of the project, the decision was made not to pursue a full CFD campaign within the scope of this thesis. This decision was influenced by two main factors; First, a parallel effort within the research group was already underway, with one of the PhD students conducting detailed CFD analysis of the flow structures associated with jet impingement. Second, as the 2D conduction insert concept emerged and matured, it became clear that the most meaningful contribution of this thesis would lie in

demonstrating the feasibility of that concept, rather than duplicating ongoing CFD work. A brief discussion of the CFD work which was done is given in A.

5.10 Discussion and Summary

The experimental rig developed and commissioned during this project has been shown to be capable of producing reliable and physically meaningful results. Despite operating under practical constraints, and without the benefit of metrological precision in every subsystem, the rig captured the key trends in impingement heat transfer with consistency and fidelity.

While absolute Nusselt numbers were lower than those predicted by classical correlations, most notably in the Florschuetz model, this discrepancy is well understood. It reflects realistic limitations in insulation, surface uniformity, and uncontrolled heat losses rather than a failure of the underlying physics. Crucially, the observed functional dependencies on jet Reynolds number and temperature ratio align with the canonical literature and theoretical expectations. This confirms that the rig is appropriate for use in extended impingement geometries and provides a solid foundation for future refinement.

Although the scope of this project did not include detailed fluid dynamic analysis, a complementary CFD campaign conducted within the research group has yielded additional insight into the complex interactions between jet structure, crossflow development, and surface geometry. Those results, while not presented here, provide a compelling direction for future work and further support the findings of this experimental study.

Most importantly, the results presented in this chapter demonstrate that corrugated plate geometries offer a promising avenue for mitigating the effects of crossflow in impingement-cooled passages. While the data are not sufficient to fully characterize the mechanisms involved, the data strongly suggest that jet plate shaping can be used to modify flow behaviour and sustain cooling effectiveness at higher channel crossflow levels. This concept, while conceptually simple, appears to be highly effective. If this geometry can be manufactured reliably in gas turbine blades, it would appear that it has the potential to be impactful. Future study is certainly warranted.

6

High Conductivity Insert Concept

The numerical study presented in this chapter was designed to investigate the feasibility of a two-dimensional, conduction-based cooling concept using finite element thermal analysis. Rather than attempting to replicate full fluid-thermal interactions, the objective was to isolate and evaluate the potential of high-conductivity inserts to laterally redistribute heat within a simplified plate geometry. This modelling approach prioritises physical insight over geometric fidelity, allowing for clear interpretation of conduction-driven effects in a regime that is representative of internal gas turbine cooling. Although more advanced conjugate heat transfer models could provide additional detail, the FEA-based methodology adopted here offers a conservative and credible proof of concept that complements the experimental work.

6.1 Numerical Demonstration of 2D Insert Cooling Concept

Building on the experimental results and the limitations observed in conventional impingement cooling configurations, this chapter presents a numerical investigation of a novel two-dimensional insert concept designed to mitigate crossflow-induced degradation in blade wall cooling performance. The underlying hypothesis is that significant thermal non-uniformity within a channel wall can be passively managed by embedding a thermally conductive insert that redistributes heat through in-plane conduction. Such an insert would act to smooth local temperature gradients and compensate for the reduced performance of downstream jets in high-crossflow environments. This approach has the potential to preserve the effectiveness of impingement-based cooling while offering a simpler manufacturing route than complex corrugated channels.

As discussed in the literature review, advances in additive manufacturing enable spatial control of thermal conductivity and material anisotropy, demonstrating the feasibility of implementing this concept in future gas turbine blade designs. Although the current experimental campaign did not directly investigate crossflow effects, extensive prior work has established its detrimental impact on impingement cooling, particularly in downstream regions. That foundation justifies the relevance of this investigation even in the absence of direct experimental validation.

The numerical model developed in this chapter evaluates whether the introduction of a two-dimensional conductive insert, representing an engineered thermal pathway, can serve as a supplemental or alternative mechanism to reduce hot-spot severity. The model is intentionally simplified to demonstrate physical feasibility and trends, rather than to provide a high-fidelity predictive design tool. The results serve as a compelling proof of concept and establish a foundation for future more detailed analyses.

6.2 Objectives of the Numerical Study

The numerical study aims to provide a simplified yet physically representative demonstration of the proposed two-dimensional conductive insert concept. To maintain simplicity, the model is restricted to steady-state conduction under idealised boundary conditions. A full conjugate heat transfer (CHT) or transient treatment is beyond the intended scope at this stage. The following criteria define the minimum requirements for demonstrating proof of concept:

1. **Representative Physical Behaviour:** The model must capture the essential physics of in-plane conduction within a plate-like geometry subjected to spatially non-uniform surface heat flux and convective cooling on one surface.

2. **Demonstrable Heat Redistribution:** The simulation must show clear evidence of lateral heat transfer from locally heated regions (hot spots) into adjacent areas of lower thermal load, enhanced by the insert. This effect should manifest as a spatial smoothing of internal temperature gradients.

3. **Geometric or Material Sensitivity:** The results must demonstrate that increasing the in-plane thermal conductivity leads to a measurable reduction in maximum surface temperature and/or improved temperature uniformity.

6.3 Proposed Methodology

All simulations in this study were conducted using SolidWorks Simulation, rather than a higher-fidelity computational fluid dynamics or multiphysics platform such as ANSYS. This decision was based on the defined objectives of the numerical campaign, which emphasised feasibility demonstration over detailed resolution of flow physics or fluid-thermal coupling. The goal was not to resolve details of the complex jet or turbulent channel flow, or develop a predictive conjugate heat transfer model. Rather, the purpose is to assess, in simplified terms, the thermal behaviour of the proposed two-dimensional conductive insert concept.

SolidWorks Simulation was selected for its rapid model setup, accessible boundary condition definition, and sufficient capability in solving steady-state conduction problems with representative thermal inputs. As the dominant physical mechanisms in this phase of the work are governed by two-dimensional heat conduction within a simplified plate geometry, the use of a more sophisticated solver was not warranted. Key simplifications, such as the use of prescribed convective boundary conditions and the omission of fluid-solid coupling, enabled a fast, parametric modelling workflow appropriate to the aims of this study.

The modelling approach adopted here is intended to provide a conceptual foundation for subsequent work, where more complex geometries, boundary interactions, and material anisotropy may be incorporated into higher-fidelity models.

6.4 Modelling Challenges with the Embedded Insert Concept

During development of the numerical model, several limitations of the SolidWorks Simulation environment were encountered that required simplifications. The primary objective was to evaluate a fully embedded conductive insert within the target plate,

thereby simulating internal thermal redistribution pathways. This was ultimately achieved by splitting the geometry into separate solid bodies and enforcing bonded thermal contacts, which provided a robust representation of an embedded insert.

However, defining realistic convective boundary conditions proved challenging. The use of split-line features to impose multiple local heat transfer coefficients sometimes interfered with the thermal bond between the parent plate and the insert, particularly when several zones were specified. To maintain stable and repeatable solutions, the convective environment was simplified to three distinct regions: a high-intensity, spatially confined jet-like zone, a secondary region representing wall flow, and a third zone representing fully developed channel flow. Although this does not reproduce the full complexity of a multi-jet impingement array, it is sufficient to capture the governing physics of in-plane conduction and heat redistribution.

A further observation was that in a datum homogeneous-material case, where the insert was specified to have the same conductivity as the parent plate, the temperature field exhibited a small but measurable deviation (on the order of $1-2\,^{\circ}\mathrm{C}$) from the baseline. This effect is attributed to solver artefacts arising from the treatment of bonded interfaces between separate solid bodies. Because the deviation is minor and does not affect the comparative trends, it was judged not to compromise the validity of the analysis.

Overall, these simplifications should be viewed as conservative. By restricting the convective environment to a small number of zones, the model avoids over-fitting to a specific cooling arrangement and instead highlights the general mechanism by which a high-conductivity insert modifies the temperature field. More detailed resolution of impingement patterns would be a natural extension for future work, ideally using a platform capable of conjugate heat transfer simulation such as ANSYS Fluent. Within the present constraints, however, the SolidWorks model successfully demonstrates both qualitatively and quantitatively the feasibility of the conductive insert concept.

6.5 Geometry and Domain Boundary Conditions

For all runs, the computational domain was sized to correspond to the experimental facility 'hot section', which is (625mm $\times$ 312.5mm) with a thickness of 10mm.

To simulate background heating representative of gas turbine operation, the bottom surface of the plate was prescribed a convection boundary condition with $h = 2000, \mathrm{W/m^2K}$, consistent with published estimates for first-row NGVs [51]. The convection reference temperature was set at 1650K, representative of demonstrated commercial engine conditions. For simplicity, all lateral edges of the computational domain were treated as adiabatic boundaries ($q'' = 0$). The bottom (hot side) and lateral edge boundary conditions here described were maintained for every subsequent simulation run.

Top convective cooling zone definitions for each simulation run are given below.

6.6 Reference No-Insert Case

An initial reference configuration was first modelled. The reference case consisted of a flat impingement plate without inserts and subject to a single jet, with secondary wall flow and tertiary channel flow convective regions. This case is not treated as the comparative datum for the study but is retained as an illustrative example for qualitative assessment. These are shown in Figure 6.1.

Heat transfer coefficients of 1000, 500, and 127 $\mathrm{W/m^2K}$ were applied to these zones respectively, based on both experimental facility data and published correlations. This distribution represents a strong central jet followed by wall and channel flow development.

Bottom and edge thermal boundary conditions were held as defined above.

6.6.1 Reference Temperature Distribution

Under the boundary conditions defined above, the reference plate configuration produced the temperature distribution shown in Figure 6.2. At this stage, absolute magnitudes are not physically representative; the purpose is to illustrate the spatial distribution of the thermal field as a preliminary demonstration of the concept.

Figure 6.2 shows a distribution consistent with asymmetric cooling. The maximum temperature occurs at the downstream end of the plate, away from the jet impingement region, as expected. Although simplified, this configuration

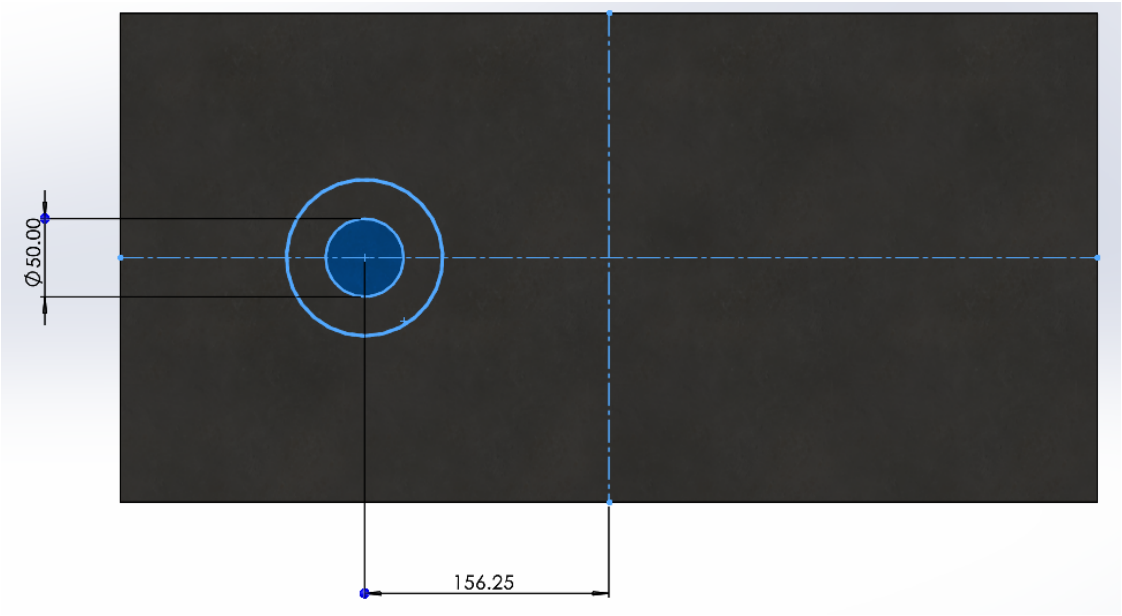

Figure 6.1: Surface boundary condition definition for the reference configuration.

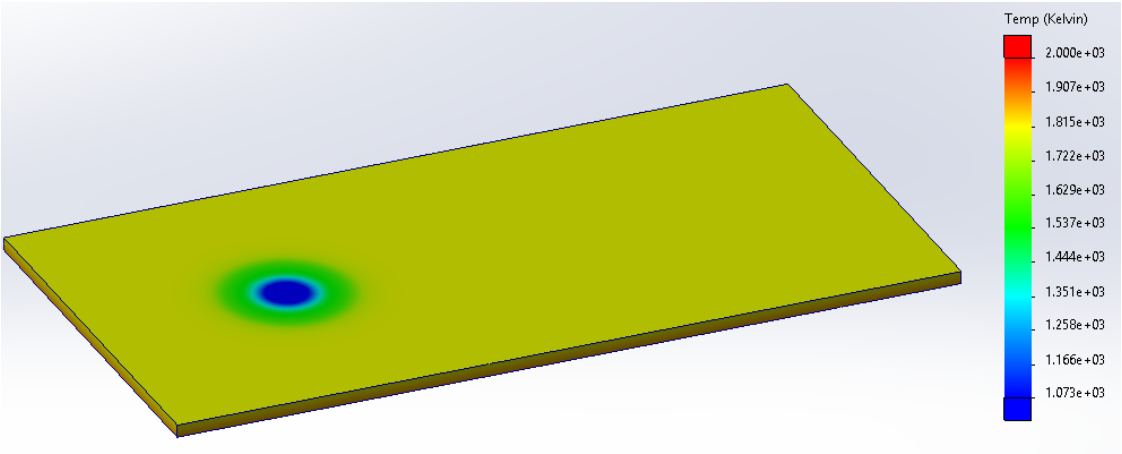

Figure 6.2: Temperature distribution in the reference case with uniform plate material and no insert. Field shown for qualitative clarity only and not representative of experimental conditions.

captures the type of temperature gradients anticipated in a non-uniform cooling environment and serves as a reference for comparison with the insert concept.

6.7 Initial 2D Insert Concept

Building on the reference distribution, a two-dimensional insert was introduced to investigate whether enhanced spanwise conduction could redistribute heat away

from low-convection regions. The insert, shown in Figure 6.3, was inserted into the base plate as a separate solid body in SolidWorks, enabling explicit definition of thermal bonding and independent material assignment.

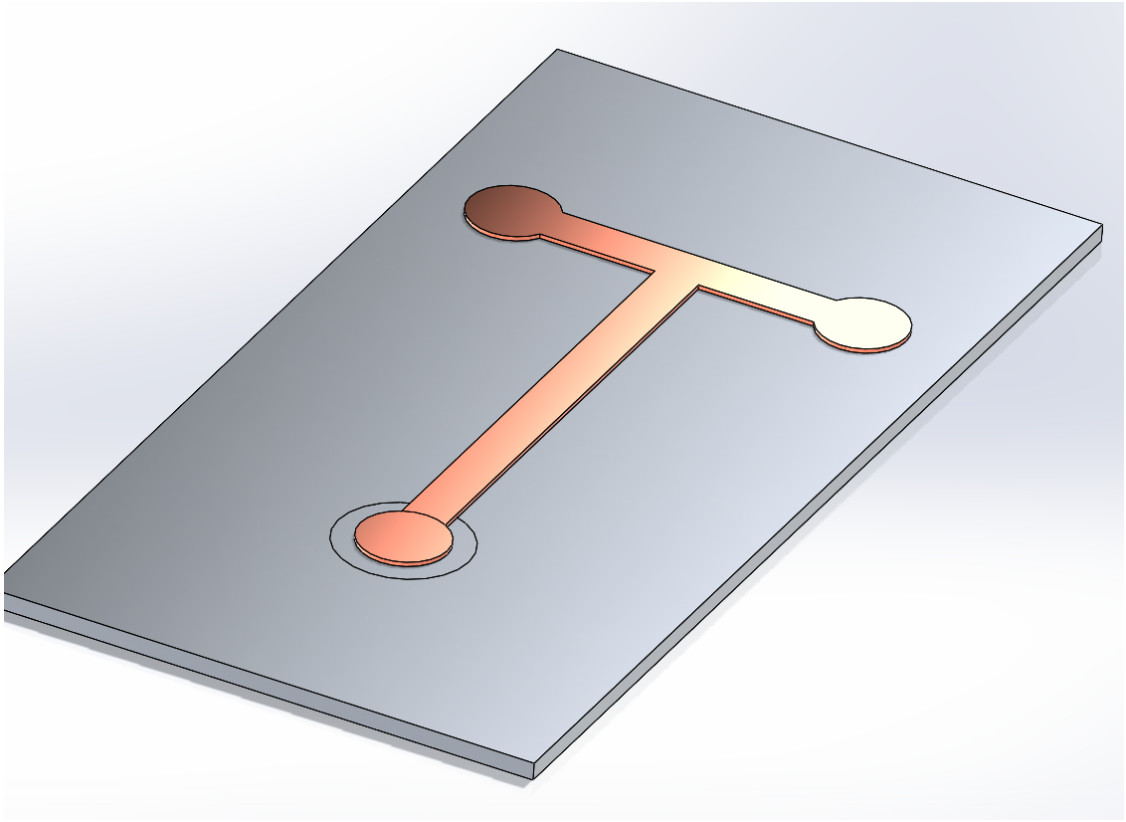

Figure 6.3: Initial 2D insert concept geometry.

This first geometry concept is a 5 mm thick insert embedded within, and thermally bonded to, the base plate.

6.7.1 Insert Simulation Thermal Boundary Conditions

Figures 6.4a and 6.4b show the two different convective zones that were used in the insert feasibility model. Convective zone 1 simulates a single highly-optimised impingement jet with high heat transfer coefficient of 5,000 W/m^{2}K. Zone 2 was set to a lower value of 2,500 W/m^{2}K. These values are arbitrary and used only to illustrate the concept, but are derived as order-of-magnitude for accepted jet-on-metal impingement jet cooling magnitudes. It can be imagined that in a situation where a single highly-optimised jet is used on a conductive insert, then

the remaining convection in the channel would be from channel flow only, so the situation presented here is at least conceptually valid.

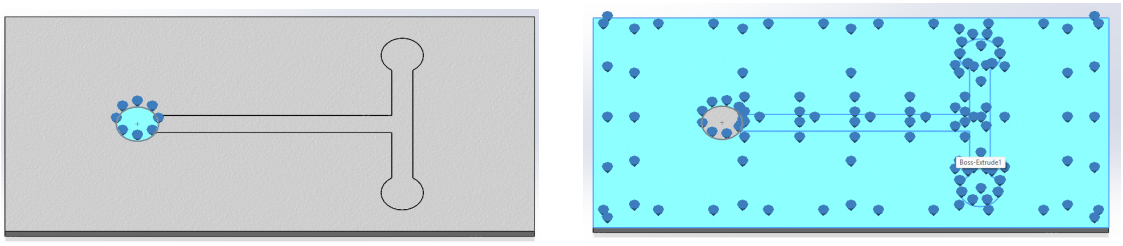

(a) Convection Boundary Condition – Zone 1 **(b)** Convection Boundary Condition – Zone 2

Figure 6.4: Spatial distribution of applied convection boundary conditions for Insert Model Simulation

6.8 Preliminary Qualitative Results

To clearly illustrate the effect of the insert, the first simulation employed an exaggerated material contrast: the substrate was defined as rubber and the insert as copper. The model was refined to ensure good mesh interfaces between the solid bodies, and the solution converged to steady state. The resulting temperature field, shown in Figure 6.5, demonstrates a clear modification relative to the reference case, particularly in the downstream low-convection region. The two-dimensional conductive insert significantly altered the local gradients, providing immediate qualitative validation of the concept.

Although not representative of gas turbine materials, the low conductivity of rubber amplified the effect of the copper insert, producing a distinct disruption of the surface temperature distribution and making lateral heat redistribution unambiguous in qualitative assessment. This configuration also served as a validation exercise, confirming that thermal coupling between the insert and substrate was correctly modelled by SolidWorks. While internal heat flux plots were generated, they are not shown here due to their complexity; nevertheless, they confirmed lateral heat transfer from the rubber substrate into the copper insert, verifying the intended conductive interaction.

At this stage, the fundamental principle underlying the two-dimensional conduction concept has been demonstrated. The following section shifts focus from proof

of principle to quantitative characterisation of the concept using more realistic material selections.

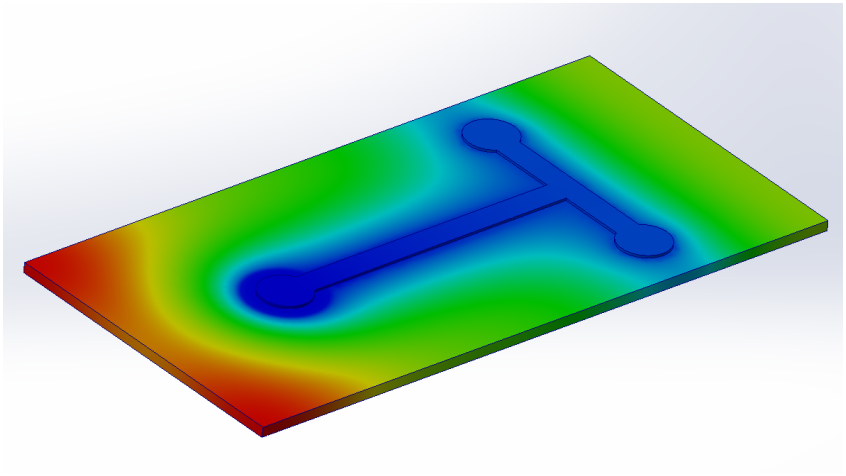

Figure 6.5: Temperature distribution in the 2D insert case, showing the effect of the conductive insert on the temperature field.

6.9 Material Selection for Insert Study

A wide range of runs were conducted on the 2D geometry, exploring different materials, mesh refinements, and convective loading conditions. These exploratory cases were useful for building confidence in the model, but the results presented here focus on configurations that demonstrated both good numerical fidelity and direct relevance to turbine cooling applications. Thus, the cases reported in this thesis model the base plate as Inconel 718, a representative nickel-based superalloy, and the insert as tungsten. Although the manufacturability of tungsten inserts by additive processes is uncertain, it was selected as a high-temperature material with exceptionally high thermal conductivity. Because the insert requires little mechanical strength or creep resistance in the proposed configuration, this choice provides a conservative upper bound on conductive performance. For simplicity and efficiency, only pre-defined materials available within the SolidWorks package were used. The material properties used in the simulations are summarised in Table 6.1.

Material	**Therm. Cond.** [W/mK]	**Density** [kg/m^3]	**Specific Heat** [J/kgK]
Inconel	11.4	8,190	435
Tungsten	200	19,000	130

Table 6.1: Material properties used in the numerical simulations for the plate and insert.

6.10 Results of Numerical Simulations

Having validated the 2D insert concept qualitatively, the remaining part of this chapter will seek to quantify any performance differences in cooling when conductive inserts are used. The preceding section demonstrated that the introduction of a thermally conductive insert can substantially alter the temperature distribution within a plate subjected to non-uniform convective loading. While exaggerated cases with a low-conductivity substrate were primarily illustrative, they confirmed the feasibility and physical intuition of conduction-based thermal redistribution.

The next step is to move from conceptual validation toward engineering relevance. Here, the aim is not to establish whether the insert works, but to assess how effectively the concept performs under conditions representative of gas turbine hardware. To this end, additional simulations were conducted using conventional engineering materials, and performance was evaluated using figures of merit defined earlier in the thesis, including peak surface temperature, spatial uniformity, and standard deviation.

This analysis is not intended to be exhaustive. Rather, it provides a first-order quantification of insert performance and a conservative, yet credible, indication of the concept's potential to mitigate surface thermal gradients.

The results presented here focus on two representative configurations. In the first case, both the base plate and the insert were modelled as Inconel 718. In principle, the use of identical materials should yield little to no alteration of the equilibrium temperature distribution. However, the presence of the insert produced a small modification in the bottom-surface temperature field, as shown in Figure 6.6. This small discrepancy is most plausibly attributable to limitations in the SolidWorks Simulation environment, specifically in how thermal energy transfer is resolved across grid interfaces between separate solid bodies. Physically, such a result is not unreasonable, as any practical implementation of a discrete insert within a plate, even of the same material would introduce some degree of thermal contact resistance,

particularly when laser-sintering additive manufacturing is used. In the present case, the observed variation was only on the order of a few degrees, and can therefore be considered negligible for the purposes of this first validation of the insert concept.

The second configuration employed a tungsten insert within an Inconel base plate, which is a pairing consistent with the high-temperature materials used in modern gas turbine blades. The results, shown in Figure 6.7, demonstrate a subtle modification of the temperature field on the 'hot side'. Though difficult to see on a plot with consistent temperature scales, quantitative analysis showed that variation between the hottest and coldest regions on the bottom surface reached approximately 100 K, with a substantial fraction of the plate drawn down to lower temperatures. This behaviour is fully consistent with the expected role of a high-conductivity insert in redistributing heat away from locally overloaded regions.

While this qualitative comparison provides strong evidence of the concept's merit, the following sections present a quantitative analysis to confirm and characterise the benefit more rigorously.

Note that the temperature scales of both Figures 6.6 and 6.7 have been adjusted to show the subtle changes to the temperature field more clearly in the thesis.

Figure 6.6: Temperature distribution in the insert configuration with Inconel 718 material assigned to both solid bodies.

6.10.1 Figures of Merit for Simulations

The following quantitative metrics were calculated from the numerical simulations to assess the performance of the conduction-enhanced concept:

Figure 6.7: Temperature distribution in the insert configuration with Tungsten insert and Inconel 718 base plate.

- **Average Surface Temperature:** The mean temperature across the entire surface, providing a measure of overall cooling effectiveness.

- **Maximum Surface Temperature:** The highest temperature recorded on the surface of the plate, which serves as a critical design point for cooling systems.

- **Standard Deviation of Surface Temperature:** A statistical measure of temperature variation, indicating how uniformly heat is distributed across the surface.

- **Hot Fraction** Percentage of surface points above the average surface temperature, indicating whether the entire surface was cooled more effectively.

ID	$\overline{T}$ [K]	T_{min} [K]	T_{max} [K]	σ_T [K]	$\phi_{T>\overline{T}}$
Datum No Insert	1874	1600	1880	28.04	0.91
Inconel-Inconel	1682	1680	1710	17.99	0.12
Inconel-Tungsten	1673	1580	1680	5.13	0.18

Table 6.2: Comparison of surface temperature metrics across three insert configurations. $\overline{T}$ is the mean surface temperature, T_{max} is the maximum temperature, σ_T is the standard deviation, and $\phi_{T>\overline{T}}$ denotes the fraction of the surface exceeding the mean temperature.

6.11 Conclusion of Numerical Study

The numerical results presented in this chapter clearly demonstrate the viability of the in-plane conduction concept as a passive thermal management strategy. Across all insert configurations tested, a consistent reduction in mean surface temperature on the bottom (hot side) of the experimental domain was observed relative to the reference case, confirming that high-conductivity pathways embedded within the plate can effectively redistribute heat away from localised hotspots. This behaviour is not solely quantitative: closer inspection of the surface temperature fields reveals that thermal relief extends into regions spatially distant from the primary convective zones.

This spatial redistribution indicates that conduction-based inserts may offer a viable mechanism for cooling off-nominal or downstream areas where convective effectiveness is inherently limited. While detailed optimisation of insert geometry and material selection remains a subject for future work, the core principle underpinning this approach is validated: embedded high-conductivity inserts offer a controllable means of reshaping the surface thermal field. These findings establish a sound basis for continued development and suggest that passive conductive enhancement represents a promising and complementary alternative to traditional convective cooling strategies.

6.12 Future Work

Several opportunities exist to expand upon the findings presented in this study and further develop the in-plane conduction concept. First, improvements to the numerical framework to refine the mesh further and explicitly control the thermal interface for the homogeneous material configuration. Additionally, refinement of the boundary condition implementation to support spatially varying convective heat transfer coefficients would enable more accurate emulation of realistic impingement jet arrays and associated surface HTC distributions.

A natural extension of this work involves transitioning to high-fidelity conjugate heat transfer (CHT) modelling, enabling the full resolution of thermally developed boundary layers and surface HTC variations arising from fluid flow. This will allow

for more representative validation of the concept under engine-realistic conditions. Optimisation studies, including topology-based, parametric and even artificial intelligence approaches should be undertaken to identify insert geometries that are optimal for actual 3D blade wall geometries. Such studies would also benefit from a systematic exploration of material property combinations, including thermal conductivity ratios and interface resistance, to identify the most effective pairings for different thermal loading scenarios.

Finally, the potential of anisotropic thermal conductivity enabled by additive manufacturing should be explored. This is a key enabling technology for the in-plane conduction concept, but may be substantive enough to merit its own study. The ability to tailor thermal properties in specific directions could lead to even greater performance improvements and open up new design possibilities for advanced cooling systems.

7

Conclusions

A flexible, high-performance experimental facility was created to investigate impingement jet cooling under conditions approaching those found in modern gas turbine applications. The modular rig was designed to accommodate a wide range of impingement plate geometries and achieved a maximum temperature ratio of approximately 1.76. This value lies near the upper end of what is reported in the canonical literature.

More than 100 experiments were conducted across a broad range of jet Reynolds numbers and temperature ratios. The facility demonstrated good agreement with established literature benchmarks, providing strong confidence in its use for evaluating alternative jet plate designs. A single corrugated plate geometry was tested and showed reduced crossflow interference in downstream impingement zones. These results support established physical intuition and confirm that internal geometry remains a powerful lever for thermal optimisation, particularly at high temperature ratios where crossflow is amplified by energy exchange between the fluid and the hot wall.

In parallel, a numerical study investigated a novel hybrid cooling strategy that exploits in-plane conduction. Simulations demonstrated that high-conductivity inserts can redistribute heat from hotter to cooler regions, reducing thermal gradients and alleviating peak surface temperatures. While preliminary, this approach offers a complementary pathway to traditional convective strategies, particularly where jet optimisation is constrained by geometric or manufacturing limitations.

The literature review and theoretical foundations provided a structured basis for the study, revisiting classical models of jet impingement and situating the present work in that context. Although frameworks such as the Blasius boundary layer and Florschuetz correlations were not re-derived, they were critically examined to clarify their assumptions and relevance at elevated temperature ratios. In particular, the role of volumetric expansion in shaping flow and heat transfer behaviour

was identified as a key physical mechanism underlying observed trends. These insights informed both the rig design and the interpretation of results, ensuring that experimental and numerical findings remained grounded in first-principles reasoning.

Taken together, the experimental and numerical investigations presented here contribute new data, validate key trends from the literature, and introduce promising directions for advanced thermal management in gas turbine internal cooling systems. These findings were obtained under experimental conditions that approach engine-realistic temperature ratios.

Appendices

A

Preliminary CFD

This appendix presents an early-stage computational fluid dynamics (CFD) study that was undertaken during the initial phase of the project to support the development of the Transfer of Status Report before my change of mode of study to an MSc (Res). While this preliminary study does not constitute a standalone CFD investigation, it successfully established a converging baseline model of the impingement jet array and target channel configuration using the Ansys CFX solver. The primary objectives at this stage were to assess the feasibility of simulating the impinging jet flow field in a simplified domain, validate meshing and solver strategies, and quantify key non-dimensional parameters such as Y^+.

The value of this preliminary work lies in its ability to capture the essential flow physics with sufficient fidelity to resolve jet deflection effects at higher crossflow regimes. This is a non-trivial feature of impingement flows and indicates that the solver, meshing strategy, and turbulence model were suitably implemented. As such, this model represents a technically sound starting point upon which a full CFD campaign incorporating heat transfer and extended domain geometries could have been robustly developed.

Nonetheless, the CFD campaign was not pursued further. This decision reflects a strategic redirection of the research effort rather than any deficiency in the numerical setup. The original CFD effort was scoped to inform preliminary apparatus sizing and TOS development, and did not include heat transfer modelling. As the project evolved, the focus shifted toward evaluating a novel thermal management concept involving in-plane conduction. This concept was more effectively explored using finite element analysis (FEA), which allowed detailed investigation of thermal spreading under realistic boundary conditions derived from experiment.

The CFD results presented here, while limited in scope, provided meaningful insight into the fundamental fluid mechanics of the system and demonstrated numerical stability. They are included in this appendix to document the groundwork

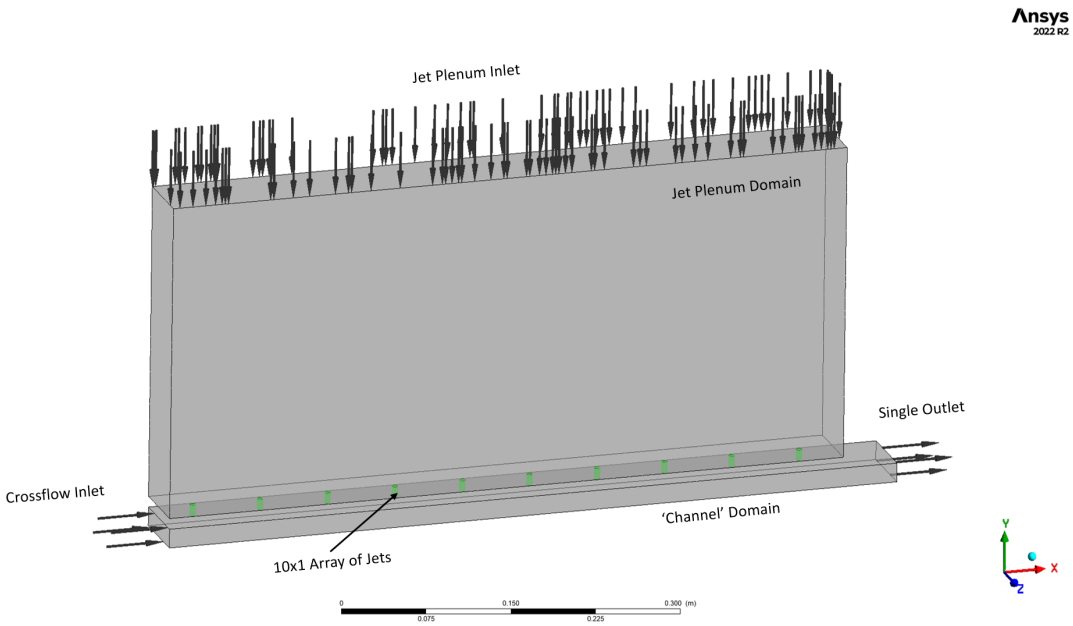

Figure A.1: Truncated 10 x 1 Jet Array Domain With Initial Crossflow.

completed and to provide a reference point for future work that may seek to extend the numerical modelling to include conjugate heat transfer and more complex jet array configurations. A preliminary CFD study for a simplified domain corresponding to a 10x1 jet array has been completed. Runs were performed with and without initial crossflow with datum mass flow rates. Expected macroscopic behaviour is well represented in the preliminary study, and a preliminary mesh independence was demonstrated.

A.1 Preliminary Computational Domain

A truncated 10x1 flow domain is illustrated in Figure A.1. Base geometry requirements were reproduced by creating a parametric SolidWorks fluid domain. The jet holes were created with a small chamfer at inlet and outlet to represent realistic manufacturing, and these features were meshed. All external plenum walls and crossflow channel side walls were defined as no-slip for the preliminary runs. The plenum and crossflow inlets were defined as mass flow inlets with $0.01[kg/sec]$ and $0.003[kg/sec]$. The flow is forced to a single channel outlet as indicated on Figure A.1. The channel outlet is configured as a pressure outlet exhausting to atmospheric pressure.

A.2 Calculation of Wall Y Plus

An initial run was performed without inflation layers to establish the order of magnitude of wall shear stress in the jet holes and at the target face. Data from this initial run was used to calculate inflation sizing for the working mesh.

Using the continuity equation, the expected channel mass flow velocity was calculated using $Q = VA$. For the simplified 1x10 jet array, the channel mass flow corresponds to the jet and initial crossflow values of 1/5th the nominal value for the full 10x5 domain, or 0.013$[kg/sec]$. Full channel velocity at the outlet for the truncated domain is calculated to be 1.84$[m/s]$.

The Reynolds number for the channel exit flow is calculated as 7,884. With the velocity and Reynolds numbers as calculated, the flow is treated as incompressible and turbulent. A wall function must therefore be applied in the solver to correctly simulate the near-wall flow. This requires careful design of the wall adjacent mesh and calculation of the wall centroid to achieve a $Y^+ < 1$ in order to insure that the first near-wall cell is completely contained within the viscous sub layer.

Experimental results show that fully developed turbulent flow in a channel has a complex non-linear velocity profile extending from the near-wall viscous sub layer to the free-stream flow. The full derivation of this can be seen in any text on fluid mechanics, and is not reproduced here. For the purposes of this calculation, the wall *friction velocity* parameter, U_* must be calculated.

$$u_* = \sqrt{\frac{\tau_w}{\rho}} \tag{A.1}$$

The definition of the Y^+ non-dimensional parameter can then be solved determine the correct wall adjacent cell centroid height:

$$Y^+ = \frac{y_{centroid} * u_*}{\nu} \tag{A.2}$$

Wall shear stress and local values of ρ and ν were obtained from the preliminary CFD runs and used to calculate a target first wall-adjacent cell height of $4.93x10^{-05}$ This was used in Ansys Mechanical meshing tool to create suitable inflation layers to capture the near wall flow behaviour for the impingement jet simulation. Ansys CFD Post was used to report highest and average wall Y+ values for the target

Mesh ID	Inflation	First Cell Height	Ave. Target Wall y+
Mesh001	NO	N/A	70
Mesh002	YES	1.53E-05	21
Mesh003	YES	8.0E-06	0.94

Table A.1: Preliminary Mesh Refinement to Achieve Target Y+.

surface and jet walls. Further inflation layer refinement was conducted based on the CFD Post results. Table A.1 shows the progression of the mesh refinement that has so far been performed.

While the model is converging, some key parameters of interest are still changing. A full mesh sensitivity study will be performed for the simulation.

A.3 Meshing

After 3 iterations of mesh refinement, the simulation accurately captures the expected macroscopic features of the flow in the target channel. Impingement jets can be seen deflecting in the downstream direction after interference from the channel crossflow. Figure A.2 illustrates the deflection of the downstream jets as expected.

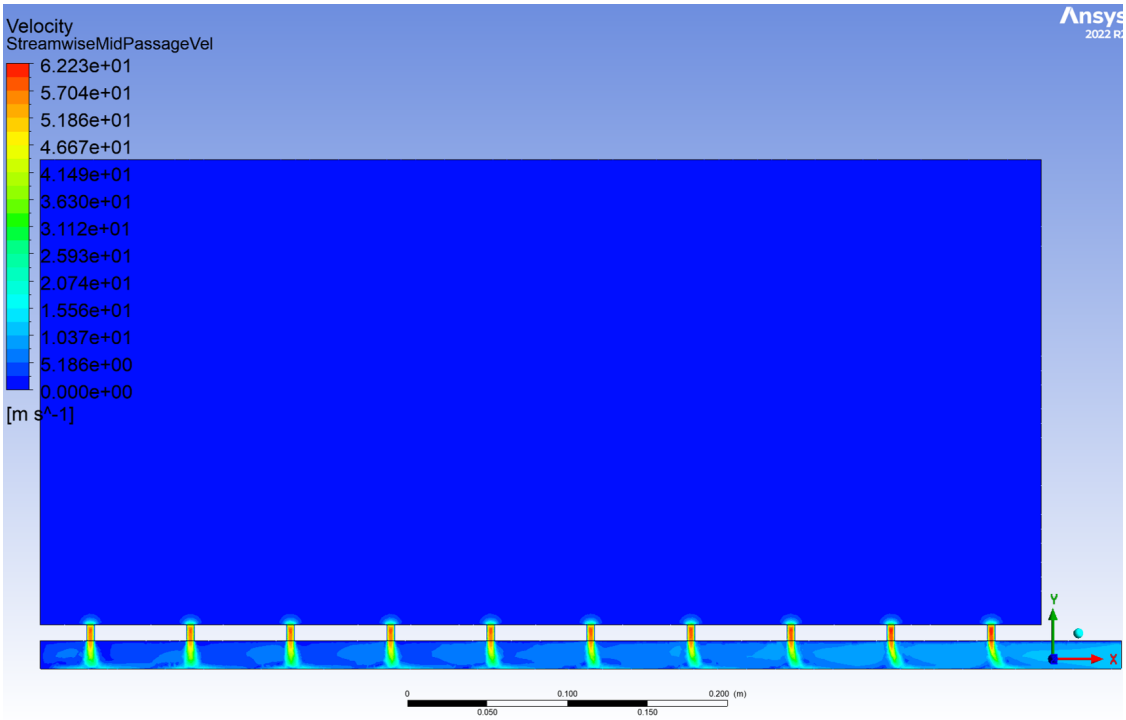

Figure A.2: Downstream Jet Deflection Caused by Channel Crossflow.

A.4 Simulation Setup

Initial calculations from a simple continuity analysis and preliminary CFD show that the flow in the target channel is turbulent. The SST turbulence model was selected in CFX to model the near-wall fluid flow. Appropriate mesh refinement in the wall-adjacent cells has been performed to position the first fluid element well within the viscous boundary layer

A.5 Sanity Checking CFD Results

Comparison of CFD and analytical calculations for jet and channel flow shows good agreement. Calculations for mass flow using the continuity equation for a single row of jets with datum channel width predict an exit velocity of 1.84[m/s]. CFD results show 2.02[m/s]. Jet flow velocities using the Florschuetz[26] predict a jet velocity of approximately 21[m/s]. CFD prediction of jet velocity is 26[m/s].

A.6 Future Work on Numerical Simulation

The focus of this project is experimentation, but CFD is a useful tool to help gain better understanding of the underlying flow physics and can help with sizing components for the experimental apparatus. The preliminary mesh with inflation layers on the target wall gives appropriate wall Y+ values, and the model successfully captures the large scale fluid flow characteristics that would be expected. Predictions of channel and jet velocities are over predicted in the model but this is expected to converge with mesh refinement. The only region where Y+ is significantly above 1 in the wall adjacent cells is in the interior of the impingement holes where the flow is likely separated and dominated by large scale mixing. This is therefore considered insignificant.

The initial mesh is for a single row of jets only, and even with periodic boundaries this configuration represents a 'straight' array. A staggered array of jets will also be meshed for study of that configuration. The fluid domain must be extended to at least 2 spanwise rows of jets with periodic walls to study span-adjacent jet interference effects for both straight and staggered arrays.

Meshing the full 10x5 domain with sufficient inflation will require a mesh with well over 10M elements, and this will be computationally expensive. However, the simulation will be structured to run on the Oxford ARC super computing cluster and the full fluid domain will be simulated.

Since the focus of the proposed research project is to evaluate cooling effectiveness of novel geometries and techniques, heat transfer must be added to the numerical simulation.

The preliminary work is quite promising, however, and a stable baseline datum model has been developed which can be expanded.

References

[1] Leap71. *Multimaterial Metal Printing: The Future of Additive Manufacturing.* Accessed July 21, 2025. Apr. 2023. URL: https://leap71.com/2023/04/20/multimaterial-metal-printing-the-future-of-additive-manufacturing/.

[2] Masayoshi Hatta, Thomas Merritt-Webster, and Budimir Rosic. "THE ROLE OF CORRUGATED IMPINGEMENT COOLING GEOMETRIES AT HIGH TEMPERATURE RATIOS FOR FUTURE GAS TURBINES". In: *Proceedings of Global Power and Propulsion Society.* GPPS Chania24. GPPS-TC-2024-0208, ISSN-Nr: 2504-4400, September 4-6, 2024. Sept. 2024. URL: www.gpps.global.

[3] Masayoshi Hatta, Thomas Merritt-Webster, and Budimir Rosic. "NUMERICAL STUDY ON EFFECTS OF DIFFERENT CORRUGATED HEIGHT AND INITIAL CROSSFLOW ON IMPINGEMENT JET HEAT TRANSFER". In: *Proceedings of ASME Turbo Expo 2024.* Turbomachinery Technical Conference and Exposition GT2024 GT2024-121343. ASME. London, United Kingdom, June 2024.

[4] Shailendra Naik. "Basic Aspects of Gas Turbine Heat Transfer". In: *Heat Exchangers.* Ed. by S M Sohel Murshed and Manuel Matos Lopes. Rijeka: IntechOpen, 2017. Chap. 6. URL: https://doi.org/10.5772/67323.

[5] Yunus A. Çengel and Michael A. Boles. *Thermodynamics: An Engineering Approach.* 8th ed. New York: McGraw-Hill Education, 2015.

[6] Kenichiro Takeishi. "Evolution of Turbine Cooled Vanes and Blades Applied for Large Industrial Gas Turbines and Its Trend toward Carbon Neutrality". In: *Energies* 15.23 2022.

[7] D. R. Clarke, M. Oechsner, and N. P. Padrure. "Thermal-barrier coatings for more efficient gas-turbine engines". In: *Materials Research Society Bulletin* 2012.

[8] *The Gas Turbine Handbook*. US Department of Energy-National Energy Technology Lab (NETL), 2006.

[9] Guohua ZHANG et al. "Optimization of cooling structures in gas turbines: A review". In: *Chinese Journal of Aeronautics* 35.6 2022, pp. 18–46. URL: https://www.sciencedirect.com/science/article/pii/S1000936121003289.

[10] K. Jambunathan et al. "A review of heat transfer data for single circular jet impingement". In: *International Journal of Heat and Fluid Flow* 13.2 1992, pp. 106–115.

[11] R. Viskanta. "Heat Transfer to Impinging Isothermal Gas and Flame Jets". In: *Experimental Thermal and Fluid Science* 6.6 1993, pp. 111–134.

[12] H. Martin. "Heat and Mass Transfer between Impinging Gas Jets and Solid Surfaces". In: *Adcances in Heat Transfer* 1977.

[13] Alexandros Terzis. "Detailed heat transfer distributions of narrow impingement channels for inegrally cast turbine airfols". PhD thesis. Ecole Polytechnique Federale De Lausanne, 2014.

[14] M. Modak, S. Chougule, and S. Sahu. "An Experimental Investigation on Heat Transfer Characteristics of Hot Surface by Using CuO-Water Nanofluids in Circular Jet Impingement Cooling". In: *Journal of Heat Transfer* 140 2018, pp. 1–10.

[15] M. Attalla and M. Salem. "Effect of nozzle geometry on heat transfer characteristics from a single circular air jet". In: *Applied Thermal Engineering* 2013.

[16] Dushyant Singh, B. Premachandran, and Sangeeta Kohli. "Effect of nozzle shape on jet impingement heat transfer from a circular cylinder". In: *International Journal of Thermal Sciences* 96 2015, pp. 45–69. URL: http://dx.doi.org/10.1016/j.ijthermalsci.2015.04.011.

[17] Dushyanth Singh, B. Premachandran, and Sangeeta Kohli. "Experimental and numerical investigation of jet impingement cooling of a circular cylinder". In: *International Journal of Heat and Mass Transfer* 60.1 2013, pp. 672–688. URL: http://dx.doi.org/10.1016/j.ijheatmasstransfer.2013.01.008.

[18] Pratik S. Bhansali, Kishore Ranganath Ramakrishnan, and Srinath V. Ekkad. "Effect of Pin Fins on Jet Impingement Heat Transfer Over a Rotating Disk". In: *Journal of Heat Transfer* 144.4 2022.

[19] Di Zhang et al. "Flow and heat transfer characteristics of single jet impinging on protrusioned surface". In: *International Journal of Heat and Mass Transfer* 58.1-2 2013, pp. 18–28. URL: http://dx.doi.org/10.1016/j.ijheatmasstransfer.2012.11.019.

[20] Bingxing Wang et al. "Heat transfer characteristics during jet impingement on a high-temperature plate surface". In: *Applied Thermal Engineering* 100 2016, pp. 902–910. URL: http://dx.doi.org/10.1016/j.applthermaleng.2016.02.054.

[21] Yang Xu et al. "An experimental study on the flow and heat transfer of an impinging synthetic jet". In: *International Journal of Heat and Mass Transfer* 144 2019, p. 118626. URL: https://doi.org/10.1016/j.ijheatmasstransfer.2019.118626.

[22] Liping Geng, Chuanbo Zheng, and Jingwei Zhou. "Heat transfer characteristics of impinging jets: The influence of unsteadiness with different waveforms". In: *International Communications in Heat and Mass Transfer* 66 2015, pp. 105–113. URL: http://dx.doi.org/10.1016/j.icheatmasstransfer.2015.05.017.

[23] Robert D. Plant, Jacob Friedman, and M. Ziad Saghir. "A review of jet impingement cooling". In: *International Journal of Thermofluids* 17.February 2023, p. 100312. URL: https://doi.org/10.1016/j.ijft.2023.100312.

[24] L. W. Florschuetz, D. E. Metzger, and R. A. Berry. *NASA 3217: Multiple Jet Impingement Heat Transfer Characteristic – Experimental Investigation of In-Line and Staggered Arrays with Crossflow.* Tech. rep. NASA, 1980.

[25] L. W. Florschuetz, D. E. Metzger, and C. R. Truman. *NASA 3373: Jet Array Impingement With Crossflow-Correlation of Streamwise Resolved Flow and Heat Transfer Distributions.* Tech. rep. 3373. NASA, 1981.

[26] L. W. Florschuetz et al. *NASA 3630: Jet Array Impingement Flow Distributions and Heat Transfer Characteristics - Effects of Initial Crossflow and Nonuniform Array Geometry.* Tech. rep. NASA, 1982.

[27] D. M. Kercher and W. Tabakoff. "Heat Transfer by a Square Array of Round Air Jets Impinging Perpendicular to a Flat Surface Including the Effect of Spent Air". In: *Journal of Engineering for Power* Jan. 1970, pp. 73–82.

[28] D. R. H. Gillespie. "Intricate Internal Cooling Systems for Gas Turbine Blading". PhD thesis. University of Oxford, United Kingdom, 1992.

[29] J. Lee et al. "Crossflows from jet array impingement cooling: Hole spacing, target plate distance, Reynolds number effects". In: *International Journal of Thermal Science* 2014. URL: http://dx.doi.org/10.1016/j.ijthermalsci.2014.09.003.

[30] Jung Yang San and Jenq Jye Chen. "Effects of jet-to-jet spacing and jet height on heat transfer characteristics of an impinging jet array". In: *International Journal of Heat and Mass Transfer* 71 2014, pp. 8–17. URL: http://dx.doi.org/10.1016/j.ijheatmasstransfer.2013.11.079.

[31] E. I. Esposito et al. "Novel jet impingement cooling geometry for combustor liner backside cooling". In: *Journal of Thermal Science and Engineering Applications* 1.2 2009, pp. 1–8.

[32] Yongbin Ji et al. "Effect of crossflow regulation by varying jet diameters in streamwise direction on jet impingement heat transfer under maximum crossflow condition". In: *Numerical Heat Transfer, Part A: Applications* 72.8 2017, pp. 579–599. URL: https://doi.org/10.1080/10407782.2017.1394136.

[33] *Effects of a Vortex Generator Pair on Jet Impingement Heat Transfer in Cross-Flow.* Vol. Volume 5B: Heat Transfer. Turbo Expo: Power for Land, Sea, and Air. V05BT13A003. June 2015. eprint: https://asmedigitalcollection.asme.org/GT/proceedings-pdf/GT2015/56727/V05BT13A003/4238607/v05bt13a003-gt2015-42236.pdf. URL: https://doi.org/10.1115/GT2015-42236.

[34] L. G. Hansen and B. W. Webb. "Air jet impingement heat transfer from modified surfaces". In: *International Journal of Heat and Mass Transfer* 36.4 1993, pp. 989–997.

[35] L. A. Gabour and V Lienhard J. H. "Wall Roughness Effects on Stagnation-Point Heat Transfer Beneath an Impinging Liquid Jet". In: *Journal of Heat Transfer* 116.1 Feb. 1994, pp. 81–87. eprint: https://asmedigitalcollection.asme.org/heattransfer/article-pdf/116/1/81/5789034/81_1.pdf. URL: https://doi.org/10.1115/1.2910887.

[36] M. E. Taslim, Y. Pan, and K. Bakhtari. "Experimental racetrack shaped jet impingement on a roughened leading-edge wall with film holes". In: *American Society of Mechanical Engineers, International Gas Turbine Institute, Turbo Expo (Publication) IGTI*. Vol. 3 B. 2002, pp. 897–906.

[37] N. M. R. Jeffers et al. "Heat transfer from novel target surface structures to a normally impinging, submerged and confined water jet". In: *Journal of Thermal Science and Engineering Applications* 1.3 2009, pp. 1–9.

[38] Matt Goodro et al. "Effect of temperature ratio on jet array impingement heat transfer". In: *Journal of Heat Transfer* 131.1 2009, pp. 1–10.

[39] J. E Hartsel. "Prediction of Effects of Mass-Transfer Cooling on the Blade-Row Efficiency of Turbine Airfoils". In: *AIAA* 1972.

[40] J. H. Horlock, D. T. Watson, and T. V. Jones. "Limitations on Gas Turbine Performance Imposed by Large Turbine Cooling Flows ". In: *Journal of Engineering for Gas Turbines and Power* 123.3 Feb. 2001, pp. 487–494. eprint: https://asmedigitalcollection.asme.org/gasturbinespower/article-pdf/123/3/487/5602327/487_1.pdf. URL: https://doi.org/10.1115/1.1373398.

[41] A. Elkholy, M. Rouby, and R. Kempers. "Characterization of the anisotropic thermal conductivity of additively manufactured components by fused filament fabrication". In: *Progress in Additive Manufacturing* 4.4 Dec. 2019, pp. 497–515.

[42] Yunchao Jia et al. "High through-plane thermal conductivity of polymer based product with vertical alignment of graphite flakes achieved via 3D printing". In: *Composites Science and Technology* 145 2017, pp. 55–61. URL: https://www.sciencedirect.com/science/article/pii/S0266353816320978.

[43] D. M. Hymas, M. A. Arie, F. Singer, et al. "Enhanced air-side heat transfer in an additively manufactured polymer composite heat exchanger". In: *16th IEEE Intersociety Conference on Thermal and Thermomechanical Phenomena in Electronic Systems (ITherm)*. IEEE, 2017, pp. 634–638.

[44] U. Kalsoom et al. "A 3D printable diamond polymer composite: a novel material for fabrication of low cost thermally conducting devices". In: *RSC Advances* 6.44 2016, pp. 38140–38147. URL: http://dx.doi.org/10.1039/C6RA05261D.

[45] Amit Bandyopadhyay and Bob Heer. "Additive manufacturing of multi-material structures". In: *Materials Science and Engineering: R* 129 2018, pp. 1–16.

[46] Nicholas F. Jones, Jack L. Beuth, and Maarten P. de Boer. "Directed energy deposition joining of Inconel 625 to 304 stainless steel with direct bonding". In: *Journal of Materials Research* 36.18 2021, pp. 3701–3712. URL: https://doi.org/10.1557/s43578-021-00304-4.

[47] Chester V. Wells. *Principles and Measurement Uncertainty Analysis in Research and Applications*. Tech. rep. NREL/TP-XXXX-XXXX. Presented at the Third Annual Infrared Radiometric Sensor Calibration Symposium, Logan, Utah, September 14–17, 1992. Golden, Colorado: National Renewable Energy Laboratory (NREL), Nov. 1992. URL: https://www.nrel.gov.

[48] Engineering Toolbox. *Air - Thermal Conductivity, Heat Capacity and Viscosity*. Accessed: 2025-07-30. 2005. URL: https://www.engineeringtoolbox.com/air-properties-viscosity-conductivity-heat-capacity-d_1509.html.

[49] W. F. McGreehan and M. J. Schotsch. “Flow Characteristics of Long Orifices With Rotation and Corner Radiusing”. In: *Journal of Turbomachinery* 110.2 Apr. 1988, pp. 213–217. eprint: https://asmedigitalcollection.asme.org/turbomachinery/article-pdf/110/2/213/5666911/213_1.pdf. URL: https://doi.org/10.1115/1.3262183.

[50] Isaac Newton. “Scala graduum Caloris. Calorum Descriptiones et Signa”. In: *Philosophical Transactions of the Royal Society of London* 22.270 1701. Published anonymously; attributed to Newton., pp. 824–829.

[51] Vijay K. Garg. *Heat Transfer in Gas Turbines*. Contractor Report NASA/CR–2001-210942. Prepared for Turbulent Heat Transfer III, sponsored by ASME, Girdwood, Alaska, March 18–22, 2001. Prepared under Contract NAS3-00180. Brook Park, Ohio: National Aeronautics and Space Administration, Glenn Research Center, June 2001. URL: https://gltrs.grc.nasa.gov/GLTRS.